DEVELOPMENT OF A STATIONARY CHEST TOMOSYNTHESIS SYSTEM USING CARBON NANOTUBE X-RAY SOURCE ARRAY

Jing Shan

A dissertation submitted to the faculty at the University of North Carolina at Chapel Hill in partial fulfillment of the requirements for the degree of Doctor of Philosophy in the Department of Physics and Astronomy (Physics).

Chapel Hill
2015

Approved by:

Otto Zhou

David Lalush

Yueh Z. Lee

Jianping Lu

Xiaohui Wang

Sean Washburn

ABSTRACT

Jing Shan: Development of a stationary chest tomosynthesis system using carbon nanotube x-ray source array
(Under the direction of Otto Zhou)

X-ray imaging system has shown its usefulness for providing quick and easy access of imaging in both clinic settings and emergency situations. It greatly improves the workflow in hospitals. However, the conventional radiography systems, lacks 3D information in the images. The tissue overlapping issue in the 2D projection image result in low sensitivity and specificity. Both computed tomography and digital tomosynthesis, the two conventional 3D imaging modalities, requires a complex gantry to mechanically translate the x-ray source to various positions.

Over the past decade, our research group has developed a carbon nanotube (CNT) based x-ray source technology. The CNT x-ray sources allows compacting multiple x-ray sources into a single x-ray tube. Each individual x-ray source in the source array can be electronically switched. This technology allows development of stationary tomographic imaging modalities without any complex mechanical gantries. The goal of this work is to develop a stationary digital chest tomosynthesis (s-DCT) system, and implement it for a clinical trial.

The feasibility of s-DCT was investigated. It is found that the CNT source array can provide sufficient x-ray output for chest imaging. Phantom images have shown comparable image qualities as conventional DCT. The s-DBT system was then used to study the effects of source array configurations and tomosynthesis image quality, and the feasibility of a physiological gated s-DCT. Using physical measures for spatial resolution, the 2D source configuration was shown to have improved depth resolution and comparable in-plane resolution. The prospective gated tomosynthesis images have shown substantially reduction of image blur associated with lung motions. The system was also used to investigate the

feasibility of using s-DCT as a diagnosis and monitoring tools for cystic fibrosis patients. A new scatter reduction methods for s-DCT was also studied. Finally, a s-DCT system was constructed by retrofitting the source array to a Carestream digital radiography system. The system passed the electrical and radiation safety tests, and was installed in Marsico Hall. The patient trial started in March of 2015, and the first patient was successfully imaged.

ACKNOWLEDGEMENTS

First and foremost, I am deeply grateful to my advisor, Dr. Otto Zhou for his guidance and encouragement throughout my graduate studies. His enthusiasm and dedication in translating research to useful applications has truly inspired me. I also highly appreciate all the members in my committee, Dr. David Lalush, Dr. Yueh Z. Lee, Dr. Jianping Lu, Dr. Xiaohui Wang, and Dr. Sean Washburn for their their guidance and advice. Particular thanks goes to Dr. Jianping Lu, and Dr. Yueh Z. Lee for helpful insights and guidance into my research. I would also like to thank each member of our research group, past and present, that has helped me through my researches and studies, including: Laurel Burk, Jabari Calliste, Guohua Cao, Pavel Chtcheprov, Emily Gidcumb, Mike Hadsell, Allison Hartman, Christy Inscoe, Marci Potuzko, Xin Qian, Shabana Sultana, Jiong Wang, Gongting Wu, Guang Yang, Jerry Zhang, and Lei Zhang.

I would like to thank our industrial collaborators in Carestream Health Inc., and XinRay Systems Inc. for the help and discussions. These include Michael Heath, David Foos, Weidong Huang, Yuan Cheng, Derrek Spronk, Houman Jafari, and Philip Laganis. I thank the staffs of the UNC Hospital, Department of Environment, Health, and Safety of UNC, and UNC Cardio-thoracic surgery simulation lab for technical support. I also thank Carestream Health Inc., National Cancer Institute grant (R21 CA185741), Lineburger Comprehensive Cancer Center of University of North Carolina at Chapel Hill, and UNC Graduate School Dissertation Completion Fellowship for the fundings and supports for the research projects.

Finally, I would like to thank all my friends and family for their support throughout my graduate school. I would like to thank Margaret Anagnos for the encouragement. Most of all, I am grateful for my parents, Yucai Shan and Kaijing Fu, for their love and unconditional support.

TABLE OF CONTENTS

LIST OF TABLES

LIST OF FIGURES

LIST OF ABBREVIATIONS AND SYMBOLS

AEC	Automatic exposure control
AP	Anterior-posterior
ASF	Artifacts spread function
CF	Cystic Fibrosis
CNT	Carbon nanotube
CT	Computed tomography
CXR	Chest x-ray radiography
DCT	Digital chest tomosynthesis
DTS	Digital tomosynthesis
EHS	Department of Environment, Health and Safety
FDA	Food and Drug Administration
FEA	Finite element analysis
FWHM	Full width at half maximum
HVL	Half value layer
IRB	Institutional review board
MPE	Multi pixel electronics
MRT	Micro-beam radiation therapy
MTF	Modulation transfer function
PA	Posterior-anterior
PSA	Primary Sampling Apparatus
ROI	Region of interest
RTT	Real Time Tomography
s-DBT	stationary digital breast tomosynthesis
s-DCT	stationary digital chest tomosynthesis
SdNR	Signal difference to noise ratio
SEM	Scanning electron microscopy

SI	Superior-inferior
SNR	Signal to noise ratio
SPR	Scatter to primary ratio
UNC	University of North Carolina at Chapel Hill

CHAPTER 1: Introduction

Section 1.1: Dissertation Overview

X-ray imaging is the most widely used, non-invasive medical test that help physicians diagnose medical conditions. It utilizes the difference of absorption or attenuation rates of materials to x-ray photons to produce images. Because of it can show the human anatomy non-invasively, it was used for medical examinations shortly after its discovery. Nowadays, x-ray imaging has evolved into multiple modalities, each focusing on specific tasks. Among all of them, imaging modalities used in diagnosing medical conditions of the chest, which includes imaging lungs, hearts, and bones of spine and chest, will be the focus in this discussion.

Chest x-ray radiography (CXR) is the most widely used chest x-ray imaging technique.[1] It has been ordered so commonly by doctors that it's the most performed diagnostic imaging. The advantages of this modality are high accessibility, low cost, and relatively low radiation exposure to the patient. CXR simply acquires a 2D projection image of the chest. However, the tissues in the path of the x-ray beam superimpose onto each other in the final image. The tissue overlapping lowers the visibility of lesions, resulting low sensitivity and specificity for CXR.

Computed tomography (CT), which was invented in the 1970s, is a 3D imaging modality.[2] During one CT scan, hundreds of projection images are acquired by rotating the x-ray source around the body. 3D volume data is computed from these base images. The dataset is usually sliced along a certain direction and a stack of cross-sectional images is presented to doctors. The computed images remove tissue overlapping, thus increasing the visibility of lesions. However, the patients are exposed to much higher radiation in a CT examination

compared to CXR. Studies have shown the dose from a normal chest CT scan is on the order of 100 times the dose of a CXR. [1, 3] The procedure is also more expensive. [1]

Digital tomosynthesis (DTS) is another 3D imaging modality that produces sectional images using low dose projection images acquired over a limited scanning angle. [1, 4] Compared to CT, DTS reduces both the radiation dose to the patient and the examination cost. [1] The technology is used clinically on breast, chest, sinonasal, abdominal, and musculoskeletal imaging. [1, 5–7] Multiple studies have shown that digital chest tomosynthesis (DCT) improves the ability to detect small lung nodules and other lung pathologies compared to CXR. [8–12] Several commercial DCT systems are used clinically. These DCT systems mechanically sweep a single x-ray source over a long distance to acquire projection images at different viewing angles. The moving x-ray source results in a relatively long scanning time ($\sim 10\ s$), which leads to potential patient motion blur. [13, 14]

In this dissertation, the feasibility and development of a stationary DCT system using the carbon nanotube (CNT) x-ray source technology developed at University of North Carolina at Chapel Hill (UNC) will be investigated. The key technology is the stationary digital chest tomosynthesis (s-DCT) system using a CNT x-ray source, which enables tomographic imaging without any mechanical motion of the x-ray source. [15] The CNT source array may hold the future of an affordable 3D imaging modality in future.

The primary goal of this dissertation is to develop an s-DCT prototype system for use in a clinical trial. A desktop proof-of-concept system was first developed. System was characterized to demonstrate the feasibility of s-DCT system. Then a prototype s-DCT was constructed by retrofitting the CNT source array to a digital radiography system. Once the s-DCT passed the electric and radiation safety certification, it was moved to a clinical research setting for the clinical trial.

The secondary goal of this dissertation is to investigate the system requirement of CNT source arrays for applications of chest tomosynthesis, and parameters affecting image quality. Image configurations for tomosynthesis, such as dose and source array geometry configura-

tion will be studied. The effect of imaging time on tomosynthesis image quality, and the physiologically gated tomosynthesis will be investigated too.

Section 1.2: Specific Research Aims

1.2.1: Feasibility of s-DCT

In this specific aim, a bench-top system was developed to demonstrate the feasibility of s-DCT using a CNT source array. Key questions investigated in this phase included whether the CNT x-ray source array can output sufficient x-ray flux needed for chest imaging; whether the s-DCT system has comparable or better image quality compared to current DCT systems; and the impact of imaging configurations on the tomosynthesis image quality. The source array output and consistency between sources was measured. Anthropomorphic phantom images were acquired for overall evaluation of the system image quality, and the system modulation transfer function (MTF) and artifacts spread function (ASF) was measured to quantitatively characterize the image quality. The effects of the number of beams and tomosynthesis angular coverage on image quality was studied.

1.2.2: Integration of s-DCT for Clinical Use

An s-DCT system was constructed by retrofitting the CNT x-ray source array to the Carestream digital radiography x-ray system. The system was modified to comply with regulations on electric and radiation safety. The system was characterized for clinical use based on new imaging geometry and dose requirement using an anthropomorphic phantom. A customized operating software was developed for radiologist technician use.

1.2.3: Investigation of Imaging Parameters and Imaging Protocols

Imaging parameters that affect the tomosynthesis image quality were studied in this phase, using both the bench-top system and the s-DCT system. Besides the physical phan-

tom and anthropomorphic phantom, porcine lung specimens and human cadaver samples were imaged to investigate the imaging protocols, including imaging dose, imaging configurations and imaging time. Physiologically gated tomosynthesis was also studied in this phase. The effects of respiration gated s-DCT for motion reduction were evaluated and implemented for clinical trial.

Section 1.3: Dissertation Organization

This dissertation is organized in the following order: (1) background information, (2) system development and related research, (3) investigations of imaging parameters and imaging protocols, and (4) clinical trial implementation of the system. Chapter 2 provides background information about x-rays. Chapter 3 gives an overview of tomosynthesis and its application to chest imaging. Chapter 4 covers the background on CNT x-ray sources and related applications. In Chapter 5, the feasibility study of s-DCT is reported. Characterization of the system and related physics problems are discussed in Chapter 6. Chapter 7 investigates the effects of system configurations on image quality. Physiologically gated s-DCT is studied in Chapter 8. Chapter 9 covers other applications and a scatter reduction technique for s-DCT system. Chapter 10 overviews the implementation of the s-DCT for clinical trial. Finally, in Chapter 11, the dissertation is summarized and the future direction of the research is discussed.

CHAPTER 2: X-rays

Section 2.1: Discovery of X-rays

German physicist Wilhelm Conrad Röntgen first discovered x-rays on November 8^{th}, 1895 when he was studying the cathode rays in "Crookes tubes", an evacuated glass bulb with positive and negative electrodes, which display fluorescent glow when high voltage current passing through. Röntgen noticed the green fluorescent light on the screen even though the tube was blocked with heavy black papers. He figured out the fluorescence was caused by invisible rays from the tube, which penetrated the paper and struck the screen. He named the "invisible light" he discovered "x-ray", where the "x" is used to indicate unknowns in mathematics.[16]

After a series of experiments, he found that x-rays were capable of passing through a variety of substances, including soft tissues of the human body such as muscles. Photographic films were used to record shadows of objects imaged by x-ray. One of the earliest photographs of x-ray was the hand of Röntgen's wife (Figure 2.1), which first demonstrated the idea of using x-ray for medical imaging.

Section 2.2: Interactions with Matter

X-ray is a form of electromagnetic radiation of exactly the same nature as light, but of much shorter wavelength. The wavelength of x-rays typically range from 100 nm to 0.01 nm, corresponding to photon energies on the order of 100 eV to 100 keV.

X-ray photons carry energy that is proportional to their frequency according to quantum

Figure 2.1: X-ray photograph of the hand of Röntgen's wife.
[16]

mechanics, as shown in Equation 2.1.

$$E = h\nu = h\frac{c}{\lambda} \tag{2.1}$$

where the h is Planck's constant. The photon interacts with matter while traveling through space, resulting in absorption and scattering of x-rays. The interaction between x-ray photon and matter constitute the physics behind x-ray imaging. There are four main ways x-rays interact with matter: photoelectric absorption, Rayleigh scattering, Compton scattering, and pair production. The strength of these interactions are mainly determined by the x-ray photon energy and the material composition of the matter. For medical imaging, photoelectric absorption, Rayleigh scattering, and Compton scattering are most common interactions.(Figure 2.2)

2.2.1: Photoelectric Absorption

Photoelectric absorption is the dominant interaction for low-energy x-ray. In this process, illustrated in Figure 2.3, energy of an x-ray photon is transferred to an electron of an atom

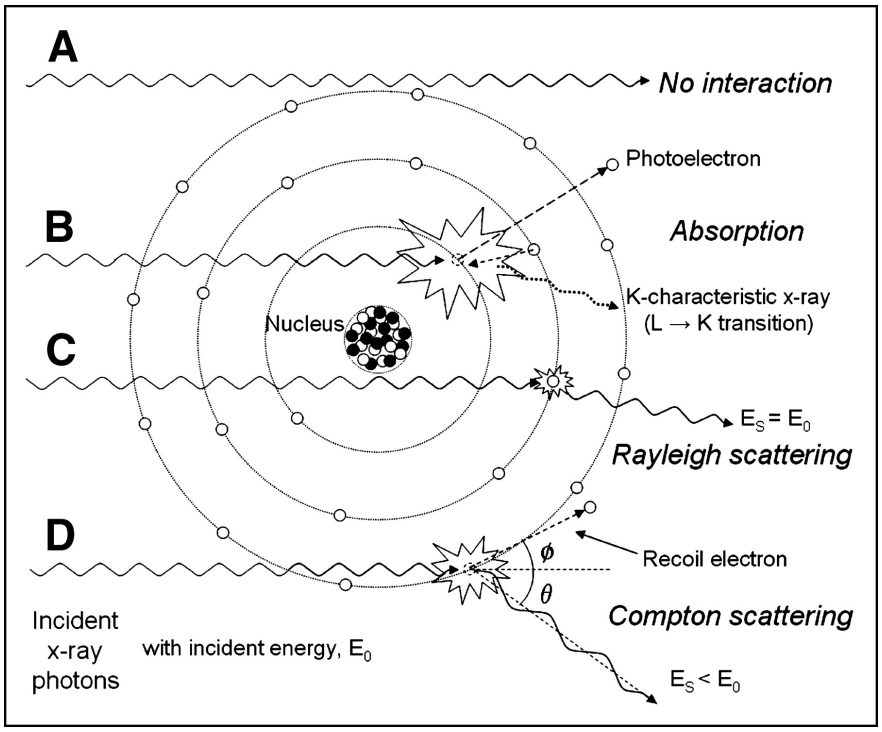

Figure 2.2: Illustration of x-ray and matter interactions. (A) Most x-ray photons have no interaction with the material, passing through unattenuated. (B) Photoelectric absorption results in total removal of the x-ray photon and production of a photoelectron, and a characteristic x-ray. (C) Elastic Rayleigh scattering with small change of trajectory of the x-ray photon. (D) Compton scattering between high energy photons and less bounded electrons. Scattering photon with less energy and a recoiled electron are generated.
[17]

when the photon energy is higher than the electron binding energy in the atom. The electron is freed up from the atom and the excessive energy is transferred to the kinetic energy of the ejected electron, which is called the photoelectron. If the photoelectron is released from the inner orbit of an atom, which is a lower energy and more stable quantum state, other electron in the higher energy state tends to "jump" to this state and fill the vacancy. The energy difference between two states is released in the form of electromagnetic radiation, resulting in characteristic x-rays. However, in some cases, the released characteristic x-ray can excite another electron at a higher energy state to a free electron (the Auger electron).[18] The kinetic energy of the Auger is the difference between characteristic x-ray photon energy and the binding energy of the Auger electron. The resulted vacancy from the release of an Auger

electron or characteristic x-ray leads to another cascaded emission of characteristic x-rays or Auger electrons.

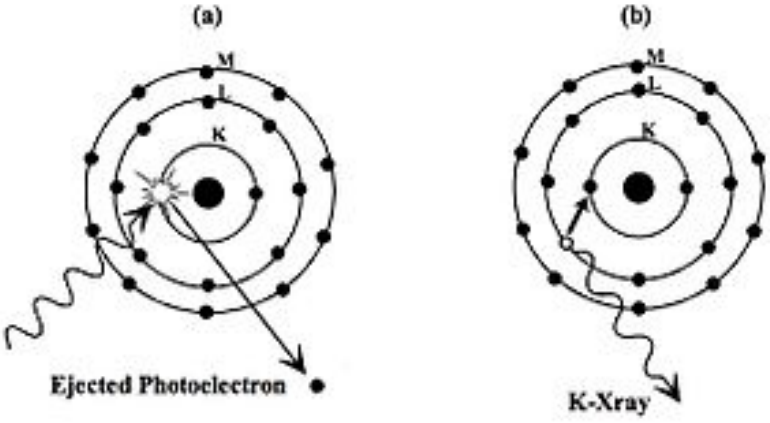

Figure 2.3: Illustration of photoelectric effect. (a) Photon absorption and ejection of photoelectron. (b) Characteristic x-ray emission.
[19]

Photoelectric absorption is subject to statistical processes. The probability of the effect is described by the cross section σ.[17]

$$\sigma_{pe} \propto \frac{Z^n}{E^3} \tag{2.2}$$

where Z is the atomic number of the material, and E is energy of the incident photon. The higher the photon energy, the less likely photoelectric absorption happens. The σ also proportion to Z. The heavier the atom (higher Z), the more photons are absorbed. The variance of absorption rate of different material results in the contrast of the object in the projected x-ray image. However, in this interaction, x-ray energy is transferred to matter, ionizing atoms and disrupting molecular bonds, which is harmful to living tissue.

2.2.2: Rayleigh Scattering

Besides being absorbed by matter, x-ray photons can be also scattered by atoms. Rayleigh scattering is one of the scattering interactions between x-ray photons and matter. It is an elastic scattering, meaning the energy of the scattered photon does not change, as shown in Figure 2.2. This process occurs when the incoming x-ray photon temporarily excites the electron without removing it from the atom, the excited electron returns to its normal energy state by emitting a photon with the same energy, but in a different direction. In this interaction, no energy is deposited into matter, thus it does not contribute to imaging dose. However, the scattered photons cause increased noise in the image which degrade image quality. Rayleigh scattering is more likely to happen with low energy x-ray photons and high Z material. The probability of Rayleigh scattering is described by the scattering cross-section:[17]

$$\sigma_R \propto \frac{Z^2}{E^{1.2}} \tag{2.3}$$

2.2.3: Compton Scattering

Compton scattering is another form of scattering between x-ray and matter. Compton scattering is an inelastic scattering. It is the dominant interaction for high energy x-ray photons. When the energy of the incident photon is much higher than the binding energy of the electron, part of the energy is transferred to the electron, which causes a recoil and removal of the electron. The remainder of the energy is transferred to the scattered photon, which has a trajectory with an angle of θ relative to the trajectory of the incident photon, as illustrated in Figure 2.2. θ is called the scattering angle. Both the total momentum and energy are conserved in this process, therefore, the scattered photon is given by:[17, 20]

$$E_s = \frac{E_i}{1 + \frac{E_i}{m_e c^2}(1 - \cos\theta)} \tag{2.4}$$

Where E_s is the energy of the scattered photon, E_i is the energy of the incident photon, $m_e c^2$ is the rest energy of electron (511 keV), and θ is the scattering angle.

At low energies ($\sim$ $5keV$), x-ray photons are mostly back-scattered; at intermediate energy ($\sim$ $20keV$), the scattering photons are distributed approximately equally in all directions; while at high energies, the photons are forward scattered with a small scattering angle. [17] In x-ray imaging, these scattered photons can continue on to the x-ray detector, contributing to image noise and the degradation of the image contrast. Compton scattering also causes ionization in living tissue. As the incident photon energy increases, more energy is transferred to the the ejected electron, increasing the radiation dose to the object.

The cross-section of Compton scattering depends on the photon energies, when the x-ray energy between 10 keV and 100 keV, the cross-section is:[17]

$$\sigma_C^{LE} \propto Z \cdot E^0 \tag{2.5}$$

while at the high energies (> 100 keV), the cross-section is:[17]

$$\sigma_C^{HE} \propto \frac{Z}{E} \tag{2.6}$$

2.2.4: Pair Production

When the energy of an x-ray or γ-ray photon is higher than 1.02 MeV, the interaction between photon and matter results in the production of electron-positron pairs. The excessive energy is transferred to the kinetic energies of electron and positron equally. Once the positron exhausts its kinetic energy, it will annihilate with a nearby electron, producing two x-ray photons of energy of 511 keV each that are emitted in opposite directions. However, pair production only occurs at energies much higher than those used in diagnostic imaging.

Section 2.3: X-ray Attenuation

Due to the interactions of x-ray photons with matter discussed in the previous section, the combined effect is the attenuation of the x-rays, either through absorption or scattering, when x-rays pass through the material.

Consider a monochromatic x-ray beam, the attenuation of the beam intensity (I) was experimentally observed as:

$$\frac{dI}{I} = -\mu dx \tag{2.7}$$

Where μ is the constant for a given material and photon energy. The equation describes an exponential decay of the beam intensity. Given the incident beam intensity (I_0), the exit beam intensity (I) after passing a material of thickness x is:

$$I = I_0 e^{-\mu x} \tag{2.8}$$

The μ is called the attenuation coefficient, which statistically describes the probability of an x-ray photon interacting with matter. Like the individual ways of interaction, μ is strongly dependent on incident photon energy and the density of the material. Generally, high Z materials have higher attenuation coefficients. The attenuation coefficient also decreases with increased photon energies.

Simply, if the object is composed by many materials, the beam intensity after attenuation is:

$$I = I_0 e^{\sum_i \mu_i x_i} \tag{2.9}$$

Where μ_i is the attenuation coefficient of the i-th material, and x_i is the thickness of the i-th material in the beam path.

Section 2.4: Generation of X-ray

Section 2.2 briefly introduced the physical properties of x-ray, this section will focus on the generation of x-rays. X-ray, as a form electromagnetic radiation, is naturally generated through numerous physics processes, such as acceleration of charges, nuclear reactions, etc. Since the discovery of x-ray, scientists also found several ways to generate x-rays in laboratory settings. In this section, the mechanisms to produce x-rays will be briefly introduced.

2.4.1: Bremsstrahlung Radiation

Bremsstrahlung radiation occurs when one charged particle (usually electron) decelerates as it is passing by another charged particle (usually the nucleus of an atom). The energy of the photon equals the loss of the kinetic energy of the incoming charge. Thus the energy spectrum of Bremsstrahlung radiation is continuous, with the maximum possible energy equal to the kinetic energy of the incident charge. The maximum energy can only occur when all kinetic energy transfers to a single photon, in which case the probability is very small. Thus the number of photons decrease as photon energy increases.

2.4.2: Characteristic X-rays

When an electron in the inner shell of an atom is removed from the atom, an electron in the outer shell leaps from high energy state to fill the vacancy, emitting a photon during this process. The emitted photons are called the characteristic x-rays because the energies of the photons are equal to the energy differences in the two states, which are unique to a given element. Each characteristic x-ray is marked by the letter of vacant shell, with a subscript indicating whether the electron is from adjacent shell (α) or non-adjacent shell (β). For example, if an electron is ejected from the K shell of an atom, the characteristic x-ray emitted when an L shell electron fills in is called K_α, and the characteristic photon from the M shell is K_β. The characteristic x-rays are shown in the energy spectrum as discrete

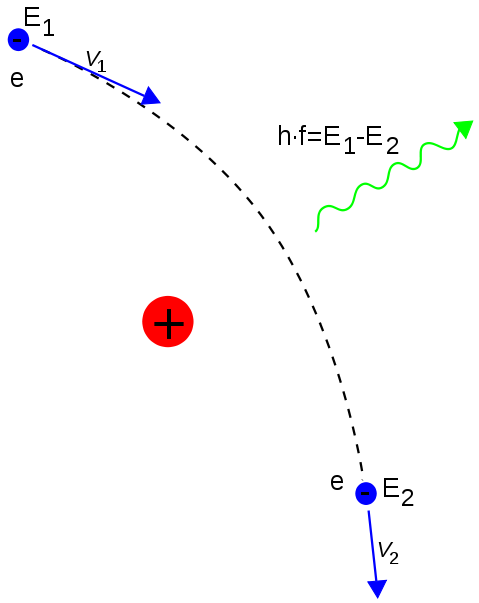

Figure 2.4: Illustration of the Bremsstrahlung radiation. An electron is deflected when passing by the nucleus of an atom, the loss of kinetic energy transfers to the x-ray photon.

lines. The K_α line is typically a doublet, with slightly different photon energy, due to the spin-orbit interaction energy between electron spin and orbit angular momentum. K_α lines are usually the strongest x-ray spectral line for an element. Figure 2.5 shows the energy spectrum of x-rays of a 90 kVp x-ray tube, with the characteristic lines marked.

2.4.3: Synchrotron Radiation

Synchrotron radiation is the x-ray radiated when charged particles are accelerated radially ($\mathbf{a} \perp \mathbf{v}$). Synchrotron radiation is generated in the synchrotrons, which uses a magnetic field to bend the trajectory of the high speed (ultra-relativisitic) charged particles (Figure 2.6). The emitted photons are highly collimated, polarized, and have high intensity. But the synchrotron facilities cost hundreds of millions of dollars to construct.

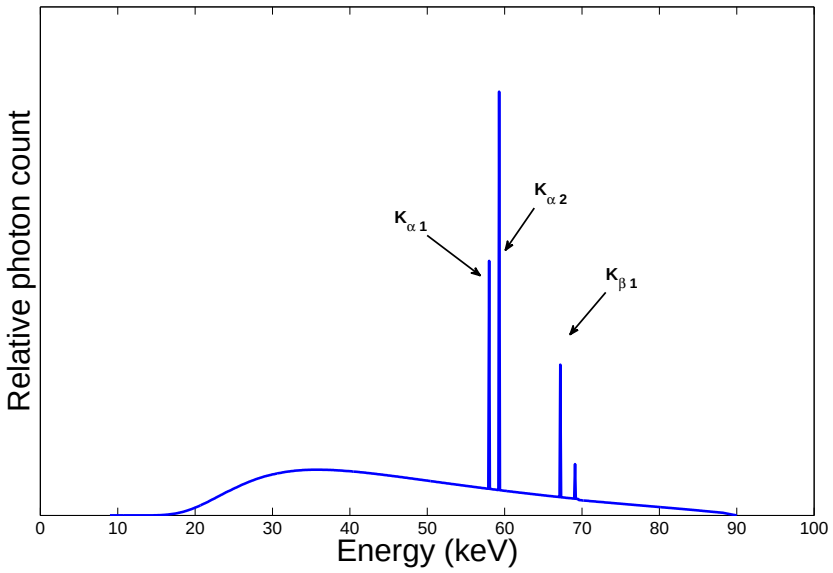

Figure 2.5: Energy spectrum of x-rays generated using a 90 kVp tube. The characteristic lines $K_{\alpha 1}$, $K_{\alpha 2}$, and $K_{\beta 1}$ are marked.

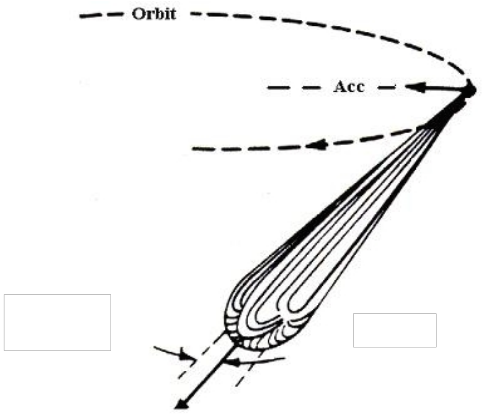

Figure 2.6: Synchrotron radiation from the bending charged beam. The radiation beam is sharply collimated forward.

Section 2.5: X-ray Tubes

Currently, an x-ray tube is the most convenient way to generate x-rays controllably. The design of x-ray tubes haven't changed significantly since William Coolidge invented the modern design of the x-ray tube in 1913 (Figure 2.7).[20]

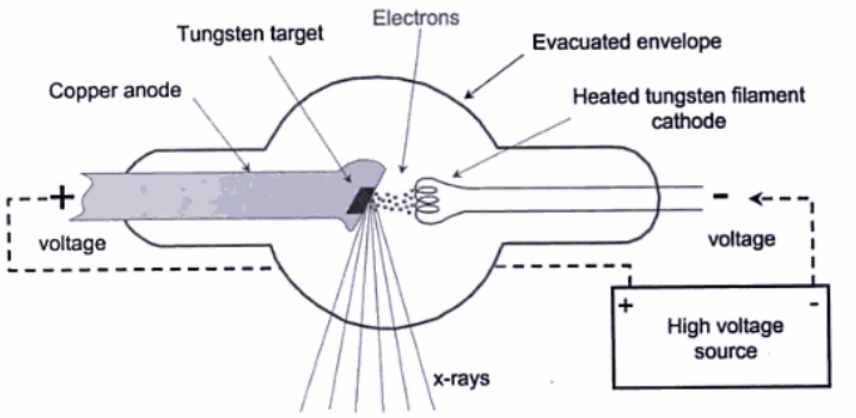

Figure 2.7: Diagram of a Coolidge tube. The major component of the tube is the cathode, the anode, and the tube housing.
[20]

The x-ray tube consists of an electron source, and an anode target in a vacuum chamber. The anode is held at high voltage. Electrons emitted from the cathode are accelerated, and bombard the target material. Bremsstrahlung radiation is the main mechanism of x-ray production. If the anode voltage is high enough, characteristic radiation of the anode material is also generated.

2.5.1: Cathode

The cathode is the electron source in x-ray tubes. In conventional x-ray tubes, it is usually made of high melting temperature material, typically tungsten (W). The tungsten wire is machined to a helical spiral shaped filament. When operating, a small voltage is applied to the cathode (around 10 V), generating a current up to 7 A.[20] The heat generated in the filament increases the energy of the electrons. Once the energy is greater than the work

function of the metal, electrons are emitted from the cathode, which is called thermionic emission. In most modern tubes, a focusing cup electrode is placed behind the filament and at a negative voltage, propelling the emitted electrons to focus into a spot.

2.5.2: Anode

The anode in the x-ray tube is applied a positive high voltage.[1] The electrons emitted from the cathode are accelerated by the electric field generated by the high anode voltage. The potential energy of the electric field is transferred to the kinetic energy of the electrons. The high speed electrons bombard the surface of the anode and penetrate into the target material. The electrons decelerate after hitting the anode, generating x-ray due to the Bremsstrahlung effect. If the electron energy is high enough, characteristic x-rays are also produced.

Over 99% of the energy of the electrons is transferred to heat. High atomic number targets yield to higher x-ray production efficiency. Therefore, high melting temperature and high atomic number materials are preferred for the anode. Tungsten, with a melting temperature of 3695 K and atomic number of 74, is the most commonly used anode material. When the electrons hit the anode surface, the penetration depth is on the order of a few hundred micrometers,[21] thus most heat is generated at the surface of the anode. To prevent anode cracking and pitting, an alloy of 10% rhenium (Re) and 90% tungsten is used to provide better resistance to surface damage.[20]

The anode heat load is a crucial issue to consider when designing the x-ray tube. For a low power tube, a stationary anode with highly conducting backing (typically copper) is used. However, to prevent anode damage, a rotating anode is often used in modern high power tubes. The rotating anode consists of the anode disk, the stem, and the rotor. Typical rotation speed of the anode is 3,000 RPM to 9,000 RPM.

[1] For medical imaging, the high voltage typically ranges from 20 kVp to 200 kVp.

2.5.3: Focal Spot

The electron trajectories are focused by the electric field. The area where electrons bombard the anode target is called the focal spot. The size of the focal spot is very import in x-ray imaging due to its direct involvement in the image resolution. Smaller focal spots yield to better spatial resolution.

For conventional x-ray tubes, the actual focal spot size depends on the size and shape of the filament. Since most filaments are long and thin, the focal spot is elongated in one direction, causing asymmetric spatial resolution in the image. To compensate for this, the anode and the detector are usually placed at an angle. This angle is referred as anode angle θ. The effective focal spot is the projected focal spot on the detector plane. The length of the effective focal spot is the actual focal spot length times $\sin\theta$. The anode angle affects the field of view and the effective focal spot. Figure 2.8 illustrates this relationship. Generally, a small anode angle ($\sim 7^\circ - 9^\circ$) is desirable for small field of view applications, such as dental x-ray; while a larger anode angle ($\sim 12^\circ - 15^\circ$) is preferred for general radiographic applications.[20]

For most diagnostic imaging systems, the effective focal spot is isotropic, so that the image has the same spatial resolution along all directions. The (effective) focal spot size of an imaging system depends on the tradeoff between the imaging resolution requirement for the imaging task, the field of view, x-ray flux requirement, and anode heat load.

2.5.4: Tube Housing and Filtration

The cathode and anode are required to be placed in a vacuum environment to ensure the passing of electrons. The tube housing serves as a vacuum barrier. In addition, the housing also provides initial x-ray shielding, since the x-rays are produced in every direction. Dense materials, such as lead, are typically used for radiation shielding in the tube housing.

The x-ray window provides an exit for the x-rays from the tube housing. It is made of thin and light material, such as glass, beryllium, or aluminum. The x-ray window is also

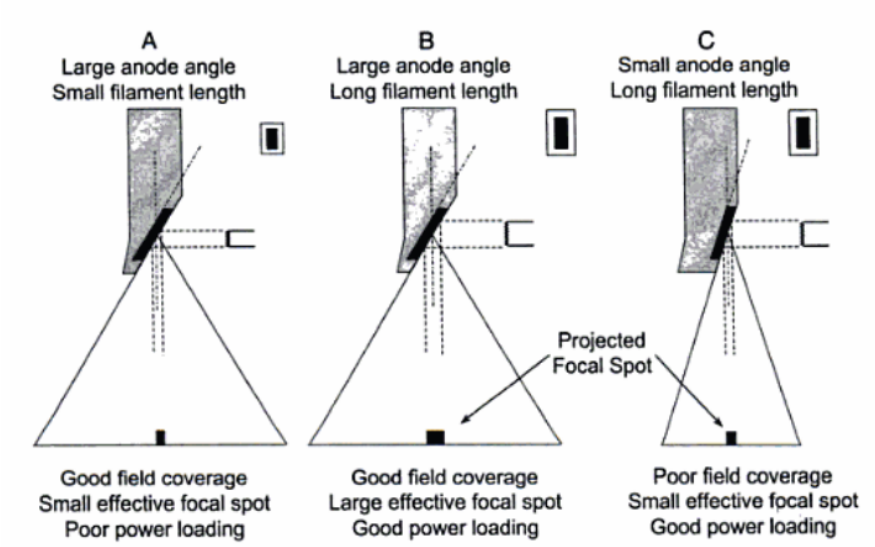

Figure 2.8: Illustration of the field of view and effective focal spot with respect to anode angle.

[20]

called the inherent filtration, since the window material also provides filtration to the x-ray spectrum. In addition to the inherent filtration of an x-ray tube, thin layers of material (typically aluminum) are also mounted outside the window for additional filtration of the beam. The filtration in an x-ray tube attenuates low energy photons to improve the beam quality. Since the low energy photons have little chance of passing through the patient in diagnostic imaging, filtering out this part of photons reduces the radiation dose to patient. The beam quality is quantitively measured by the half value layer (HVL) of the x-ray beam. HVL gives a measure of the effective energy of the beam. It is defined as the thickness of aluminum (in mm) required to reduce the intensity of the x-ray beam to half. The effective attenuation coefficient of aluminum μ_{eff}^{Al} can be calculated from HVL:

$$\mu_{eff}^{Al} = \frac{\ln 2}{HVL} \tag{2.10}$$

By looking up the attenuation coefficient, the effective beam energy can be found. Increasing the additional filtration increases the HVL.

Table 2.1: Excerpts of FDA HVL regulations for an x-ray tube operated between 60 kVp and 120 kVp.

X-ray Tube Voltage (kVp)	Minimum HVL (mm of aluminum)
60	1.5
70	1.8
71	2.5
80	2.9
90	3.2
100	3.6
110	3.9
120	4.3

In the United States, the Food and Drug Administration (FDA) regulates the beam quality of x-ray for diagnostic imaging. All diagnostic imaging equipment must comply with the minimum HVL requirement specified in Title 21 of the Code of Federal Regulations.[22] Table 2.1 is an excerpt of HVL regulations for x-ray tubes between 60 kVp and 120 kVp.

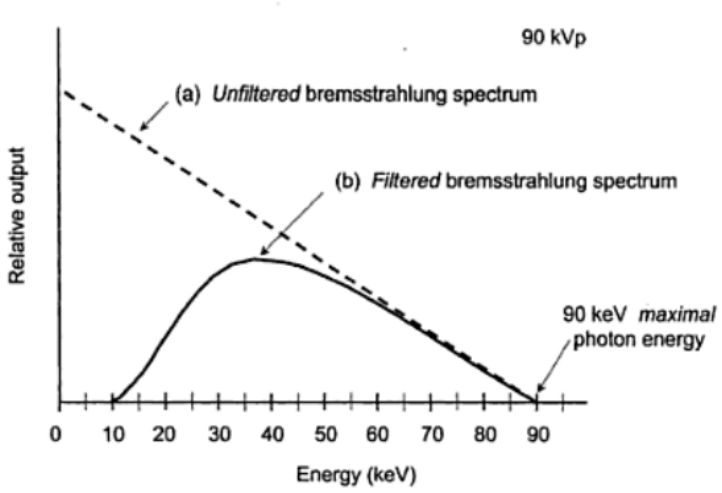

Figure 2.9: Illustration of the effect of x-ray tube filtration on x-ray spectrum. (a) Shows the unfiltered Bremsstrahlung spectrum with great low-energy x-ray photon production. (b) Shows the filtered spectrum with preferential attenuation on the low energy photons. [20]

With the tube filtration, a large number of low energy photons that do not contribute

to imaging are removed from the energy spectrum. The benefits of filtration are (1) reducing unnecessary radiation exposure to the patient; and (2) reducing scattering and its degradation to image quality. Figure 2.9 illustrate the filtered spectrum from a 90 kVp tube.

CHAPTER 3: Digital Chest Tomosynthesis

Section 3.1: X-ray Imaging Modalities for Chest

There are three x-ray imaging modalities used in the clinic for chest examinations: chest x-ray radiography (CXR), computed tomography (CT), and digital chest tomosynthesis (DCT). This section will provide a brief introduction on each modality.

3.1.1: Chest X-ray Radiography

Chest x-ray radiography (CXR) is the most commonly practiced imaging procedure.[1] It is frequently the first imaging test performed on patients with known or suspected lung disease. It has been used for the diagnosis of diseases related to lungs and hearts such as infectious diseases, malignancies, airway diseases, interstitial diseases, bone diseases, and evaluation of trauma.

Different views of CXR can be obtained by changing the orientation of the chest and the direction of the incident x-ray beams. Posteroanterior (PA), anteroposterior (AP), and lateral views are the most common CXR views. The PA view is typically acquired with the patient standing up straight, in front of detector. The x-ray source is positioned behind the patient so that the x-ray beam can enter the posterior aspect (back) of the chest and exit from the anterior aspect (front) of the chest. In this exam, the source-to-image distance is typically 1.8 m.

With the advancement of technology, the digital flat panel detector has been replacing conventional film and imaging cassette as the image receptor. The digital detector also lowers the radiation dose delivered to patients due to its high dose efficiency.[23] CXR is normally acquired at 80 kVp - 120 kVp, while the technique (mAs value settings used in exam) is

determined using automatic exposure control (AEC).[3] The AEC chambers are embedded in the detector housing and are used to measured the radiation dose reaching the detector after passing through the patient. Once the reading from AEC reaches the designated value, it cuts off the x-ray output so that a reasonably good quality image is acquired at the lowest possible dose. For chest imaging, the AEC chambers are typically placed in the lung regions.

Despite the low radiation dose, low cost, and high accessibility, there are several challenges for CXR. In CXR images, a 3D object is projected onto the 2D imaging plane. Organs and tissues along the path of x-ray beam are superimposed, resulting in loss of "depth resolution". Besides, the superposition of anatomical features may hide a lesion, leading to low sensitivity for the exams.

3.1.2: Computed Tomography

Until the invention of CT in 1972, x-ray imaging relied on 2D radiography. CT enables true 3D x-ray imaging. A CT scanner consists of an x-ray tube and a detector. But instead of fixing the positions of x-ray source and detector during image acquisition, both are mounted on a gantry and rotated around the object. The purpose of rotation is to allow x-rays to pass through all portions of the body through sufficient paths, so that the fully sampled object can be reconstructed using computers.

The principle of CT reconstruction is to calculate the attenuation coefficient of the material.[2] 3D datasets were calculated, and the value of each voxel is the CT number. The dataset is sliced along a certain direction and a stack of cross-sectional images are presented to the physicians.

The CT images solve the tissue overlap issue in conventional radiography images, thus increases the visibility of lesions. The additional "depth" resolution better represents the anatomic structures, as well as the localization of the lesion. However, due to its complex mechanical structures, CT machines are very expensive, leading to high examination costs compared to radiography. In addition, the huge number of projection images acquired by

CT results in high radiation dose to the patient. Studies have shown that the average dose of a two-view CXR is less than 1% of that of chest CT.[3]

However, due to cost, workflow, and radiation dose concerns, it is unlikely that CT will supplant CXR in the near future for general chest imaging. Therefore, an alternative low dose 3D imaging modality is desirable.

3.1.3: Digital Chest Tomosynthesis

DCT is an emerging low-dose tomographic imaging modality. It utilizes a small number of projection images acquired over a limited angle to produce quasi-3D image datasets. The technique yields some of the tomographic benefits of CT, but at lower cost and dose. It has been shown that the average dose of DCT is approximately 2% of chest CT.[3]

Section 3.2: Digital Tomosynthesis

3.2.1: Principles of Chest Tomosynthesis

The term "tomosynthesis" was introduced by Grant in 1972.[24] It was combined from two Greek words: "toms" – a section, a slice – and "synthesis" – combining two or more pre-existing elements to get something completely new. Grant proposed a technique that uses a small number of projections to generate 3D images. However, it was not widely implemented until the development of digital detectors.

Current digital chest tomosynthesis (DCT) is illustrated in Figure 3.1. The system includes a conventional x-ray source, a computer controlled gantry that can be moved to various locations along a vertical path, a flat panel detector, and control electronics. The patient is positioned in front of a stationary detector, usually in PA position, as in CXR. Images are acquired and readout during the course of the tube movement.

The projection images are reconstructed to a stack of slices, each is parallel to the detector and focused at a specific height. The traditional method to reconstruct the tomosynthesis

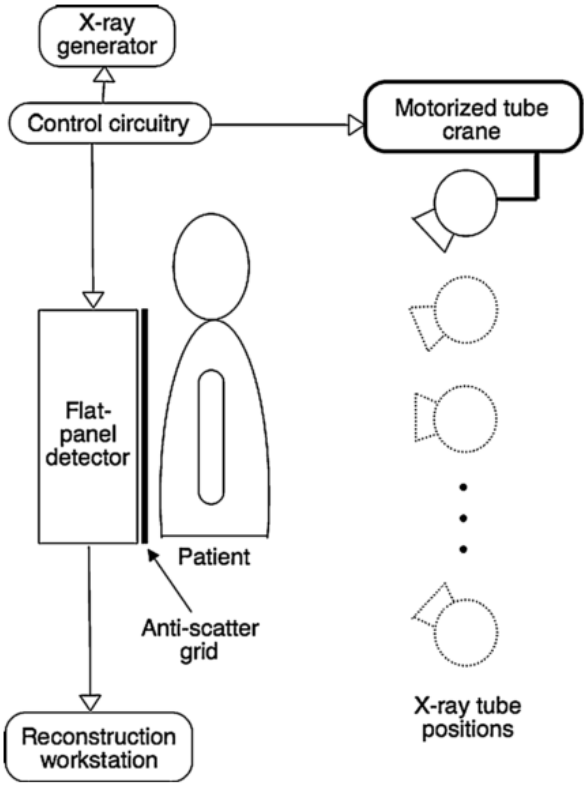

Figure 3.1: Illustration of a DCT system. The system consists of a computer controlled gantry that can move the x-ray source to various locations long a vertical path, a flat panel detector, and computers.

[1]

image is the shift-and-add technique, as illustrated in Figure 3.2. The shift-and-add technique is similar to the back projection technique in CT reconstruction. By shifting and adding the projection images, composite image slices at different planes are generated. Each plane is at a specific height. Only the object in the plane shows clearly in the reconstructed slice (Figure 3.2(B)). By scrolling through the reconstructed image set, different objects come in focus at different slices, while the object at other planes blurs out as artifacts.

However, traditional shift-and-add technique results in substantial blur artifacts. Deblurring techniques are always used to render clearer images. Besides the shift-and-add technique, filtered back projection and iterative algorithms have been also developed.[25]

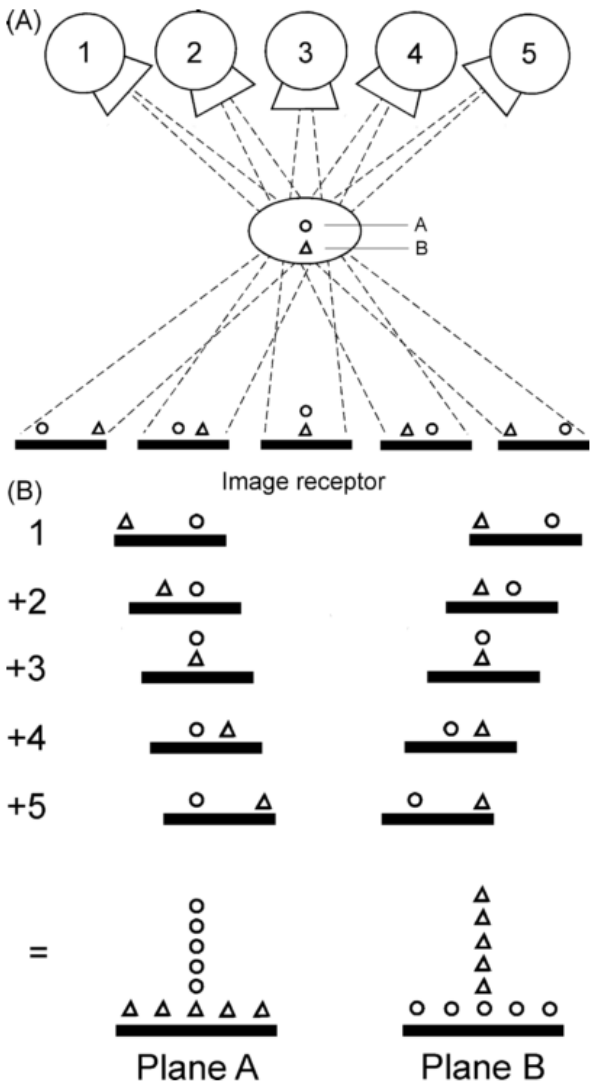

Figure 3.2: Shift-and-add technique for tomosynthesis image reconstruction. In this illustration, five projection views are used for tomosynthesis reconstruction. The five images are shifted and added to yield composite images at two different planes. Different objects come in focus at different imaging planes.

[1]

3.2.2: Commercial DCT Systems

Currently, several DCT systems have been developed and used in the clinic.[1, 8, 10, 26, 13, 27] These systems were mostly based on clinical in-room digital radiography system. The prototype scanner developed at Duke University was reported to perform a tomosynthesis

scan of 71 projections over a 20° angular span, within 11 s.[1, 8]

GE has developed a tomosynthesis option for their in-room digital radiography (DR) system. With the VolumeRAD option, the x-ray tube in the DR system can be moved in a vertical path to perform tomosynthesis with a variable source-to-detector distance of 180 cm -187 cm, as shown in Figure 3.3. A typical tomosynthesis scan takes 10 s and includes 61 low dose projections over 30°.[10, 28] The tomosynthesis radiographic technique varies from patient to patient. The mAs per projection was determined using a scout view. [3, 27, 9]

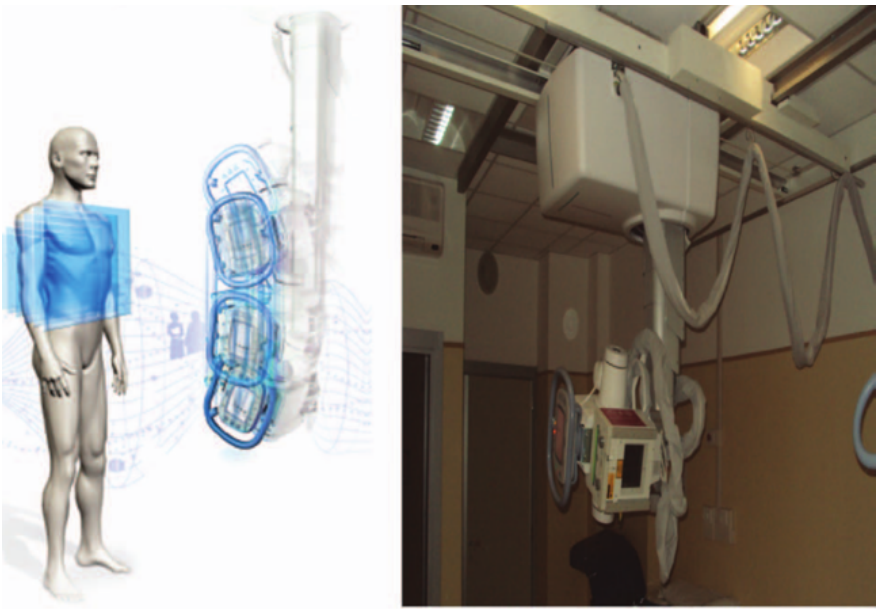

Figure 3.3: Illustration and photo of GE VolumeRAD DCT system.
[27]

The relatively long scanning time, approximately 10 s, leads to image blur due to patient motion.[13] Shimadzu developed a fast tomosynthesis system. In the Shimadzu SONIALVISION (Shimadzu, Japan) DCT, both the x-ray tube and the detector move linearly in opposing directions. As illustrated in Figure 3.4, the patient is placed on the imaging bed in the AP chest position. The bed is tilted to 80°. A set of 74 projections are acquired over a 40° angle in 5 s.[13] Table 3.1 summarizes the key specs of current DCT systems.

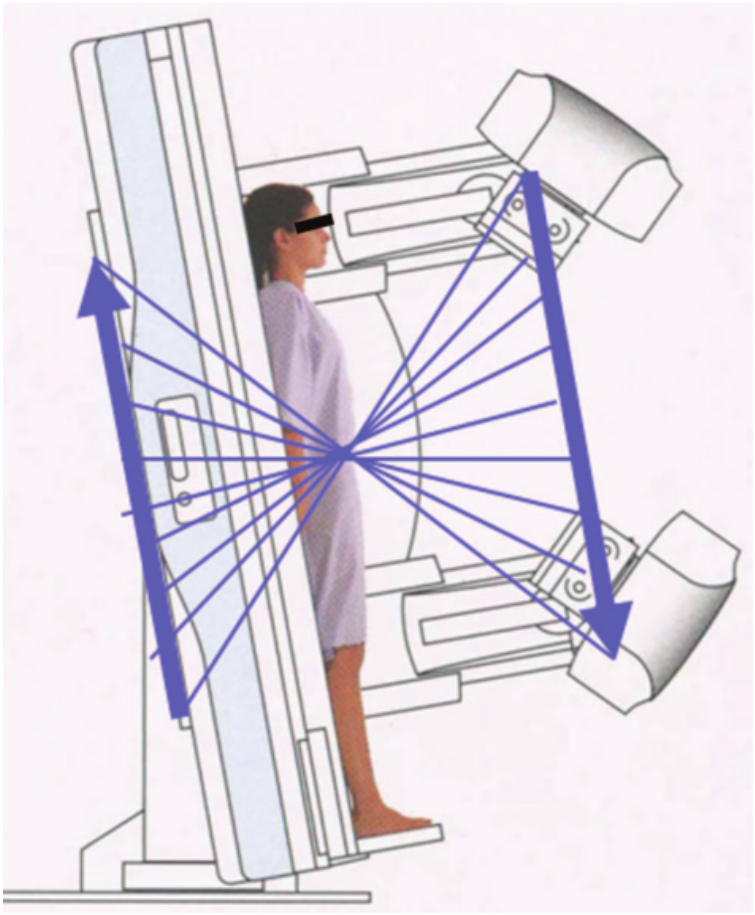

Figure 3.4: Illustration of Shimadzu SONIALVISION DCT system. [13]

Table 3.1: List of key specs of the commercial DCT systems.

Commercial systems	GE VolumeRAD	Shimadzu Safire
Anode kVp	80 - 120	80 - 120
SID	180 - 187 cm (PA) 110 - 120 cm (AP)	110 - 130 cm (AP)
Number of projections	60	74
Angular coverage	30° - 35°	40°
Scanning time	10 s	5 s
Focal spot size	0.6 mm/1.2 mm	0.4 mm
mAs per projection	1/6 of CXR	N/A
In-plane resolution	3.5 cycles/mm[29]	3 cycles/mm[30]

3.2.3: Dosimetry of DCT Systems

DCT acquires low dose projection images to reconstruct tomosynthesis datasets. Currently, most DCT uses the following protocol to determine the radiographic technique. When a patient is positioned, a scout view, which is a standard PA radiograph image using AEC, is acquired first. The technician uses this image to check the patient position and determine the technique for DCT acquisition. The mAs value from the scout view is multiplied by a constant, typically 10, and then divided by the total number of the projection views (61 for GE's VolumeRAD system), to calculate the mAs setting for each projection.[3] For some of GE's DCT system, the base DR system only has discrete settings for mAs. Thus the number is usually rounded down to the closest setting.[9]

In medical imaging, the effective dose is commonly used to measure the risk of radiation exposure. For standard chest CT, the effective dose is about 7 mSv.[3] For PA CXR, the average effective dose is around 0.017 mSv, while the two-view (PA + Lateral view) is 0.056 mSv.[3] Multiple studies have evaluated the effective dose for DCT. For adults, the average effective dose for a standard sized patient is approximately 0.1 mSv - 0.2 mSv.[3, 10, 13, 9]

3.2.4: Diagnostic Accuracy of DCT

Recently, the potential of DCT for diagnosing lung disease has been investigated. Detection of pulmonary nodules, a pathology usually related to lung cancer, is one of the most challenging tasks in chest imaging.[1] Several studies have been performed to evaluate the detection the lung nodules using DCT compared to CXR and chest CT, the current gold standard. Table 3.2 summarizes the diagnostic accuracy of DCT. It is shown that DCT has comparable sensitivity for detecting lung nodules compared to CT, for nodules larger than 5 mm, while at a low cost and effective dose. In addition to pulmonary nodules, DCT has shown increased diagnostic accuracy compared to CXR for other lung pathologies, such as bronchiolitis, pulmonary consolidation, pulmonary emphysema, and cystic fibrosis.[31, 11, 12]

Table 3.2: Comparison of CXR, DCT and CT for detection of lung nodules with CT as reference

	3 - 5 (mm)	5 - 8 (mm)	> 10 (mm)	Effective dose (mSv) [3, 9]	Cost
CT	100%	100%	100%	2 - 7	High
CXR	7% [8]	19% [27]	63.6% [27], 53% [8]	0.02 - 0.06	Low
DCT	53% [8]	91.4% [27]	100% [27], 90% [8]	0.1 - 0.2	Medium

3.2.5: Limitations of Conventional DCT

Current DCT scanners collect projection images by mechanical translation of a single x-ray tube to different viewing angles, resulting in (1) long scan time, and (2) relatively low depth resolution. The imaging time of the current DCT scanners is longer than a human respiratory cycle, which is about 3 - 6 s.[32] Image blurring caused by respiratory motion, even if the projection images are collected within a single breath-hold, significantly reduces the system spatial resolution and sensitivity, especially for small nodules. This contributes to the significant drop in the detection sensitivity of DCT for small nodules compared to CT.[1] A recent study by Kim et al. concludes that when there is no respiratory motion artifact, the detection sensitivity of DCT for nodules is significantly better than that of CXR. But, when motion artifacts are present, the sensitivity of DCT is reduced to the level of CXR.[14] The mechanical translation mechanism limits the angular coverage, which results in a low depth resolution. Several studies reported the challenges of using DCT to localize pleural and subpleural nodular lesions.[33] The limited depth resolution also leads to artifacts, which is of special concern when high-density objects are superimposed on tissue with low density.[10]

CHAPTER 4: Carbon Nanotube X-ray Source

Section 4.1: Carbon Nanotube

Carbon nanotubes (CNTs) are allotropes of carbon with cylindrical crystal structure which was first discovered in 1991.[34] CNTs are members of the fullerene structure family. CNTs are long, hollow shaped tube structures with a high aspect ratio. Their walls are formed by graphene. Based on the number of layers, CNTs can be categorized as single-walled nanotubes (SWNTs) or multi-walled nanotubes (MWNTs). The diameters of SWNTs range from 0.4 nm to 2 nm, while those of MWNTs are between 2 nm to 100 nm. CNTs can be considered as graphene rolled at specific angles. The different ways of rolling result in a variance in properties of CNTs, such as metallic or semiconducting. [35]

CNTs can be synthesized using multiple techniques, such as arc discharge, laser ablation, chemical vapor deposition, etc.[36] Sumio Iijima synthesized the first CNTs using the arc discharge method in 1991.[34] Mass production of nanotubes is now available.[36]

Section 4.2: CNT Based Field Emission X-ray Source

4.2.1: Field Emission Effect

As discussed in Section 2.5, cathode is an important part of the x-ray tube, which provides electrons to generate x-rays. In the conventional x-ray tube, a tungsten filament is the most commonly used electron source. The filament is heated up to a high temperature, at which the energy of electrons exceeds the work function of the tungsten (approximately 4.5 eV). Electrons are emitted from the surface of the filament. The current density from thermionic

emission is described by the empirical formula:

$$J = (1 - r_{av}) A_0 T^2 e^{-\frac{\phi}{kT}} \tag{4.1}$$

Where r_{av} is the reflection rate of outgoing electrons at the surface, T is the temperature of the filament, k is the Boltzmann constant, ϕ is the work function of the material, and A_0 is a constant given by

$$A_0 = \frac{4\pi m k^2 e}{h^3} = 1.2 \times 10^6 A m^{-2} K^{-2} \tag{4.2}$$

The emission current increases as temperature rises. Using a material with high melting temperature, current density of conventional thermionic filaments can be up to 1000 mA/cm^2.

In 1928, Ralph H. Fowler and Lothar Wolfgang Nordheim discovered the field emission effect.[37] Electrons are emitted by applying an external electric field to the material, instead of heating up the material, thus it's also called "cold electron emission". The presence of the external electric field lowers the effective work function, so the electrons near the Fermi surface can tunnel through the potential barrier, as illustrated in Figure 4.1.[38] The emission current density is determined by the Fowler-Nordheim equation:[38]

$$J = a \frac{F^2}{\phi} e^{-\frac{b\phi^{3/2}}{F}} \tag{4.3}$$

Where a and b are constants with values of $1.54 \times 10^{-6}\ A \cdot eV \cdot V^{-2}$ and $6.83\ eV^{-3/2} \cdot V \cdot nm^{-1}$, respectively. F is the applied electric field. The derivative of the current density

$$\frac{\mathrm{d}J}{\mathrm{d}F} \propto F e^{-\frac{1}{F}} \tag{4.4}$$

shows the field emission current increases exponentially as the applied electric field. The Fowler-Nordheim equation also shows that the field emission current is easier to modulate compared to that of thermionic emission, since current is solely dependent on the applied electric field, which is easier to control compared to the temperature of a filament.

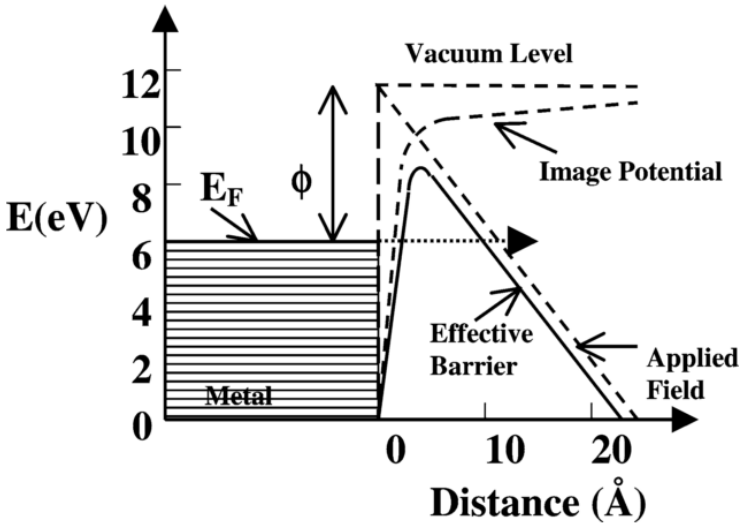

Figure 4.1: Illustration of the field emission effect. The application of the electric field lowers the effective barrier so electrons near the Fermi level can tunnel through the barrier. [39]

4.2.2: X-ray Source Using CNT Field Emitters

The high aspect ratio of CNTs makes CNTs excellent field emitters. Due to the sharp tip of CNTs, an enhanced field is created, which makes electrons easier to tunnel through the energy barrier.[40] CNTs have been studied as field emitters as early as 1995.[41] Early applications of CNT field emitters includes using CNT-based field emission displays,[42] and CNT as electron sources in x-ray tubes.[43]

Our lab at UNC built its first CNT based x-ray source over a decade ago, using single-walled carbon nanotubes.[44] The cathode was made of purified SWNT bundles, which had an average diameter of 1.4 nm and average bundle size of 50 nm.[44] Figure 4.2 shows the schematic of this early x-ray tube and sample images of a fish and human hand phantom. The tube anode was made of copper, and had a gated cathode assembly in a concealed vacuum chamber. The cathode assembly includes the cathode and gate mesh, which was a metal grid placed 50 $\mu m - 200$ μm away from the cathode, and was grounded. A negative voltage was applied to the cathode and positive high voltage was applied to the anode. Due

to the power limit and vacuum conditions of this tube, the anode voltage was set to 14 kV.

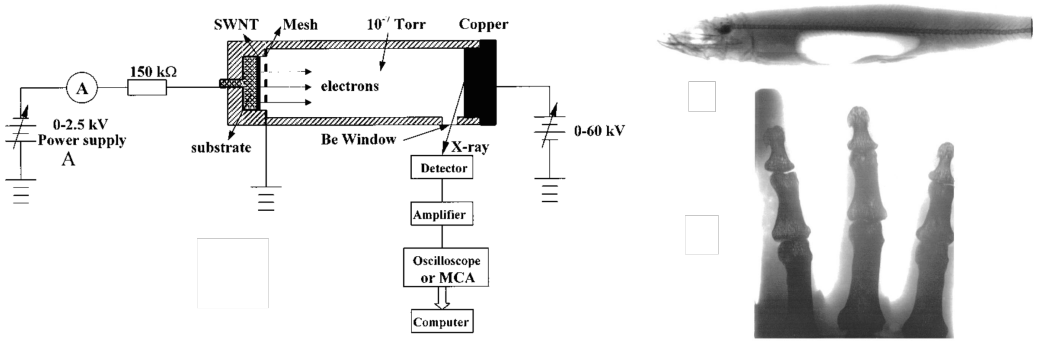

(a) (b)

Figure 4.2: (a) Schematic of the triode-type field emission x-ray tube. (b) X-ray images of a fish and human hand phantom taken using the CNT x-ray source.
[44]

Currently, all CNT-based x-ray sources developed at UNC use the triode electric design: CNT cathode, gate electrode, and anode.[45–49] The entire tube is kept at a high vacuum state approximately 10^{-9} *torr*. Figure 4.3 illustrates the typical design of the CNT x-ray sources. The cathode is bulk molybdenum substrates with CNTs deposited on top. The area of the deposited CNTs varies depending on different applications. The gate electrode consists of a mesh of tungsten bars.[50] Gate-cathode voltage (V_{gc}) on the order of 1000 - 2000 V is applied either on the gate or cathode, with the other grounded.[1] Switching electronics are typically required to enable the switch of the V_{gc} so the source can be operated in pulsed mode. The focusing electrodes are designed to provide an electric field distribution between the gate and anode to bend trajectories of electrons. Either positive or negative voltage is applied on the focusing electrodes. The shape and the size of the electrodes, and the voltage applied are dependent on the intended focal spot size.[50] A DC high voltage, ranging from 30 kVp to 160 kVp, for different imaging and therapy applications, is applied on the anode. The anode used in CNT x-ray sources is a stationary tungsten anode. Due to the triode

[1]Two situations: (1) Gate is grounded, the cathode has a negative voltage applied to it. (2) Cathode is grounded, the gate has a positive voltage applied on it.

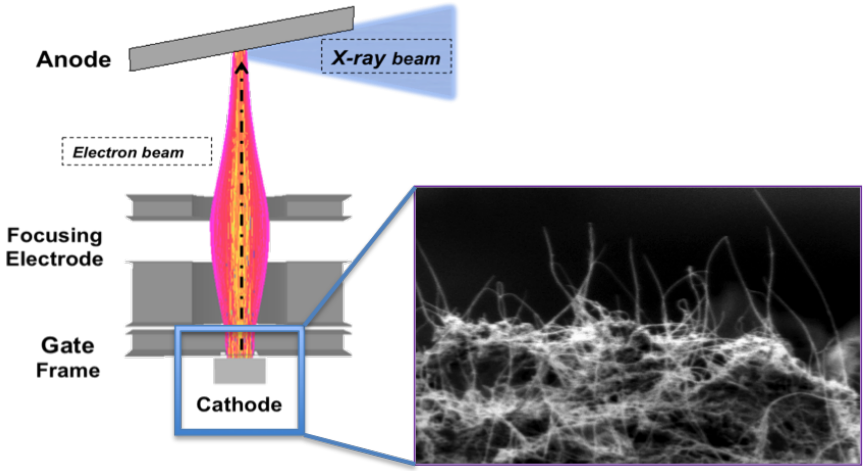

Figure 4.3: Schematic of the typical CNT source design. The source consists of a CNT cathode, gate and focusing electrodes, and anode. The anode has high voltage applied, while a smaller voltage (in the order of 1000 V) is applied between the gate and cathode. The blue box shows a picture of a representative cathode surface with CNTs, captured by scanning electron microscope (SEM).

design, the current emitted from the cathode may leak to the gate electrode, and the focusing electrodes in some cases. Therefore, the current that reaches the anode (also called as anode current or tube current), which is the current that actually generates x-rays, is less than the field emission current from the cathode. The ratio of tube current to the cathode current is defined as the transmission rate. Typical transmission rate of the CNT x-ray source is around 60% to 70%.

Similar to conventional x-ray sources, in the design of a CNT x-ray source, the main issues that need to be considered are tube rating (in kVp), tube output (in mA), and focal spot size. The anode voltage rating is determined by imaging or therapy applications. The high voltage feedthrough and spacing between electrodes need to be designed to prevent arcing. Higher tube current allows shorter pulses at a given exposure (in mAs), which is extremely beneficial for diagnostic imaging. The maximum tube current is dependent on the heat management of the anode. Given a focal spot and anode material, the maximum power applied on the anode can be derived from simulation using the finite element analysis (FEA) method.[51] The maximum tube current is calculated as the maximum power divided

by anode voltage. For the CNT x-ray source, the tube current is an interplay of cathode emission current and transmission rate. The current from the CNT cathode depends on many factors such as density of CNTs, area of deposited CNTs, voltage between gate electrode and cathode, and gate mesh design. Higher density and larger area of the CNT deposit increases the total number of CNT emitters, thus producing higher current output at the same operating condition. The mesh design, i.e. spacing and shape of the gate mesh, affect the electric field distribution between the gate and cathode at a given V_{gc}, as well as the transmission rate. The focal spot size, which plays an important role in determining an imaging system's spatial resolution, is heavily dependent on the electric field distribution between the gate, focusing electrodes, and anode. These parameters are not isolated, and need to be considered thoroughly. The anode heat management and focusing electric field design were studied using FEA simulations.[50, 51]

Section 4.3: CNT X-ray Source Applications

The compact design of source, instantaneous switching, and flexibility of cathode shape give CNT x-ray sources advantages over conventional thermionic sources. Current applications of CNT x-ray sources include: micro-CT, stationary digital breast tomosynthesis (s-DBT), stationary digital chest tomosynthesis (s-DCT), stationary CT, and micro beam radiation therapy(MRT).

4.3.1: Micro-CT

Micro-CT is a useful imaging modality for small animal imaging in pre-clinical studies.[52–54] Micro-CT has very high spatial resolution. However, *in-vivo* imaging of mice is a challenge for conventional micro-CTs due to the very fast respiration and cardiac cycles. Retrospective gating is frequently used, however, the excessive radiation exposure to mice may be a concern for longitudinal studies.[53] CNT x-ray sources have instantaneous turn-on and off capabilities, therefore enabling the prospectively gated imaging. [45, 55] Figure 4.4 shows

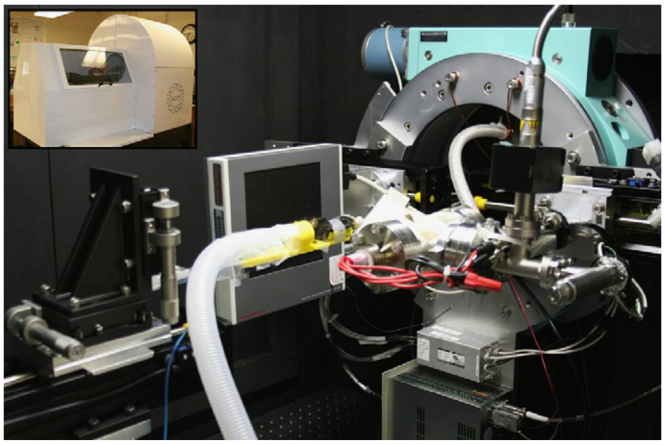

(a)

(b)

Figure 4.4: Micro-CT using a CNT based x-ray source. (a) System setup of the micro-CT. The inset shows the system with the cover and shielding. (b) Reconstructions of the micro-CT datasets of a mouse gated to both cardiac and respiration cycles.
[54]

the system setup of the CNT-based micro-CT scanner developed at UNC. The scanner consists of a micro-focus x-ray tube with a 100 μm effective focal spot size. The respiration and cardiac cycles were monitored using sensors. Images can be gated to any phase of the respiration and/or cardiac cycle.[56] Figure 4.4(b) shows an example reconstructed image of a free-breathing mouse gated to both cardiac and respiratory cycles.

Figure 4.5: A photo of the s-DBT system under clinical evaluation in the N.C. Cancer hospital.

4.3.2: s-DBT

As discussed in Chapter 3, conventional DTS utilizes a single rotating x-ray tube.[4] For digital breast tomosynthesis (DBT), the rotation of the source during image acquisition decreases the spatial resolution due to the source motion blur, which degrades the visibility of the microcalcifications.[57] An s-DBT system has been developed using the distributed CNT source array.[46, 47] The s-DBT has shown improved image resolution and image acquisition time compared to conventional DBT.[47] The s-DBT system is currently being evaluated in clinical trials. Figure 4.5 shows the s-DBT system installed in the N.C. Cancer hospital, under clinical evaluations. The CNT source array has 31 focal spots.

4.3.3: Stationary CT

Conventional CT systems use a single x-ray source mounted on a gantry and rotated around the isocenter to acquire images. The gantries in the current CT systems are usually mechanically complex, large in size, and heavy. Studies have been done to explore the

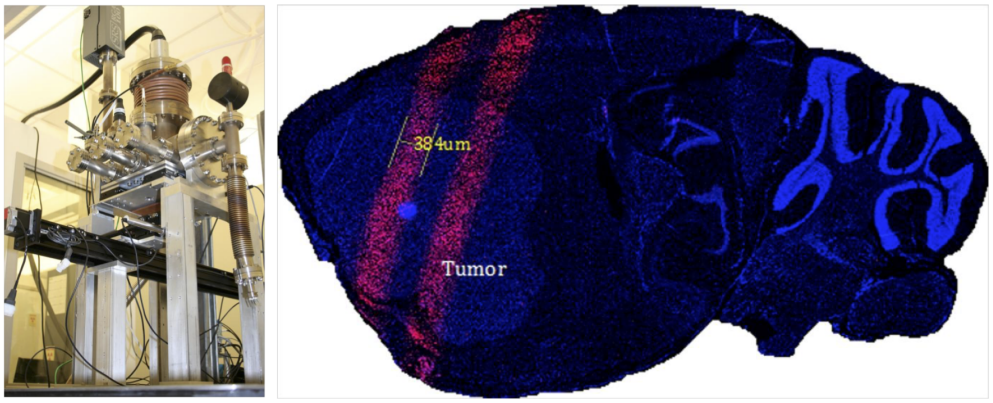

(a) (b)

Figure 4.6: Desktop micro-beam radiation therapy system using CNT x-ray sources. (a) The picture of the system setup. (b) A histological slice of a mouse brain showing the DNA damage of tumor cells by the micro-beam.

feasibility of non-rotating CTs using multiple thermionic x-ray sources.[58] However, due to the size of the conventional x-ray tubes, building a CT system using fixed multiple sources results in a large distance between x-ray sources, thus under-sampling the CT scan. The compact design of the CNT x-ray sources allows the close packing of sources. A rectangular shaped stationary CT using CNT source array has been constructed for luggage scanning.[59, 60] The system consists of two CNT source arrays and two linear detectors.

4.3.4: MRT

Micro-beam radiation therapy was a radiation therapy method developed at synchrotron facilities a few decades ago.[61] The high flux and high collimation of the synchrotron beam allows for therapy using micro-beams, which are collimated beams with high dose "peaks" (on the order of 100 μm) and low dose "valleys". The "peak" to "valley" dose ratio can be kept high. It is found that micro-beams spare normal tissue while killing the tumors.[61] The mechanism of MRT is currently unclear and needs further study. However, the micro-beam is only available at a limited number of synchrotron facilities around the world. These facilities are expensive to build and run, thus limiting the research of MRT. Using a CNT

source array with long narrow focal spots, a desktop MRT system was constructed.[48] The system is able to produce a 300 μm wide micro-beam at a dose rate of 2 Gy/s. Figure 4.6 shows the system setup of MRT in the lab and a histology of a mouse brain demonstrating the therapeutic effect of the micro-beam. The compact size and the relatively low cost of the desktop MRT would allow more research on MRT and future implementation of the technology in the clinic.

CHAPTER 5: Feasibility of a Stationary Chest Tomosynthesis System Using CNT Source Array

Section 5.1: Overview

Chest tomosynthesis is a low-dose, quasi-3D imaging modality that has been demonstrated to improve the detection sensitivity of small lung nodules, compared to 2D chest radiography. The purpose of this chapter is to investigate the feasibility and system requirements of stationary chest tomosynthesis (s-DCT) using a spatially distributed carbon nanotube (CNT) x-ray source array, where the projection images are collected by electronically activating individual x-ray focal spots in the source array without mechanical motion of the x-ray source, detector, or the patient.

A bench-top system was constructed using an existing CNT field emission source array and a flat panel detector. The tube output, beam quality, focal spot size, system in-plane and in-depth resolution were characterized. Tomosynthesis slices of an anthropomorphic chest phantom were reconstructed for image quality assessment. All 75 CNT sources in the source array were shown to operate reliably at 80 kVp and 5 mA tube current. Source-to-source consistency in the tube current and focal spot size was observed. The incident air kerma reading per mAs was measured as 74.47 uGy/mAs at 100 cm. The first half value layer of the beam was 3 mm aluminum. An average focal spot size of 2.5 $mm \times 0.5$ mm was measured. The system MTF was measured to be 1.7 cycles/mm along the scanning direction, and 3.4 cycles/mm perpendicular to the scanning direction. As the angular coverage changed from 11.6° to 34°, the full width at half maximum (FWHM) of the artifact spread function improved greatly from 9.5 mm to 5.2 mm. The reconstructed tomosynthesis slices clearly show airways and pulmonary vascular structures in the anthropomorphic lung phantom. The results show the CNT source array is capable of generating sufficient dose for chest

tomosynthesis imaging. The conclusion of this chapter is that an s-DCT using a distributed CNT x-ray source array is feasible.

Section 5.2: Purpose

Currently, digital tomosynthesis (DTS) has been in clinical use for breast, chest, sinonasal, abdominal, and musculoskeletal imaging.[6, 1, 7, 62, 4] Clinical studies have demonstrated that digital chest tomosynthesis (DCT) improves the ability to detect small lung nodules in comparison to CXR, and at a much lower dose than chest CT.[1, 8, 10, 3, 9, 13] Other than lung nodules, DCT also shows improved diagnostic ability in detecting other lung pathology, such as bronchiolitis, pulmonary consolidation, pulmonary emphysema, and cystic fibrosis when compared to CXR.[31, 12, 11]

DCT systems in use today use a single-beam x-ray source that moves to collect a set of low dose projection images acquired from multiple angles. The relatively long scanning time, approximately 10 s, leads to image blur due to patient motion.[13] In systems with a moving x-ray source, there is a tradeoff between the scanning time and tube moving speed. In general, the shorter the scanning time, the faster the tube needs to be moved. This can be mechanically challenging, and may lead to blurring due to x-ray source focal spot motion during the detector integration time.

We have recently developed a carbon nanotube (CNT) based distributed field emission x-ray source array technology.[15, 63] The technology utilizes an array of individually controllable CNT emitters as the 'cold cathodes'. By electronically switching the individual CNT cathodes on and off, a scanning x-ray beam is generated by different focal spots on the x-ray anode without any mechanical motion. The CNT x-ray source array is particularly attractive for tomographic imaging because the projection views are acquired from different angles without mechanical motion. This technology enables stationary tomography with fast scanning speeds and high image resolution by eliminating imaging blur due to source and patient motions. It also opens up the feasibility of designing tomography scanners with novel

geometries, as stationary imaging with multiple sources removes the issues associated with managing the momentum of heavy x-ray sources moving in multidimensional paths.

The purpose of this chapter is to investigate the feasibility of s-DCT using a CNT x-ray source array, and the system requirements for the source array for s-DCT.

Section 5.3: Materials and Methods

A bench-top system was set up using a linear x-ray source array containing 75 focal spots and a flat panel detector, as shown in Figure 5.1. The linear source was characterized. The x-ray output and beam quality were measured. Focal spot sizes of multiple spots were measured using a pinhole phantom. Projection images of a cross wire phantom were acquired and reconstructed to measure the system modulation transfer function (MTF) and the artifact spread function (ASF) as quantitative measurements of the system in-plane resolution and in-depth resolution, respectively.

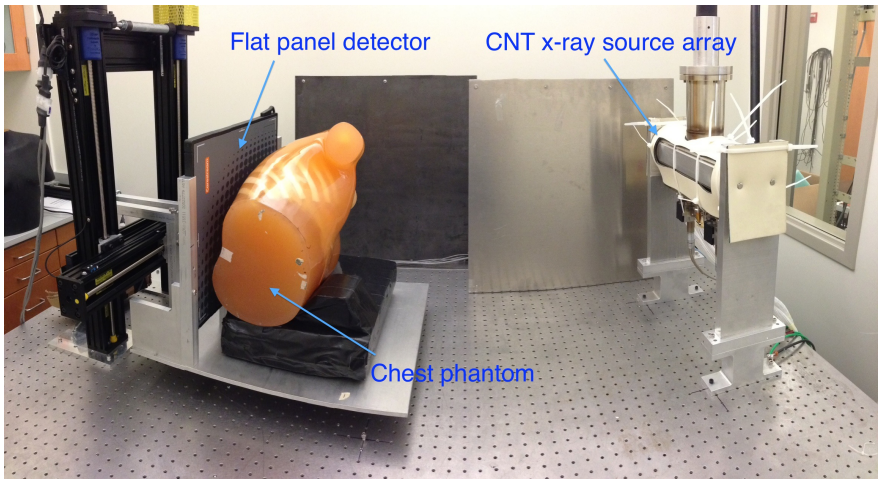

Figure 5.1: Bench-top stationary chest tomosynthesis system. The linear CNT x-ray source array consists of 75 x-ray generating focal spots. The detector and phantom, mounted on the same stage, can be translated to simulate different imaging geometries.

5.3.1: Distributed CNT X-ray Source Array

The CNT x-ray source array (Model 2008-08-L75-002, XinRay System Inc., Research Triangle Park, NC) contains 75 linearly distributed x-ray focal spots with a 4 mm pitch, and an end-to-end spacing of 296 mm. Each x-ray source consists of a CNT cathode, gate and focusing electrodes, and an elongated tungsten anode shared with other sources. The cathode is grounded, while the gate electrode is applied a positive voltage to extract electrons from the cathode via the field emission effect. The field emission current is controlled by the electric field applied between the gate electrode and cathode. The maximum output current, as in conventional x-ray tubes, is limited by the thermal management of the anode, and is influenced by interplay of many factors including the focal spot size, the anode voltage, the pulse width, and the duty cycle. The x-ray tube current, defined as the current that reaches the anode, is less than the cathode emission current due to leakage primarily to the gate electrode. The electron transmission rate, defined as the ratio of tube current to the emitted cathode current, as well as the gate voltage required for each cathode corresponding to a certain current, are used to characterize the CNT x-ray source. The tungsten anode has a 12° tilting angle relative to the x-ray window. A 2 mm aluminum window serves both as the vacuum barrier and as the inherent filter.

The CNT x-ray sources' stability was measured. The source stability is quantified as the cathode-gate voltage change for a fixed anode current over time. A source stability test was performed over a four-month period, during which the x-ray source was used multiple times a day. The tube current, cathode-gate voltage (V_{gc}), tube output in mAs, pulse width, and the date were recorded and logged into a database.

The focal spot size of each individual x-ray source in the array was measured using the pin-hole method described by the European standard EN12543-2. The tungsten pinhole used in the measurement was 400 μm in diameter and 2 mm in thickness. The pinhole images were acquired using a CsI based flat panel detector (Carestream DRX-1C). The pinhole was placed between the source array and the detector. The ratio between detector-to-pinhole

distance and source-to-pinhole distance was roughly 3:1, as recommended in the standard, to gain enough magnification. The exact magnification factor was determined later by analyzing the projection images. The pinhole was carefully aligned to the focal spot, whose location was determined using a system geometry calibration procedure. The images were corrected by the flat field air image to get uniform back- ground, and then the intensity in the pinhole was measured, normalized, and fitted into a 2D-Gaussian distribution. The full-width-at-half maximum (FWHM) values in both parallel (x) and perpendicular (y) directions to the scanning direction were measured and used as the focal spot size.

5.3.2: System Description

The bench-top chest tomosynthesis system, as shown in Figure 5.1, consists of the CNT linear x-ray source array, a CsI based flat panel detector (Model DRX-1C) manufactured by Carestream Health Inc. (Rochester, NY) mounted on a translation stage, a phantom stage, and an electronic control unit. The detector, which was originally designed for radiographic imaging purpose, has a field of view of 35 $cm \times 43$ cm and a 139 $\mu m \times 139$ μm pixel size. The integration time can be adjusted from 260 ms to 1100 ms. The detector requires a frame by frame external trigger to acquire a sequence of images. Since the x-ray source array used in this study has a relatively short length, the detector and the phantom are mounted on a translation stage to achieve a wider range of imaging geometries. A LabVIEW program was made to automate the x-ray tube operation and image acquisition. As illustrated in the timing diagram in Figure 5.2, the computer generates a sequence of trigger signals to trigger the detector read-out, followed by the detector ready-to-exposure signal which is synced to the x-ray source switching system. The x-ray source switching system is programed to switch and fire each x-ray source based on the sequence set by the operator. The x-ray sources can be fired in any sequence, either one-by-one from one end to the other, or in a predefined pattern.

The system geometry is shown in Figure 5.3. The source-to-detector distance is 110 cm,

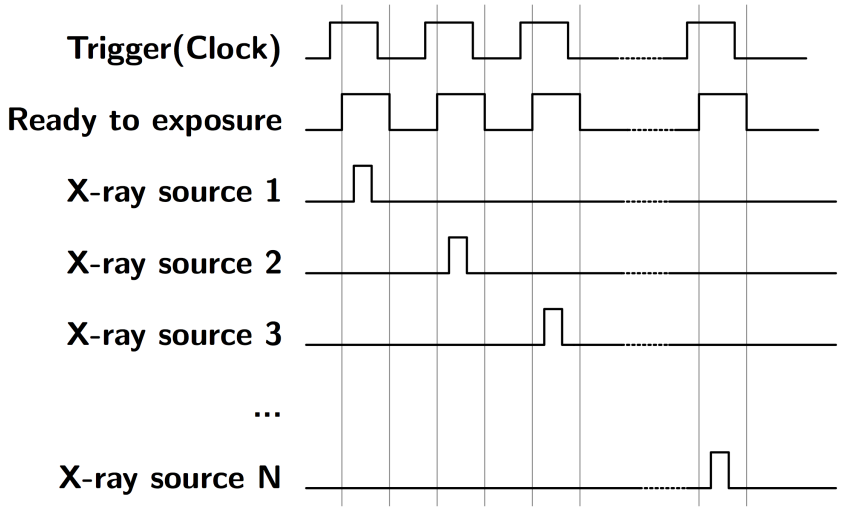

Figure 5.2: Timing diagram for s-DCT imaging. Computer generates a trigger signal to externally trigger the detector. The detector ready-to-exposure signal is synced to the x-ray source switching system, where each pulse will be used to trigger a single CNT x-ray source in the source array. The CNT sources are fired in a sequence preset by the operator.

with the source array aligned to the centerline of the detector. The 75 focal spots with 4 mm pitch, in the present x-ray source array, cover a 15.7° angular span relative to the detector center. Translation of the detector and the phantom together, relative to the source array, allows extended acquisition geometries with variable source-to-detector distances, angular coverage, and number of projection views. Due to limitations of the optical table size, the maximum effective source array length that can be emulated is 672 mm. However, the resulting 34° angular coverage relative to the detector center is comparable to current commercial systems. This effective source array has a source-to-source pitch of 4 mm and can generate up to 169 projection views. By choosing different combinations of sources, one can simulate various imaging configurations with different numbers of projections, angular span, and source-to-source pitch. For most images acquired in this study, we used every other source in this effective source array. This produced up to 85 projections with 0.4° angular steps between projections, which is comparable to commercial DCT systems.

To reconstruct the tomosynthesis dataset from the projection views, the geometric rela-

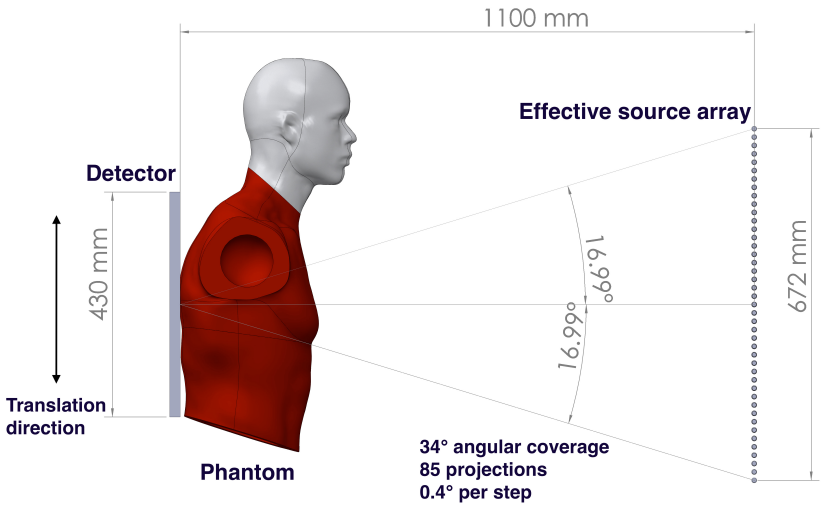

Figure 5.3: An illustration of the imaging geometry in the bench top stationary chest tomosynthesis system. The source-to-detector distance is 110 cm. By moving the detector and phantom together, parallel to the source array, we were able to emulate different imaging geometries. In the current bench-top proof-of-concept setup, the effective x-ray source array is able to cover up to a 34° angular span relative to the detector center with up to 85 projections.

tionship between the x-ray sources and the detector is required. The relative locations of each of the focal spots are determined by a geometry calibration procedure that utilizes the projection images of a phantom with metal beads positioned at different source-to-object distances to calculate the coordinates of each source relative to the center of the detector.[1]

5.3.3: X-ray Output and Beam Quality

The x-ray output and beam quality of the x-ray source array were measured. The radiation dose was measured using a solid-state dosimeter (Unfors Mult-O-Meter 470L) manufactured by Unfors Instruments AB and calibrated 3 months before measurements. (Billdal, Sweden). The dosimeter effective energy range is from 50 kVp to 150kVp. Due to the x-ray source array was not designed for medical applications originally, a 0.8 mm additional aluminum filter was added to comply with the beam quality requirement for medical imaging.

[1]The geometry calibration will be discussed in more details in Section 6.5.

Combined with the 2 mm aluminum inherent filtration, the total filtration of the source array was 2.8 mm aluminum.

The dosimeter probe was aligned to the x-ray tube and was placed 100 cm away from the focal spot without the presence of phantom or patient in front the probe to measure the incident air kerma at 100 cm in a single x-ray shot. To investigate the relationship between the incident air kerma at the detector plane and tube output (mAs), the incident air kerma was measured at 80 kVp at various mAs.

The beam quality of the source array was quantified using the first half value layer (HVL) of aluminum. The CIRS HVL filter set (Model L430) manufactured by Computerizing Imaging Reference Systems, Inc. (Norfolk, Virginia) was used as additional aluminum filtration in the measurement, in addition to the 2.8 mm aluminum total filtration of the source array. A collimator made of 6.35 mm (0.25 inch) thick lead was placed in front of the source array x-ray window, and aligned to the central source. Additional aluminum sheets were taped sequentially to the collimator. The doses after the additional aluminum filtration were measured three times for each thickness. The average dose was normalized to the dose without additional filtration, and plotted in a semi-logarithmic graph (base of 2) to determine the first HVL.

5.3.4: Image Reconstruction

In this study, a commercial reconstruction system from Real Time Tomography (RTT) (Villanova, PA) was used for tomosynthesis image reconstruction. The RTT software uses a back projection filtering method, which allows for on-the-fly reconstruction. It allows for easy implementation of different imaging configuration parameters and image processing techniques.[64]

5.3.5: The System MTF and ASF

The MTF is used as a quantitative measure of the in-plane resolution while the ASF gives a quantitative measurement of the in-depth (z-axis) resolution. In this study, the system MTF and ASF were measured using a 100 μm diameter tungsten cross-wire phantom. The MTF is calculated as the discrete Fourier transform of the line spread function (LSF) of the wire phantom. The LSF is measured using a slant angle oversampling method.[65, 66] The LSF was fitted to a Gaussian function to remove noise before doing the Fourier transform. The in-plane resolution was measured as the frequency at 10% of the MTF. MTFs in both the x and y directions were measured.

ASF can be used to evaluate the in-depth resolution of a tomosynthesis system.[67, 68] It is calculated by measuring the contrast between objects, and the background for every reconstructed slice.[68, 69] The equation used to calculate the ASF is:

$$\mathrm{ASF}(z) = \frac{|\mu_{obj}(z) - \mu_{bkg}(z)|}{\mu_{bkg}(z)} \tag{5.1}$$

where $\mu_{obj}(z)$ is the average pixel value of the object in the region of interest (ROI) for the slice located at z, and $\mu_{bkg}(z)$ is the average value of the background pixels near the ROI for the slice. In the linear imaging geometry, the out-of-plane artifacts of the wire are blurred along the scanning direction on the off-focus tomosynthesis slices, therefore the wire perpendicular to the scanning direction is used to measure the ASF of the system. The average pixel value of the perpendicular tungsten wire in the randomly chosen ROI was measured for each slice. The slices were reconstructed with 1 mm separation along the z-axis. The full width at half maximum (FWHM) of the ASF is used as a quantitative measure of the z-axis resolution.[67, 68, 70]

The relationship between the image quality and imaging geometry was studied. The system MTF and FWHM of ASF were measured at different imaging configurations with an angular coverage between 11.6° and 34°.

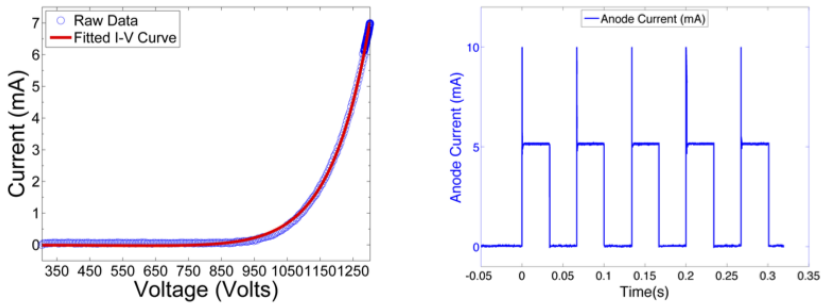

Figure 5.4: An example of CNT cathode performance in the x-ray tube. (a) The I-V curve of a CNT cathode shows the voltage needed to extract 7.5 mA of current. (b) The anode current waveforms for 5 mA current and 33 ms pulse width from 5 different CNT sources. The overshot signal at the beginning of each pulse was the step response of the switching electronics, which was not a real anode current overshoot.

5.3.6: Anthropomorphic phantom imaging

Projection images of an anthropomorphic phantom (Kyoto Kagaku Co. Ltd, Kyoto, Japan) were acquired and reconstructed into tomosynthesis slices. The phantom was positioned as shown in Figure 5.1. The scanning direction was along the axis of the spine (superior–inferior direction), as commonly used in previous studies, to reduce the limited angular artifacts of the ribs.[1, 4, 10] The projection images were acquired at 80 kVp and 0.6 mAs exposure per projection. The images were reconstructed using the RTT software with 4 mm slice spacing for image quality assessment.

Section 5.4: Results

5.4.1: CNT X-ray Source Array Characterization

All 75 CNT sources in the array were characterized. Figure 5.4 shows the field emission properties of the CNT source measured at 80 kVp. As shown in Figure 5.4(a), the emission current versus the applied cathode-gate voltage curve follows the Fowler-Nordheim equation for electron field emission.[38] Once the cathode-gate voltage exceeds the CNT field emission

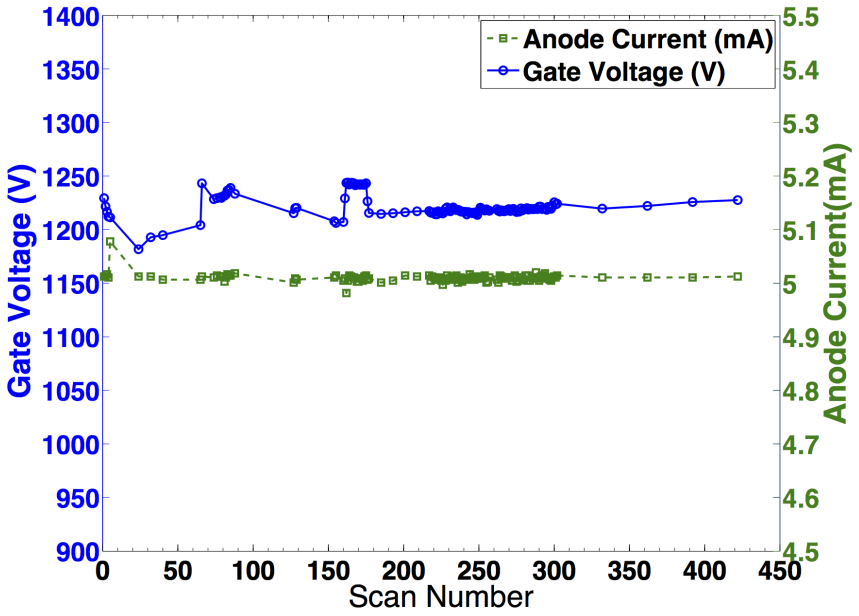

Figure 5.5: Stability measurement of a CNT source over 400 scans during a 4 month period. The tube current (green dashed curve) was kept at 5 mA, the cathode-gate voltage (blue curve) barely changes in the test. The tube current fluctuation is less than 2% over the 400 scans, and no significant degradation of cathode-gate voltage was observed.

threshold voltage, the emission current increases exponentially as the gate voltage increases. The measured transmission rates were consistent among all sources, with an average value of 70%. Figure 5.4(b) shows the anode current waveform for 5 different sources, measured using an oscilloscope, during source characterization. Each source outputs 5 mA of anode current during a 33 ms pulse width. As demonstrated in figure 5.4(b), the targeted specification of 5 mA anode current can be achieved with a programmable pulse width and good source-to-source consistency for all sources. The source stability database shows long-term stability for all the CNT x-ray sources used. The source stability for a typical cathode is plotted in Figure 5.5. The cathode-gate voltage showed little change at 5mA tube current for over 400 scans in four months. This stability is consistently observed from source to source, suggesting that the tube can be stably operated over a long time under this condition.

The source-to-source consistency for all 75 CNT x-ray sources was evaluated. The gate voltage needed to generate 5mA tube current for each source was measured and is plotted in

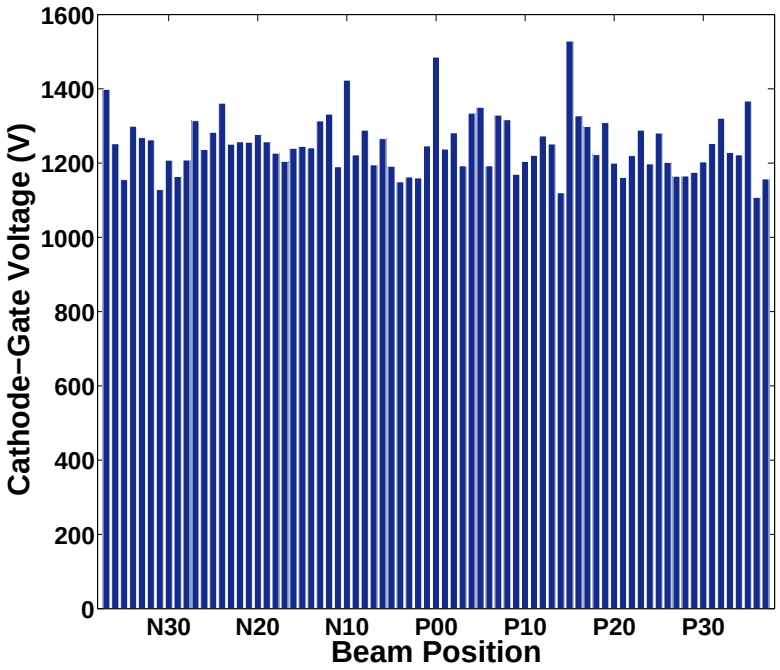

Figure 5.6: Cathode-gate voltages needed to generate 5 mA tube current from each cathode. All 75 CNT cathodes can generate the desired current, with a small variation in voltage from cathode to cathode. The average voltage needed is 1240 V. The $P00$ refers to the central beam source, while the P and N notate positive and negative locations of the source relative to the central beam, respectively.

Figure 5.6. All 75 sources were able to output the desired current. The difference between the highest and lowest cathode-gate voltage for 5 mA tube current is approximately 400 V, which was readily compensated for by the control electronics. The source-to-source output consistency in one scan was also evaluated. Figure 5.7 shows the anode current from each source in a single tomosynthesis scan using 32 CNT x-ray sources. The results show that the CNT source array can output 5 mA anode current consistently from source to source, within 0.3% accuracy. For all the images acquired in this study, all sources were set to output 5 mA tube current. By changing the pulse width (in ms) of each source was on, the x-ray output (in mAs) for each projection image was easily controlled.

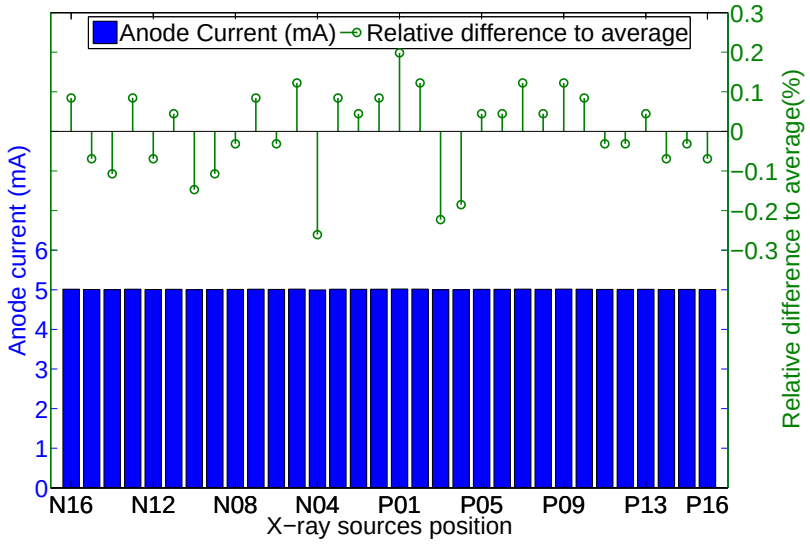

Figure 5.7: Summary of anode current in a short tomosynthesis scan using 32 sources and the relative difference to the average anode current. The CNT source array consistently output 5 mA from source to source with relative difference within 0.3%.

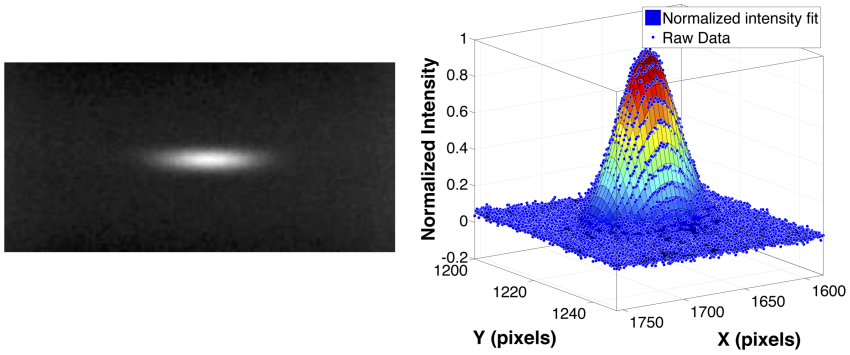

(a) (b)

Figure 5.8: Focal spot measurement using a pinhole. (a) shows the a typical pinhole image acquired at 80 kVp and 5 mA. The pinhole was $400\mu m$ in diameter and 2 mm in thickness. (b) shows the normalized intensity and the 2D Gaussian fit of the focal spot distribution.

5.4.2: Focal Spot Size

The source array used in the study was designed to have an anisotropic focal spot shape, as it was originally designed for non-medical applications. Figure 5.8(a) shows the pinhole image from a source. The magnification factor of the pinhole was calculated based on the

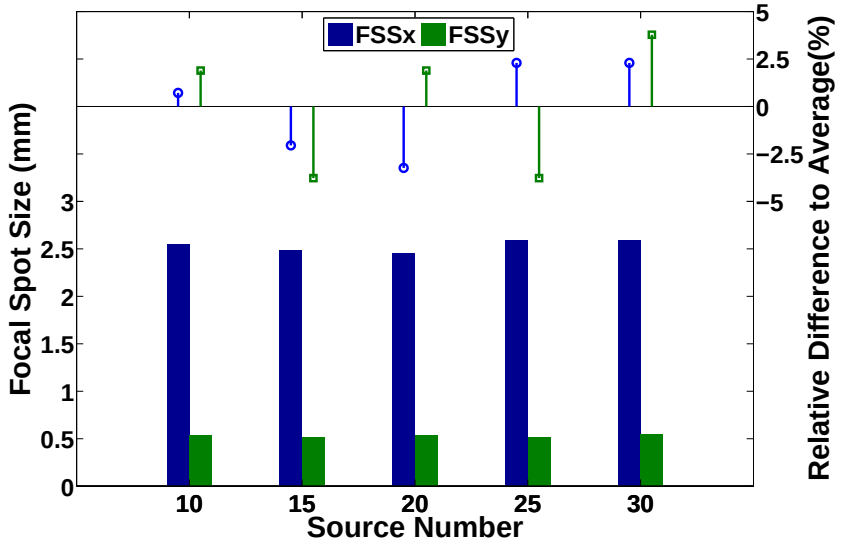

Figure 5.9: Summary of the focal spot size measurement of 5 sources in the source array. The average focal spot size was measured to be 2.5 $mm \times 0.5$ mm. The results show a good source-to-source consistency, as the relative difference is less than 4%.

magnification in size of the pinhole assembly. The intensity profile of the focal spot was measured, normalized, and fitted into a 2D Gaussian distribution, as shown in Figure 5.8(b). The intensity was closely matched to a 2D Gaussian distribution, with a coefficient of determination (R^2) of 0.9923, which agrees with the simulation results using electrical optics simulation model from our lab.[50] The FWHM of the intensity profile was used as the focal spot size. Figure 5.9 shows a summary of the measured focal spot size of 5 sources in the source array and the relative difference to the average value. The FSS_x refers to the focal spot size along the scanning direction (x-direction), while the FSS_y is the focal spot size perpendicular to the scanning direction (y-direction). The measurement results show the focal spot size is consistent from source to source within 4% relative error, with an average FWHM of 2.5 $mm \times 0.5$ mm, which agrees with the designed value for this particular source array.

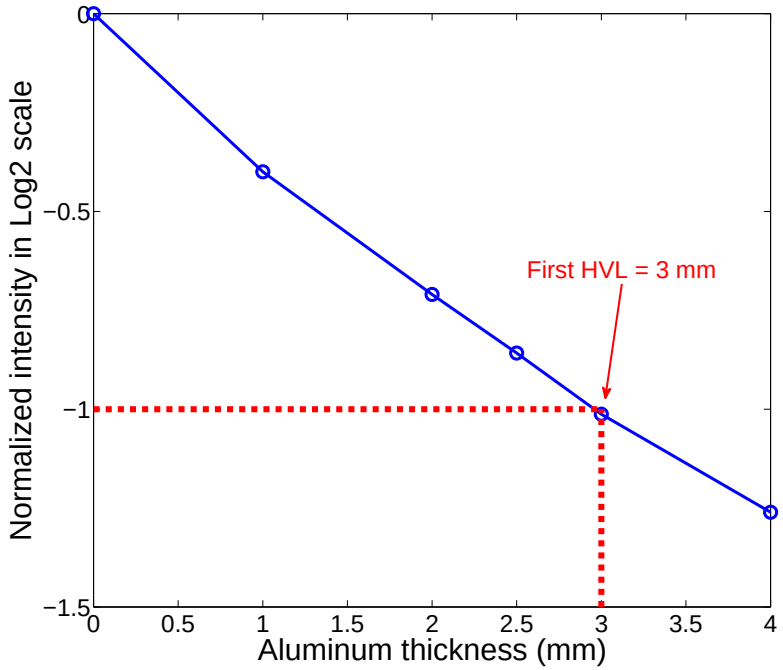

Figure 5.10: Normalized intensity in log 2 scale versus the thickness of additional aluminum filtration. The first HVL was determined by finding the thickness of aluminum to halve the dose. The first HVL of this source array was measured to be 3 mm at 80 kVp.

5.4.3: Beam Quality

The first HVL of the beam was measured to evaluate the beam quality. The first HVL was determined to be 3 mm at 80 kVp for this source array with 0.8 mm aluminum additional filtration (Figure 5.10), which complies with the regulatory minimum of 2.9 mm aluminum at 80 kVp (Table 2.1).

5.4.4: Radiation Dose

The incident air kerma at 100 cm from the focal spot was measured using the dosimeter at different tube mAs at 80 kVp. The tube output varied from 0.1 mAs to 0.5 mAs. For each mAs setting, three measurements were made. Figure 5.11 plots the relationship between the incident air kerma and the mAs at 100 cm from the central source of the source array at 80

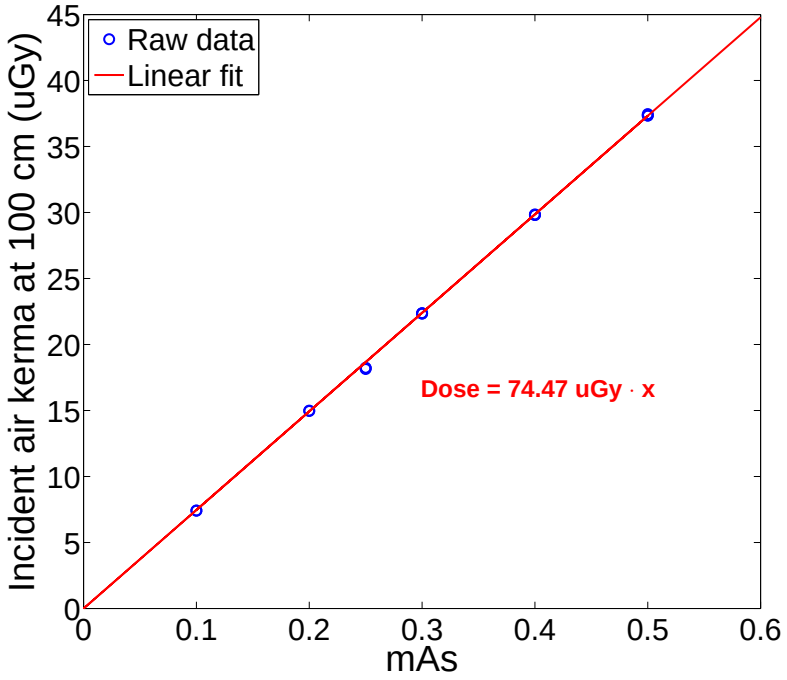

Figure 5.11: Experimentally measured relation between the incident air kerma at 100 cm from focal spot and x-ray tube output (mAs). The air kerma is linear to the anode output. The incident air kerma per mAs at 100 cm was measured as 74.47 $\mu GymAs^{-1}$.

kVp. The measurements show a linear increase with the anode output mAs, as expected. The air kerma reading per mAs at 100 cm was measured to be 74.47 $\mu GymAs^{-1}$.

5.4.5: System MTF and ASF

Projection images of the cross wire phantom were acquired at 80 kVp and 0.6 mAs per projection. The images were reconstructed using the RTT software into a tomosynthesis dataset with a 1 mm distance between slices. Figure 5.12(a) shows a reconstructed slice, where the crossed wires were focused. The MTF and ASF were studied for three imaging configurations with angular coverages, relative to the center of the detector, of 11.6°, 23° and 34°. For each imaging geometry, 29 projection images were used in reconstruction, with 0.4°, 0.8° and 1.2° angular spacing between each projection, respectively. Three randomly chosen regions across the perpendicular wire, as illustrated in the region outlined by a red

box, were used as ROIs to measure the ASF. The average pixel value of the wire in the ROI and the background were measured for each slice and averaged to calculate the ASF. Figure 5.12(b) shows the LSF of the horizontal tungsten wire and the Gaussian-fitted LSF for the 34° imaging geometry. The MTF curves for both horizontal (x-direction) and vertical (y-direction) directions with the same imaging geometry are plotted in Figure 5.12(c). The 10% cutoff of the MTF yields a spatial frequency of 1.5 cycles/mm and 3.2 cycles/mm for the x and y directions respectively. Figure 5.12(d) shows the ASF and the Gaussian-fitted ASF of the system as a function of depth (z-direction) for the 34° dataset. The in-depth (z-direction) resolution of the system, as mea- sured by the FWHM of the ASF, was 5.2 mm.

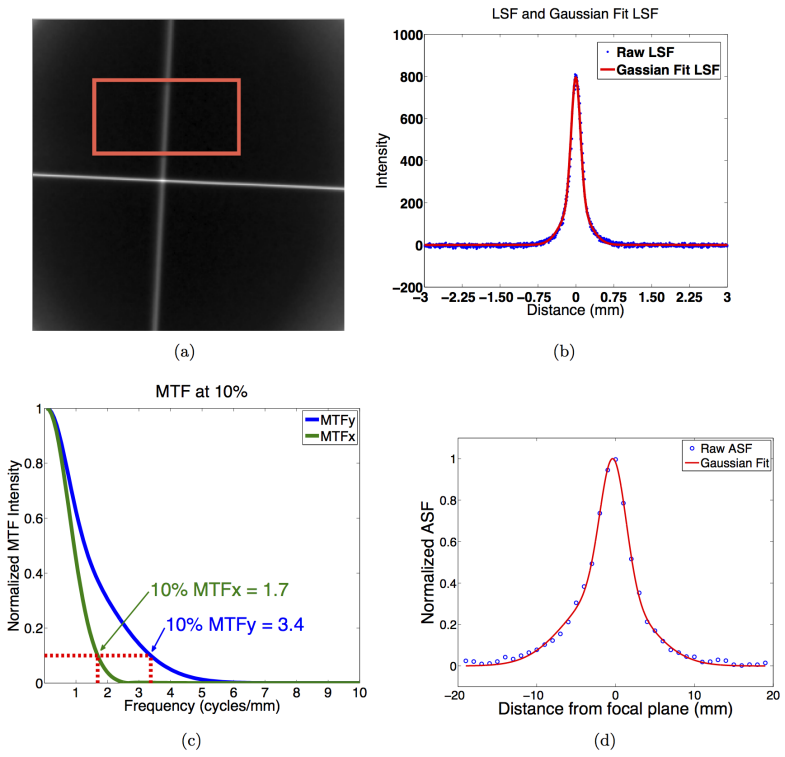

Figure 5.12: (a) A reconstructed cross wire phantom in the plane of focus with an angular coverage of 34°. The region outlined by the red box illustrates one randomly selected ROI used to calculate the ASF. (b) The LSF of the horizontal tungsten wire and the Gaussian-fitted LSF from the 34° angular coverage dataset. (c) The MTFs of the system in both x (1.5 cycles/mm) and y (3.2 cycles/mm) directions for the 34° dataset. (d) The ASF of the system measured in the 34° dataset. The measured FWHM of the ASF indicates a 5.2 mm z-axis resolution.

Table 5.1: The experimentally measured MTF and ASF of the bench-top chest tomosynthesis system for three different angular spans. MTF_x refers to direction parallel to the scanning direction, and MTF_y refers to the perpendicular direction.

Angular Span	MTF_x(cycles/mm)	MTF_y(cycles/mm)	FWHM of ASF (mm)
11.6°	1.7	3.4	9.5
23°	1.6	3.2	5.8
34°	1.5	3.2	5.2

Table 5.1 lists the results of system MTF and ASF calculations for all three imaging configurations. The asymmetric MTF in the x and y directions is due to the anisotropic focal spot size in this particular CNT x-ray tube. The smaller focal spot size in y-direction results in a better MTF than in the x-direction. As shown in the table, the MTF in both the x and y directions remains essentially the same as the angular coverage increases from 11.6° to 34°, while the ASF improves greatly as the angular coverage increases.

5.4.6: Phantom Imaging

Projection images of the anthropomorphic chest phantom were acquired and reconstructed using RTT for image quality assessments. Tomosynthesis images with the same imaging dose but different angular spans were reconstructed and compared. Three datasets, each acquired using 29 projections at 110 cm SID and 80 kVp and 0.6 mAs per projection, were captured with angular spans of 11.6°, 23° and 34°. For each projection, 0.6 mAs results in approximately 62.3 μGy incident air kerma per projection view at the patient entrance plane, which is 25 cm in front of the detector. The dose per projection is more than sufficient for the typical dose of projection view reported in clinical DCT systems.[8, 3] Three tomosynthesis slices from these datasets, focused at the same plane, are shown in Figure 5.13(a)–(c), respectively. Tomosynthesis slices from all three configurations at another depth are shown in Figure 5.13(d)–(f) as well. All reconstructed images clearly show the airways and detailed pulmonary vascular structures in the physical phantom. As the angular coverage increases,

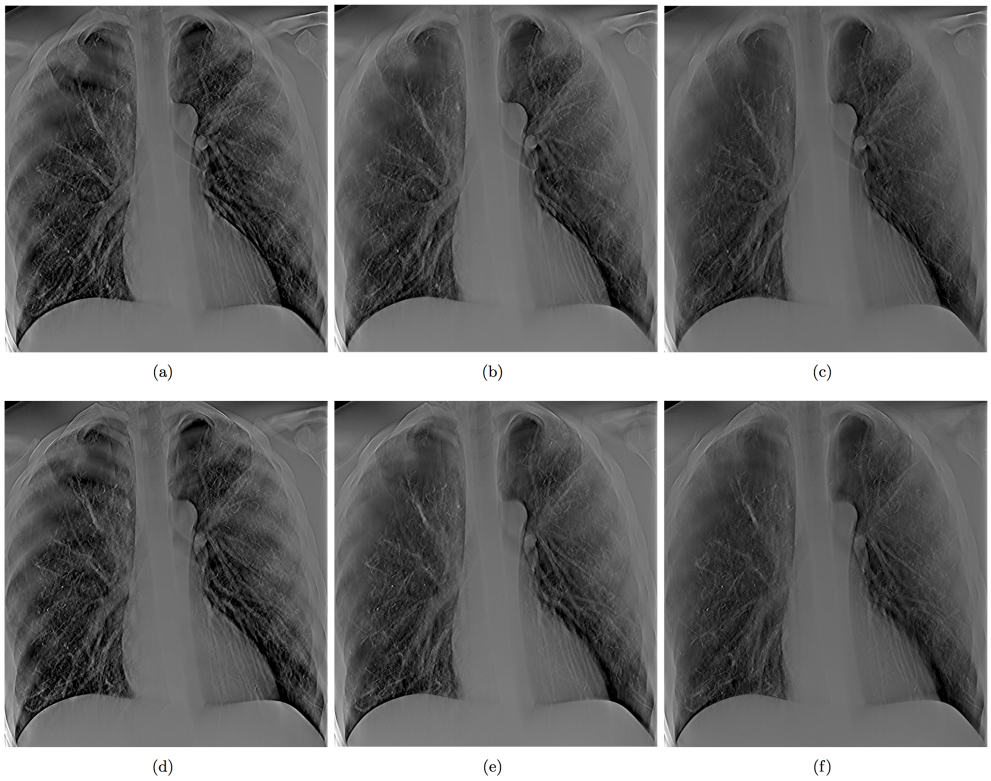

Figure 5.13: (a) and (d) show two slices at different depth (separate by 2.4 cm) reconstructed from 29 projection images acquired over 11.6°, (b) and (e), and (c) and (f) show the same slices reconstructed with same number of projection images but with 23° and 34° angular coverage, respectively. All three sets of images were acquired at the same total dose. It can be seen that the wider the angular coverage the lesser is the out of plan tomo artifact (such as those from the rib cage), due to improved in-depth resolution.

the artifacts from out-of-focus objects are reduced. At 11.6° angular span, ribs out of the focal plane can be seen in the slice, while at 23° and 34°, the visibility of these out-of-focus ribs is reduced. This is due to the improved in-depth resolution from increased angular span, as shown in the ASF measurement above. However, as the angular coverage increases, the angular step between projection images increases as well, resulting in ripple artifacts due to under sampling of the angular range.[71, 5] These ripple artifacts are caused by the high contrast objects (i.e. ribs) far outside the imaging plane that are not sufficiently blurred.

Two sets of tomosynthesis images were compared. Both covered 34° angular span and were acquired with same total mAs, but with different numbers of projection images, were

compared. Figure 5.14(a) shows a slice reconstructed with 29 projections covering 34°, acquired at 80 kVp and 0.6 mAs, while figure 5.14(c) shows the same slice reconstructed with 85 projections over the same angular span. Increasing the number of projections results in reduced ripple artifacts as shown magnified in figures 5.14 (b) and (d), corresponding to the region boxed in red in figures 5.14(a) and (c), respectively. At the same angular coverage, more projection views decreases the angular step between projection views and reduces the under sampling of the sharp edges.

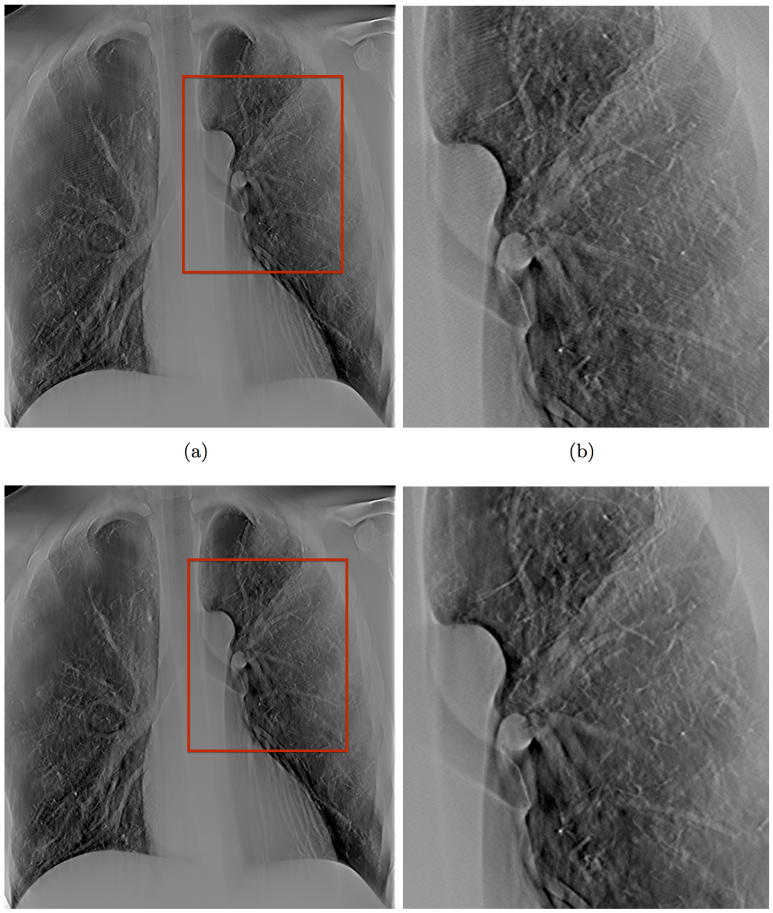

Figure 5.14: (a) shows a slice reconstructed with 29 projections over 34° angular span, while (c) shows the same slice reconstructed with 85 projections over the same angular span. As shown in the zoomed in region, outlined with a red box in (b) and (d), it can be seen that the ripple artifacts decreased when the number of projection images is increased. The two sets of images were acquired at the same total dose.

Section 5.5: Discussions

In this chapter, a bench-top DCT system was constructed and used to investigate the feasibility of a stationary DCT using a spatially distributed CNT x-ray source array. One of the key questions investigated was whether the CNT x-ray source array is capable of generating sufficient x-ray output for chest tomosynthesis. Projection images in current commercial DCT systems are typically acquired at 120 kVp and 180 cm SID. The tube output (mAs) is usually derived using automatic exposure control (AEC) from a scout view image.[3, 9, 72, 27] For instance, the GE VolumRAD DCT system multiplies the mAs of the scout view by 10, and uniformly distribute the derived mAs into 60 projection views.[3] The scout view uses the standard PA CXR technique. Sabol calculated the mean technique of 1.9 mAs and 0.1 mGy incident air kerma for the standard PA CXR used in clinic from 294 adult cases.[3] Based on the method to derive tomosynthesis radiographic technique from the scout view, the mean tomosynthesis technique is 0.32 mAs and 16.7 μGy incident air kerma per projection, where the SID is 180 cm and the incident air kerma was measured 25 cm in front of the detector.[3] The incident air kerma is a more reliable reference since the tube output in mAs used also depends on the kVp, tube filtration, and SID. For the CNT source array used in this study, the incident air kerma per mAs at 100 cm was measured as 74.47 $\mu Gy/mAs$ at 80 kVp. The phantom images in this study were acquired at 0.6 mAs per projection. Using this technique, assuming an average-sized patient with a chest thickness of 25 cm and extending the s-DCT SID to 180 cm as current systems, the incident air kerma is scaled to 18.6 μGy at the patient entrance plane (155 cm from source), which is higher than the mean incident air kerma per projection in the tomosynthesis technique. With larger patient, the mAs per projection needs to be increased accordingly. Therefore, the x-ray output from CNT source array in this s-DCT system is comparable to current clinical tomosynthesis systems. All 75 CNT sources in the tube can be operated stably at this condition with reasonable source-to-source consistency in the cathode-gate voltage and focal spot size.

The x-ray source array was operated at 80 kVp in this study because that was the maxi- mum design specification for this specific tube, which is why this study was done at a lower energy than the energy used in commercial chest tomosynthesis systems (typically 120 kVp). However, CNT x-ray source arrays using the same technology with energies up to 160 kVp, with even higher power outputs, are now available for other imaging applications from XinRay Systems.[59] Future plans include designing and building a dedicated source array for chest tomosynthesis for higher x-ray energies, the feasibility of which has been demonstrated through the 160 kVp source array developed at XinRay Systems.

This particular model of CNT source array has an elongated focal spot size of $2.5mm \times 0.5mm$ FWHM by design, as opposed to the isotropic shape found in most commercial DR systems (0.6 mm –1.2 mm nominal size).[1, 29, 28] The anisotropic focal spot leads to asymmetric system MTF values in this system. The shape of the focal spot is determined by the geometry of the CNT cathode and the focusing electron optics design. Smaller isotropic focal spots can be achieved using a different electron optics, as demonstrated in the CNT source array designed for breast tomosynthesis.[47] There is a tradeoff between the focal spot size and the maximum tube power, which needs to be considered when designing a dedicated source array for chest tomosynthesis. A detailed anode heat simulation is needed to determine the optimum focal spot size based on the anode heat capability.[2][51] For instance, the tungsten anode can safely withstand 1.1 kW power in a $0.6\ mm \times 0.6\ mm$ effective focal spot size during a 250 ms pulse according to simulation.[47, 51] If the tube operates at 120 kVp, the source array can be safely operated at 9 mA tube current. Given the performance of this tube, a slight reduction of the focal spot area is not expected to affect the ability to generate the x-ray output needed for chest tomosynthesis.

Due to the short length of the source array used in this feasibility study, the phantom and the detector were translated to mimic different imaging configurations. A longer x-ray source array covering the entire angular range can be manufactured with this technology.

[2]Anode heat load analysis and simulation will be covered in detail in Section 6.4

Preliminary results show that as the angular range of the image acquisition increases, the system in-plane resolution (system MTF) remains the same, while the in-depth resolution (FWHM of the ASF) improves greatly. These findings agree with previous studies on imaging parameters of tomosynthesis, using both stationary source array and conventional moving source commercial systems.[71, 5, 70] The system MTF, corresponding to the direction with shorter focal spot size, resulted an in-plane resolution up to 3.4 cycles/mm at 10% MTF, which is comparable to the 3.5 cycles/mm at 10% MTF in GE VolumeRAD system and 3 cycles/mm at 10% MTF in Shimadzu SONIALVISION tomosynthesis systems.[30, 29] Moreover, the flexibility in the spatial configuration of the individual CNT sources allows new tomosynthesis imaging geometries, beyond the linear scanning mode, which are mechanically challenging for conventional systems. These novel imaging geometries may improve image in-depth resolution, and reduce the image artifacts. A systematic investigation and evaluation of the effects of imaging acquisition geometry and parameters on image quality in the s-DCT system will be discussed in Chapter 7.

In this study, an anti-scatter grid was not used as is normally done in clinical settings, because the main purposes were to investigate the feasibility of s-DCT and system requirements for CNT source arrays. Scatter reduction is an important issue in chest imaging. For the s-DCT system using linear source array, conventional focusing anti-scatter grid with matching focal length can be used to reduce the scatter signal in the images. Besides the anti-scatter grid, a novel method using primary beam sampling apparatus (PSA) has been proved to be effective.[73] Initial results of using PSA for scatter rejection of s-DCT will be covered in Chapter 9.

Section 5.6: Summary

To sum up, this feasibility study was performed using a CNT x-ray source array that was originally designed for a non-medical application. As such, the technical specifications of the source are different from the x-ray tube used in commercial chest imaging systems including

relatively low tube energy (kVp) and anisotropic focal spots. However, these differences do not impact the conclusions of this study. The s-DCT system reported in this paper is not the final system that would be for clinical use. One of the purposes of this study is to find the system requirements for stationary chest tomosynthesis. Based on the results obtained so far, a dedicated source array for chest tomosynthesis with improved design and system performance is under development. The source array will be designed with longer tube length to achieve optimized imaging configurations, higher operating kVp, isotropic and smaller focal spots, and higher tube current output that allows for fast image acquisition.

CHAPTER 6: Characterization of s-DCT and Related Physics Problems

Section 6.1: Overview

Chapter 5 discussed the feasibility of s-DCT using CNT x-ray source array. A bench-top proof-of-concept system was constructed using an existing source array. However, as discussed in section 5.5, there are some problems needing further discussion. The purpose of this chapter is to provide more characterization of the source array and some discussion on related topics. Sections 6.2 and 6.3 will study the source stability and the extra-focal radiation of the source array in the current s-DCT system. Section 6.4 will discuss the anode heat management issue for CNT x-ray sources. Finally, section 6.5 will cover the geometry calibration procedures for the s-DCT system.

Section 6.2: Source Stability

6.2.1: Purpose

The stability of the CNT x-ray source is always an important indicator of the usefulness of the technology. Previous studies have characterized the CNT x-ray source stability for s-DBT system using high-current accelerated lifetime testing.[47, 74] The conclusion was that the CNT emitters show good long-term stability for the task of s-DBT imaging. In Section 5.4, the stability of the CNT source array in the s-DCT prototype system was characterized. Preliminary results have shown good stability over 400 scans in a 4-month long period.

The purpose of this section is to further evaluate the source stability of the s-DCT system.

6.2.2: Methods

Key data that characterize how stable the tube operates, such as current output per source, gate-cathode voltage per source, and beam on time, were recorded in a database over a 2-year period. During the past two years, the source array was used to carry out all studies covered in this dissertation. The source array was operated on a daily basis, from several scans to hundreds of scans per day. By thoroughly analyzing this data, the stability of the CNT x-ray source was characterized.

Stability of the x-ray pulse

The stability of the x-ray pulse refers to how stable the x-ray output was during one pulse. For x-ray sources, the x-ray output is directly related to the tube current per x-ray source. Therefore, the anode current waveform was measured and monitored to characterize the stability of the x-ray output in one pulse.

The tube current waveform was measured using a current probe (Tektronix TCP A300 AC/DC Current Probe, Tektronix Inc., Beaverton, OR). The probe senses the magnetic field generated by the passing current. By sampling the field at high frequency, the waveform of the AC current can be measured. The probe was connected to an oscilloscope (Tektronix TDS 3014C Digital Phosphor Oscilloscope, Tektronix Inc., Beaverton, OR) so that the waveform was captured and saved for analysis. However, the current waveform was not monitored each time due to equipment availability.

Long term stability of the CNT x-ray sources

The current output of the CNT cathode is primarily determined by the voltage between the gate electrode and the cathode (V_{gc}). In the long run, the CNT cathode degrades. Thus to keep the same current output, the V_{gc} needs to be adjusted accordingly. However, the degradation of the cathode varies from source to source. The Multi Pixel Electronics (MPE) switching system used in the s-DCT prototype system can automatically accommodate the

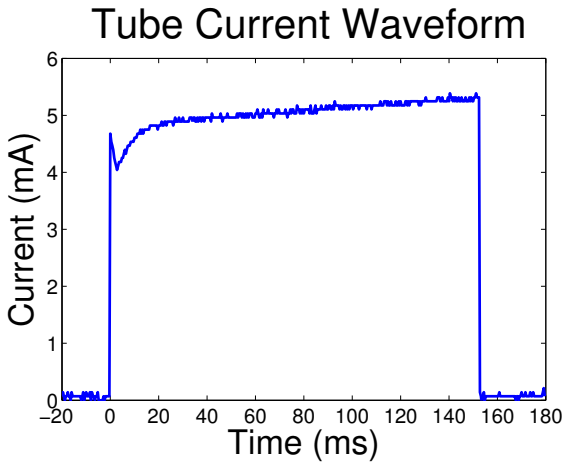

Figure 6.1: The tube current waveform for a 150 ms pulse. The current was set to output 5 mA. The waveform shows stable current output and accurate timing.

change of V_{gc} for each cathode, as long as the change is slow and gradual. The long-term stability of the source is characterized as the change in V_{gc} over time.

For each tomosynthesis scan, a customized LabVIEW program was used to log the source on time, tube current, and V_{gc} for each source automatically into a database. By comparing the change of the V_{gc} needed for outputting the same tube current, the trend and stability were measured.

6.2.3: Results: Stability of the x-ray pulse

The tube current waveforms were measured and monitored. The waveform shows stable current output during the x-ray pulse and an accurate pulse width. A representative waveform is shown in Figure 6.1. For pulses with a relatively long width, there is a slight increase in the current within the same pulse. The pattern is reproducible from pulse to pulse. This is suspected to be due to the deformation of the heated gate during the pulse. However, for the short pulses, the current remains the same during the pulse. Figure 6.2 shows the current waveforms for 5 pulses from 5 different sources. The waveforms show consistent current output from source-to-source.

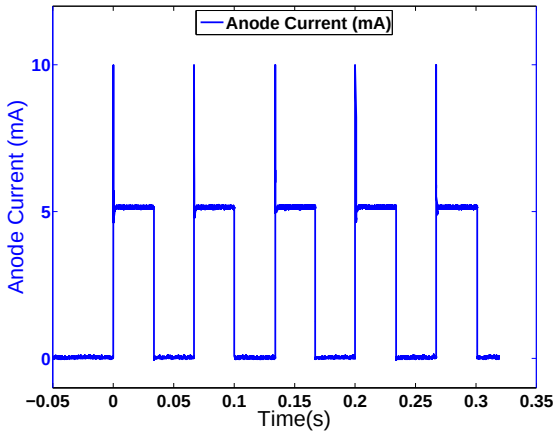

Figure 6.2: The tube current waveform for 5 mA current and 33 ms pulse width from 5 different CNT sources. The waveforms demonstrate the consistency between sources.

6.2.4: Results: Long term stability of CNT x-ray sources

The long term stability of CNT x-ray sources were measured. The gate voltage (V_{gc}) and tube current (I_a) were plotted against time for 5 representative sources across the source array (from one end to the other). They were source #11 (Figure 6.3), #20 (Figure 6.4), #24 (Figure 6.5), #29 (Figure 6.6), and #35 (Figure 6.7). In each figure, the top figure plots the V_{gc} and I_a change over the number of scans, while the bottom figure plots the changes against accumulated mAs. The data were recorded between February 21$^{\text{th}}$, 2013 and November 5$^{\text{th}}$, 2014.

All sources show good long term stability, with less than 100 V increase in V_{gc} to maintain the same tube current output. There were some sources being used more frequently than the others. For example, source 20 (Figure 6.4), which is locates in the center of the source array, was used the most, with over 9900 scans and total output of 1575 mAs. Nevertheless, after such intensive use for over 2 years, the source still output stably with less than 100 V increase in V_{gc}.

However, for each source, there was a sudden increase in V_{gc}, as pointed out by the red arrows, due to a tube arcing event that happened on July 29$^{\text{th}}$, 2014. After the arcing,

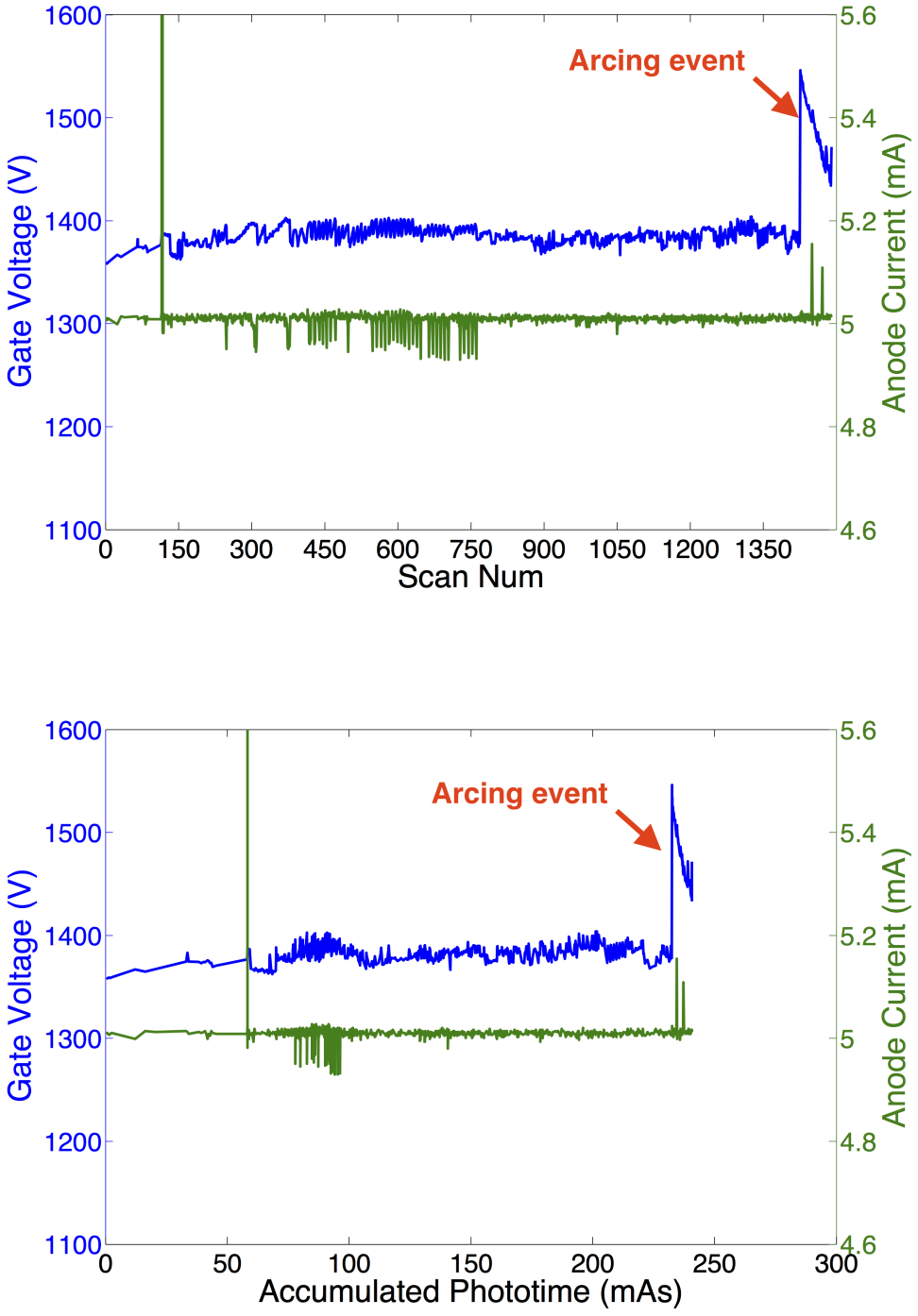

Figure 6.3: Stability measure for source #11.

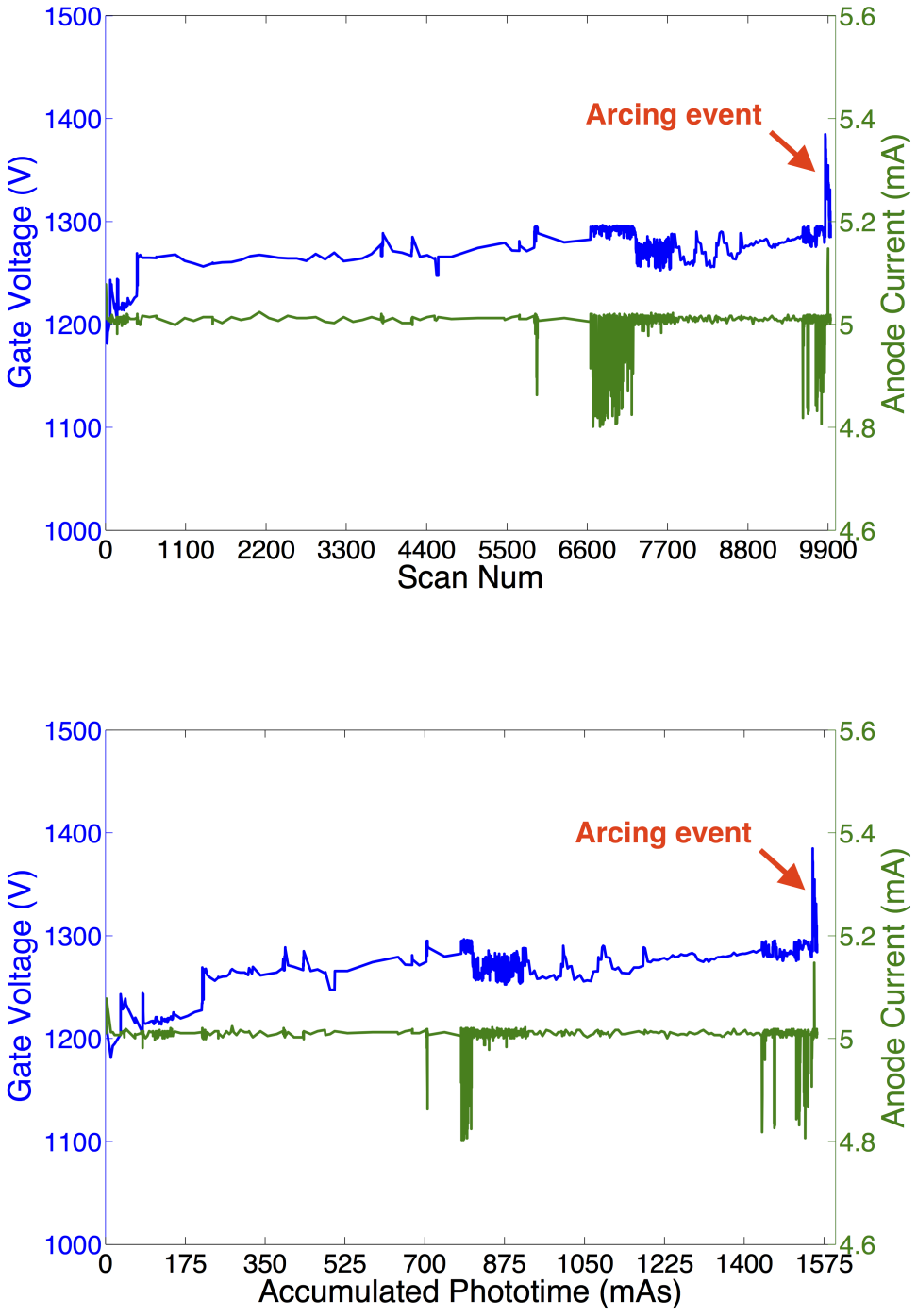

Figure 6.4: Stability measure for source #20. Source 20 is the most used source in the source array, with over 9,900 scans and accumulated output of 1,575 mAs.

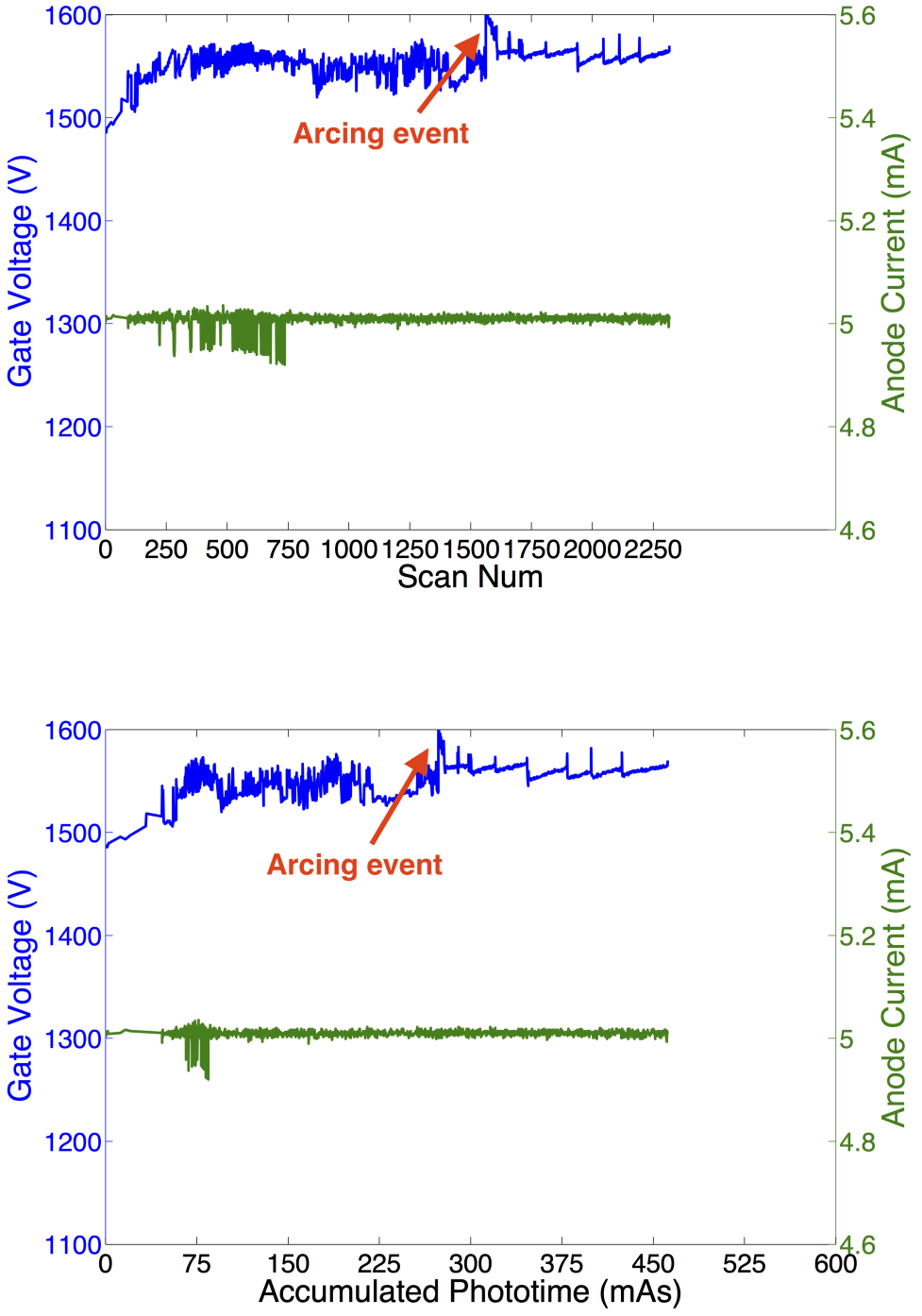

Figure 6.5: Stability measure for source #24.

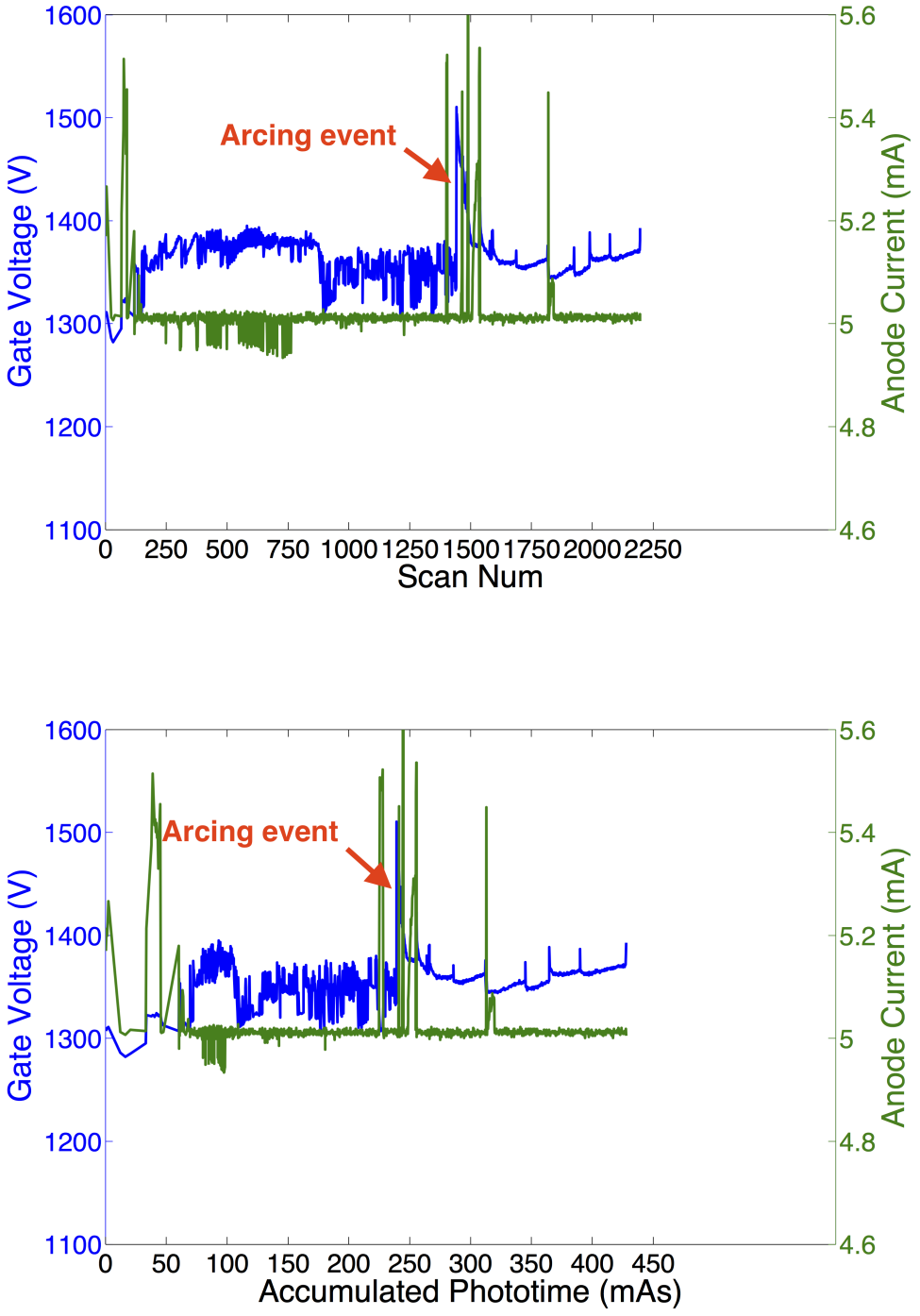

Figure 6.6: Stability measure for source #29.

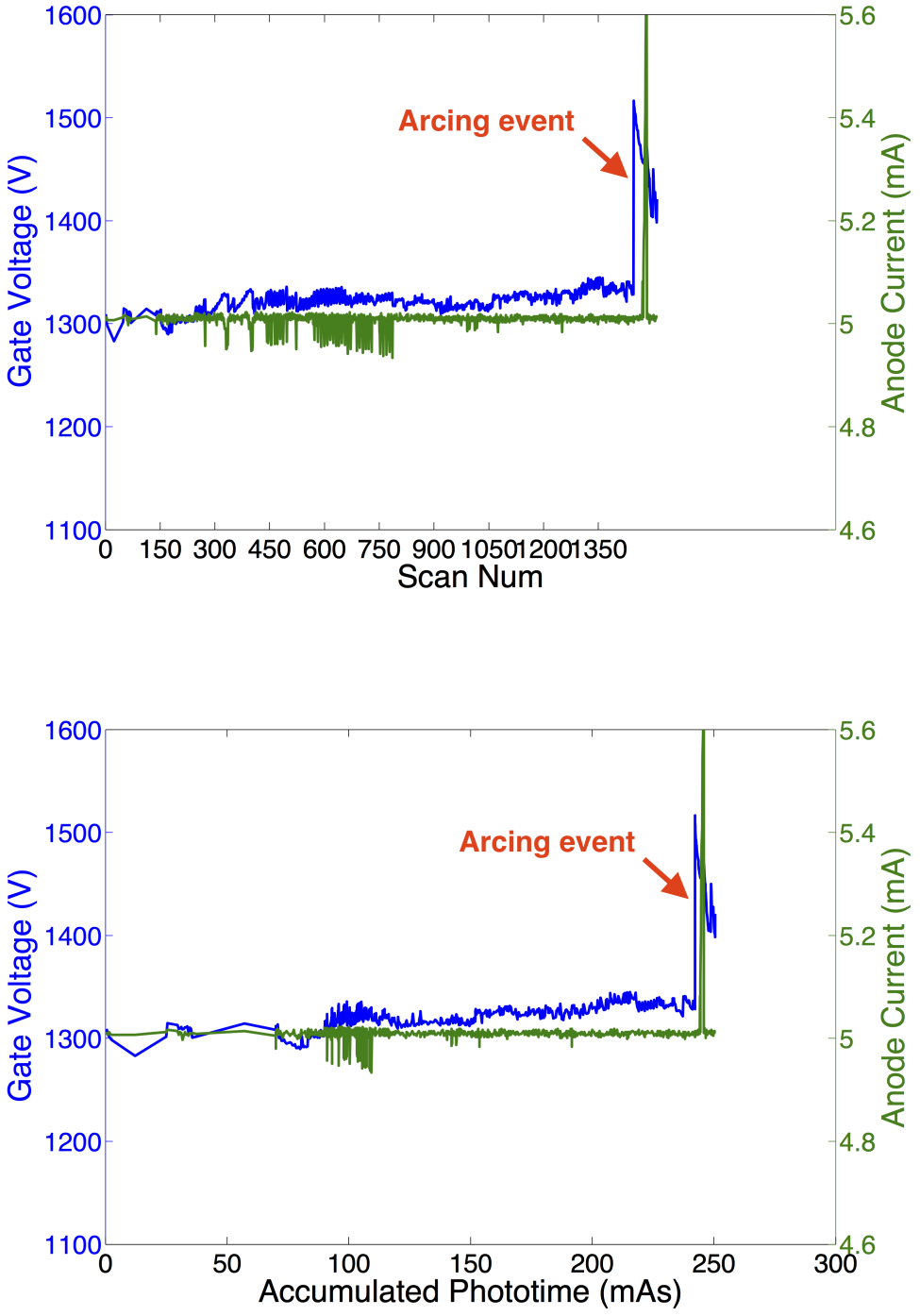

Figure 6.7: Stability measure for source #35.

nearly all sources experienced a jump in V_{gc}. Source conditioning was performed for each source. After reconditioning of the sources for several weeks, the V_{gc} recovered for all sources. However, there was still a permanent increase in V_{gc} for almost all sources. The magnitudes of the increase in V_{gc} were different from source to source, suggesting the damage to the sources was not equal.

One possible explanation for this phenomenon is briefly discussed here. Arcing damages the carbon nanotubes, decreasing the length of CNT emitters and the total number of working emitters. Thus, after the arcing, the V_{gc} needs to be much higher to extract the same amount of electrons from the damaged cathodes. Figure 6.8 shows an SEM image of a typical CNT cathode used in CNT x-ray sources. Not all CNTs are pointing outward, which is the direction favored for field emission. The conditioning procedure activated CNT emitters that were not emitting electrons previously, increases the number of emitters again, thus the V_{gc} is recovered after several conditions. However, those newly activated emitters need a stronger electric field (i.e. higher V_{gc}) to extract the same amount of current. Therefore, there was a permanent increase in V_{gc}.

Despite the arcing event, the data still show good long term stabilities for all CNT x-ray sources.

6.2.5: Discussion and Conclusion

The characterization of the source stability in this section suggests the CNT x-ray sources have good consistency in x-ray output from source to source. The long term data from 2 years of operation suggests stability and robustness of the CNT sources for the task of s-DCT.

Source 20 was used approximately 10,000 times, with a total output over 1500 mAs, without significant increase in V_{gc}. Based on this data, the clinical performance of s-DCT is estimated as follows. For example, in the coming clinical trial for an average sized patient using the s-DCT imaging protocols,[1] we determined the phototime per projection is about

[1]More details will be covered in Chapter 10.

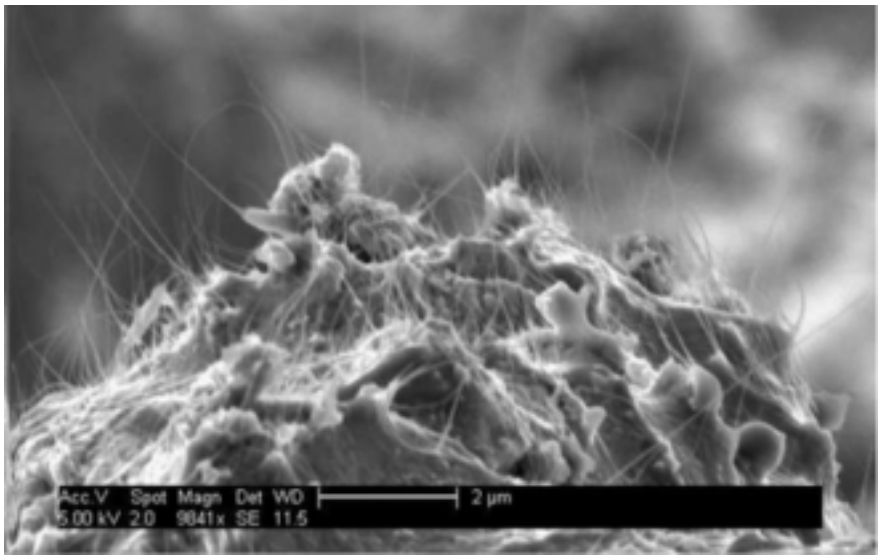

Figure 6.8: SEM image of a CNT cathode typically used in CNT x-ray sources. [74]

0.3 mAs (5 mA $\times$ 60 ms). Based on this radiographic technique, we can project that the source can reliably work for 5,000 (average sized) patients. Consider 10 patients per work day for tomosynthesis exam and 250 work days per year. This readily gives 2 years of operation, with approximately 100 V increase in V_{gc}.

Section 6.3: Extra-focal Radiation of the s-DCT

6.3.1: Purpose

The purpose of this section is to discuss the extra-focal radiation of the linear source array (Model 2008-08-L75-002, XinRay Systems) that was used in the feasibility study of stationary chest tomosynthesis (Chapter 5). This characterization is related to the radiation safety of an imaging system.

The extra-focal radiation, or off focal spot radiation, can be caused by the geometric relationship of focal spot and collimators, as illustrated in Figure 6.9. For an x-ray system, the collimator aperture assembly is designed to collimate the x-ray to the detector, if the

focal spot is an ideal point. However, the finite size of the focal spot allows part of the x-ray to shine onto the region outside the the detector. This radiation is the extra-focal radiation. It can also be caused by electrons bouncing back from anode then hitting the other part of the x-ray tube, and by secondary radiation from the primary beam. The extra-focal radiation is useless for imaging, but also gives patients extra radiation exposure. It is a convolution of many factors, such as focal spot size, focal spot intensity distribution, collimator position, collimator attenuation coefficient, etc. The IEC 60601-2-54 standard states:

> Zone of intersection of all straight lines that pass through all radiation apertures of the x-ray source assembly, with a plane normal to the reference axis at 1 m from the focal spot shall not extend more than 15 cm outside the boundary of the largest selectable X-ray field.

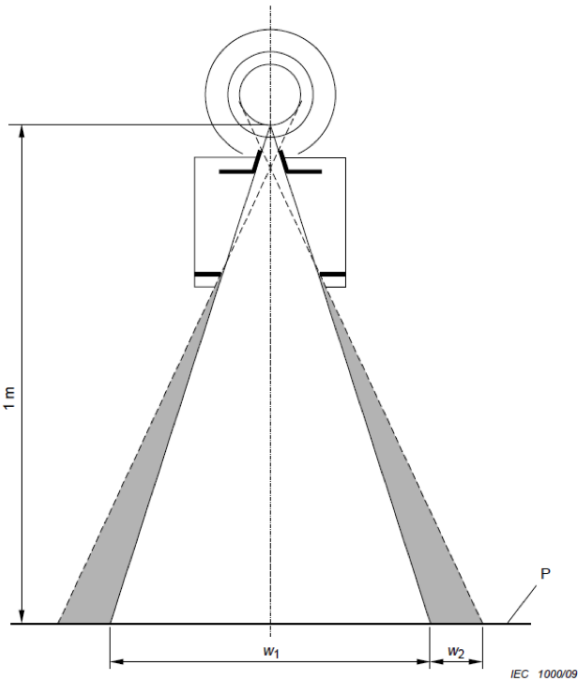

Figure 6.9: Zone of intersection of all straight lines that pass through all radiation apertures of the x-ray source assembly, with a plane normal to the reference axis at 1m from the focal spot shall not extend more than 15 cm outside the boundary of the largest selectable X-ray field.

The extra-focal radiation of the CNT source array was evaluated by simulation and experiment. The simulation was performed based on the measured size and intensity distribution of the focal spot in the source array. In the experiment, the detector reading was used as the quantitative measurement of the x-ray dose.

6.3.2: Methods

Brief system description

As described in section 5.3.1, the source array (Model 2008-08-L75-002, XinRay Systems) contains 75 linearly distributed x-ray focal spots with a 4 mm pitch. The tube was designed to have anisotropic focal spot, with the elongated side along the tube scanning direction.[2] The average measured focal spot size was 2.5 mm×0.5 mm. The focal spot size was measured using the pinhole method described in European Standard EN-12543-2. The pinhole is 400 µm in diameter and 2 mm thick. Figure 6.10 shows the projection image of a pinhole acquired at 80 kVp and 5 mA (6.10a), the intensity distribution of the pinhole image (6.10(b)), and the 2-D Gaussian fit of the normalized focal spot distribution (6.10(c)) with a coefficient of determination (R^2) of 0.9923 , where the full width at half maximum (FWHM) of the focal spot intensity in both $x-$ and $y-$ direction were used as the measured focal spot size.

The focal spot size of the tube was also measured at 80 kVp at various anode currents, as shown in Table 6.1. It was also measured at 5 mA at various anode voltages, as shown in Table 6.2. Table 6.1 shows that the focal spot size in the y-direction (FSS_y) changes little as anode current changes, while the focal spot size in the x-direction (FSS_x) improves approximately 20%. This is due to the lack of focusing structure in the source array in the x-direction. A similar trend is also observed in Table 6.2. As anode voltage increases from 50 kVp to 80 kVp, the FSS_x improves from 3.5 mm to 2.5 mm at the higher anode

[2]For consistency, we will notate the $x-$ direction as the tube scanning direction, and $y-$ direction as the direction perpendicular to the source array, as defined in Chapter 5

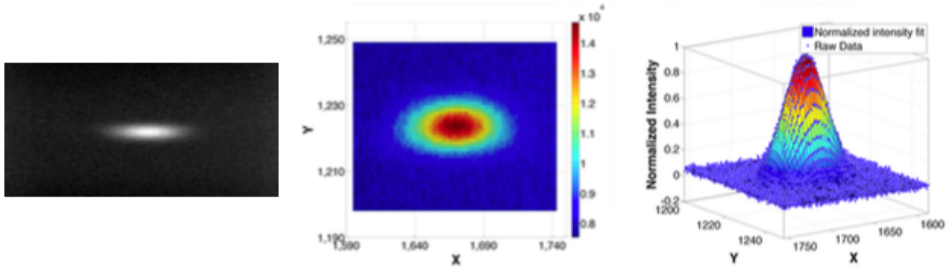

(a) (b) (c)

Figure 6.10: (a) A typical projection image of the pinhole acquired at 80 kVp and 5 mA. (b) The intensity distribution of the pin-hole image. The X and Y in the figure show the x and y coordinates in the image, in the unit of pixels. (c) The normalized intensity profile and 2D Gaussian fit. The coefficient of determination (R^2) of the fit was found to be 0.9923. The FWHM of the intensity in both $x-$ and $y-$ direction are used as focal spot size.

voltage. There is a higher electric field between gate and anode, which provides more focusing to electrons in the x-direction. This trend of changing FSS_x under different operating parameters is due to a lack of focusing structure in this particular tube. If the dedicated source array had both x- and y- direction focusing structures, we would expect consistent focal spot sizes at different operating parameters, as for FSS_y in this tube.

Table 6.1: Focal spot size measured at 80 kVp with various anode current.

Current (mA)	5	4	3	2	1
FSS_x (mm)	2.5	2.4	2.3	2.2	2.1
FSS_y (mm)	0.54	0.57	0.58	0.57	0.57

Table 6.2: Focal spot size measured at 5 mA current at various anode voltages.

Voltage (kVp)	50	60	70	80
FSS_x (mm)	3.5	3.1	2.8	2.5
FSS_y (mm)	0.57	0.57	0.57	0.54

However, since we operate the s-DCT at 80 kVp and 5 mA for most studies, the extra

focal radiation is evaluated based on focal spot intensity distribution and focal spot size measured at 80 kVp and 5 mA.

Extra-focal radiation simulation setup

Based on the experimentally measured focal spot intensity distribution, an extra-focal radiation simulation was performed. The simulation was run using MATLAB R2010a.

In the simulation, a square detector size of 400 mm was used, and the center of the detector was set up as the origin O of the coordinate system. The focal spot had a size of 2.5 mm $\times$ 0.5 mm with a normalized 2D Gaussian distribution of

$$I(x,y) = \frac{1}{2\pi\sigma_x\sigma_y} e^{-\frac{(x-\mu_x)^2}{2\sigma_x^2} - \frac{(y-\mu_y)^2}{2\sigma_y^2}} \tag{6.1}$$

where,

$$\sigma_x = \frac{1}{2\sqrt{2\ln 2}} FWHM_x = 1.06 \text{ mm} \tag{6.2}$$

$$\sigma_y = \frac{1}{2\sqrt{2\ln 2}} FWHM_y = 0.21 \text{ mm} \tag{6.3}$$

and μ_x and μ_y are the coordinates of the center of the focal spot that were being simulated. For simplicity, the simulation was performed for the central beam in the source array, and assuming the central beam was aligned to the center of the detector, i.e. $\mu_x = 0$ and $\mu_y = 0$. However, μ_x and μ_y can always be changed to any value to simulate the radiation dose profile on the detector for other non-central sources in the source array.

A source-to-imager distance (SID) of 1000 mm (1 m) was used for simulation. A collimator was placed between the focal spot and the detector to collimate the x-ray beam to the detector, as shown in the geometric setup in Figure 6.11. The source-to-collimator distance was n, and the collimator-to-detector distance was m. By changing the ratio of m and n, the extra-focal radiation on the detector plane changes accordingly. We define the magnification

factor, Mag, as

$$Mag = \frac{m}{n} \tag{6.4}$$

Qualitatively, the closer the collimator was to the source (i.e. the higher the Mag), the more extra-focal radiation was on the detector plane.

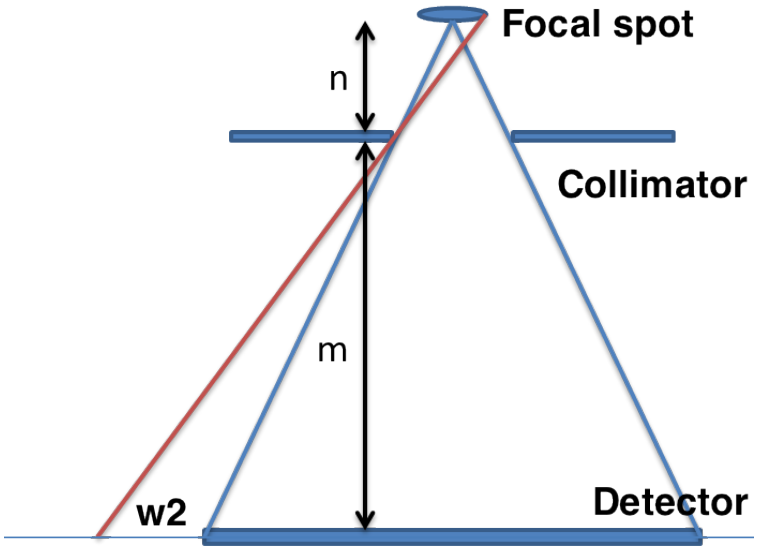

Figure 6.11: Simulation geometry. The source-to-detector distance was 1000 mm. A collimator was put between the source and detector to collimate the beam right to the detector. The source-to-collimator distance was n, while the collimator-to-detector distance was m.

Based on the fact that the focal spot of this source array is anisotropic, one would expect the extra-focal radiation would be worse on the x-direction. Therefore, for simplicity, a 1D simulation of the extra-focal radiation was perform in the x-direction to evaluate the worst scenario.

1D dose profile simulation with ideal collimator

This section will discuss the 1D extra radiation simulation with an ideal collimator. By *ideal* we assume the collimator follows Assumption 1

Assumption 1 *The collimator is designed to collimate the x-ray beam from an ideal point source, or the center of the focal spot, right to the detector. The collimator is made of*

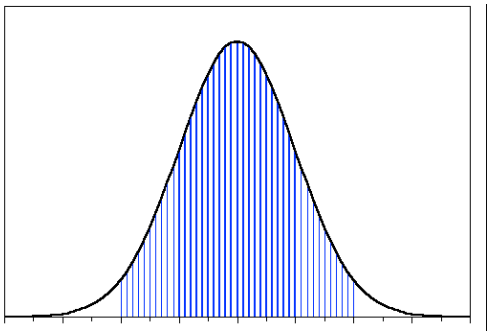

Figure 6.12: The focal spot was sampled into small bins, the intensity of each bin determined from the focal spot intensity of the Gaussian distribution.

material that can 100% *block x-ray.*

The focal spot will generate the x-ray radiation due to Bremsstrahlung radiation, we assume

Assumption 2 *For each point inside the focal spot, the radiation generated at this point is proportional to the electron intensity at this point.*

Assumption 3 *There is no interaction between x-ray photons and the collimator material, or x-ray window, i.e. no scattering photons that may contribute to the extra-focal radiation.*

The focal spot was sampled into small bins, then assign an intensity to each bin based on the focal spot Gaussian distribution, as illustrated in Figure 6.12. For the x-direction, the $FWHM_x$ was 2.5mm, a larger focal spot on the focal spot plane ($\pm$50 mm) was chosen to simulate the full focal spot distribution profile. Similarly, the detector plane was sampled into small bins to calculate the dose profile. Each bin on the detector can receive x-ray radiation from multiple bins in the focal spot plane. The intensity of x-ray in this bin was calculated by summing all radiations it received. The dose profile was calculated by combining the results of all the bins at the detector plane. The dose profile was then normalized to its maximum intensity, so that the intensity at the detector center would be 1. The detailed algorithm is shown in Algorithm 1.

Algorithm 1 Algorithm for calculating extra-radiation dose profile in 1D with ideal collimator

▷ %comment: Init focal spot array containing focal spot bins and detector array contains the detector bins. The size of the arrays are calculated by dividing the length to the bin size of focal spot and detector, respectively%
focalSpot[]= init(focal spot length,focalBinSize)
detector[]=init(detector length, detectorBinSize)
for $i = 1$ to $focalSpot.length$ **do**
▷ %comment: For each focal spot bin, determine the focal spot bin intensity%
$focalSpot[i] = intensity(focalSpot[i].x)$
▷ %comment: calculate the range of the detector bins that can receive x-ray from bin $focalSpot[i]$%
$idx = detectorBinBegin(focalSpot[i].x, Mag, detectorBinSize)$
$idxend = detectorBinEnd(focalSpot[i].x, Mag, detectorBinSize)$
for $j = idx$ to $idxend$ **do**
▷ %comment: For each detector bin j, calculate the intensity, corrected by distance, for focal spot bin i, then add the intensity%
$intensity = doseIntensity(focalSpot[i], focalSpot[i].x, detector[j].x)$
$detector[j] = detector[j] + intensity$
end for
end for
▷ % comment: Normalize the detector dose intensity profile to the maximum of the detector intensity%
$detector[] = detector[]/max(detector[])$

The dose intensity profile was then analyzed to get the width of extra-focal radiation outside the detector, w_2. The IEC 60601-2-54 standard requires the $w_2 < 15\ cm$; however, it does not state a specific requirement on how small the dose should be within w_2. In general sense, one would expect the dose as small as possible. Therefore, 0.1% (3-order magnitude) of the maximum dose was used as a criteria to determine the w_2, which is a reasonable estimation.

1D dose profile simulation with real collimator

The previous section described the algorithm to simulate the extra-focal radiation with an ideal collimator. However, this ideal collimator can not exist in reality. The material that makes the collimator can not 100% block x-rays, especially with high energy x-rays. The higher the energy of the x-ray photon, the lower the attenuation coefficient is, as illustrated

in Figure 6.13 of the attenuation coefficient of lead.

Therefore, a modified simulation algorithm, (Algorithm 2) was used to take the attenuation coefficient into consideration. The algorithm was based on Algorithm 1, but instead of calculating the beginning and end index of bins on the detector that can receive x-ray, it loops over all possible paths that connect the focal spot bins and detector bins. It then examines whether there is collimator material in the path and calculates the thickness of the material, then the intensity of the x-ray was corrected with the attenuation as

$$I' = I_0 e^{-\mu \cdot x} \tag{6.5}$$

where the μ is the x-ray attenuation coefficient, and the x is the thickness of the material the x-ray passing through.

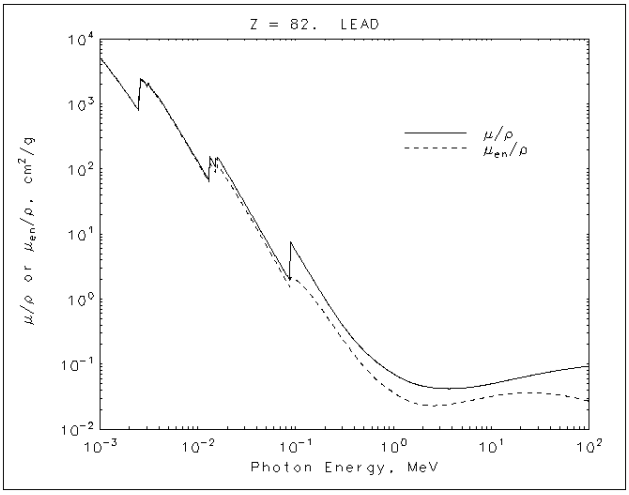

Figure 6.13: Attenuation coefficient of lead. Source: NIST database

However, since x-ray photons with different energy have different attenuation coefficients, unless we know the spectrum the of the x-ray, it would be hard to accurately calculate the attenuated x-ray intensity. Therefore, we assumed a monochromatic x-ray of 80 keV energy, so that we could simulate the worst extra focal radiation scenario. We modified the simulation model to include a lead collimator of 6.35 mm (0.25 in) in thickness and with a

opening that collimates x-ray to the detector. We assumed there was no scatter interaction between x-ray photons and the collimator. Therefore, the modified Algorithm 2 is:

Algorithm 2 Algorithm for calculating extra-radiation dose profile in 1D with ideal collimator

▷ %comment: Init focal spot array containing focal spot bins and detector array contains the detector bins. The size of the arrays are calculated by dividing the length to the bin size of focal spot and detector, respectively%
focalSpot[]= init(focal spot length,focalBinSize)
detector[]=init(detector length, detectorBinSize)
for $i = 1$ to $focalSpot.length$ **do**
  $focalSpot[i] = intensity(focalSpot[i].x)$
  for $j = 1$ to $detector.length$ **do**
    ▷ %comment: For each focal spot bin i and detector bin j, use function $checkpath(i, j)$ to calculate the thickness of lead in between the path, function will return 0 if the path does not cross collimator%
    $thickness = checkpath(i, j)$
    $intensity = doseIntensity(focalSpot[i], focalSpot[i].x, detector[j].x) * exp(-\mu * thickness)$
    $detector[j] = detector[j] + intensity$
  end for
end for
  ▷ % comment: Normalize the detector dose intensity profile to the maximum of the detector intensity%
$detector[] = detector[]/max(detector[])$

The 3-order magnitude drop criteria was still used to determine w_2.

Extra-focal radiation experimental setup

An extra-focal radiation experiment was set up to validate the simulation model and measure the actual extra-focal radiation. The experimental setup is shown in Figure 6.14. A 6.35 mm (0.25 in) lead sheet was put in front of the tube x-ray window as an collimator. A 6.35 mm (0.25 in) square hole served as the aperture to collimate the x-ray beams. The aperture was aligned to one of the sources in the source array. A detector (Varian 3030D) was used to acquire images; the detector had 300 mm × 300 mm field of view and 190 µm pixel size. The detector was placed 1060 mm away from the focal spot, and the center was roughly aligned to the center of the source array.

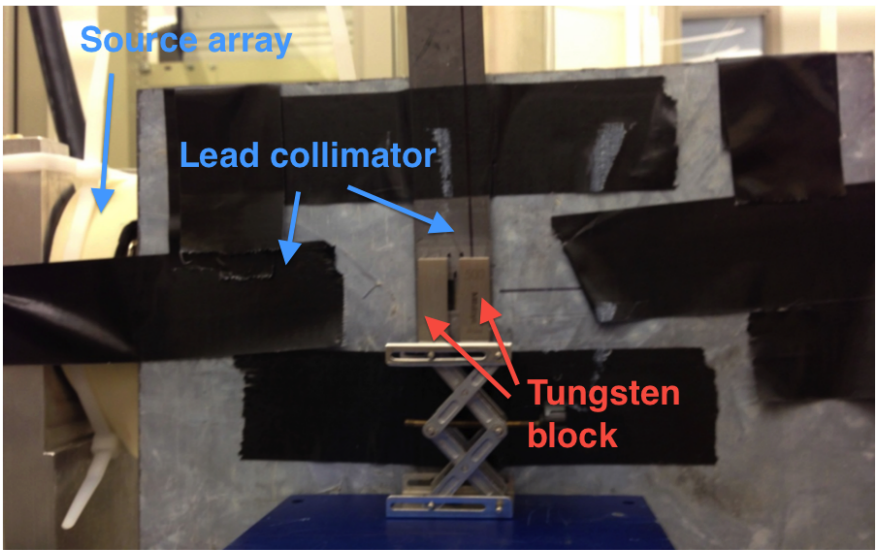

Figure 6.14: Experimental extra-focal radiation measurement setup. A lead sheet was put in front of the tube window, a square aperture was open to collimate x-ray beams. Two 12.7 mm (0.5 in) thick tungsten block were placed in front of the aperture as extra collimator along x-direction, due to the longer focal spot size in x-direction. The opening between tungsten block was 5 mm.

The detector reading of the pixels was used as an indicator of radiation dose. A line profile across the image of the collimator was used to determine how fast the dose drops off near the edges of the collimator. Because the focal spot size was larger along the x-direction, to measure the dose profile in the x-direction using such a small detector, two tungsten blocks of 12.7 mm (0.5 in) thickness were placed in front of the square aperture to narrow down the opening in the x-direction. The narrowed aperture was 5 mm.

One hundred images, together with 100 dark field images, were acquired so that the images could be averaged, reducing the effect of image noise. Each image was acquired at 80 kVp and 5 mA with a 30 ms pulse width. The images were corrected using the dark field images and averaged. Line profiles across the aperture in both $x-$ and $y-$ direction were used to measure how fast the dose drop off at the collimator edge. To study the worst scenario, the profile along the x-direction was analyzed.

6.3.3: Results

1D dose profile simulation for ideal collimator

Simulations of the dose profile along the x-direction using an ideal collimator were performed for various collimator positions, i.e. for different collimator magnification factors, Mag. Figure 6.15(a) shows the normalized dose profile on the detector plane (1000 mm away from the source). The dose was normalized to the maximum intensity (at the center of detector). The detector width was 400 mm, ranging from -200 mm to 200 mm. The collimator was placed 38.5 mm away from the source, which was reasonably close to the realistic design, resulting in a $Mag = 25$ in the simulation. As shown in the figure, the dose falls off quickly after the detector edge. The same dose profile was plotted in log scale in Figure 6.15(b). From the plot, the dose magnitude drops to the 10^{-3} order of the peak dose in 76.6 mm, which is less than the 15 cm requirement by IEC.

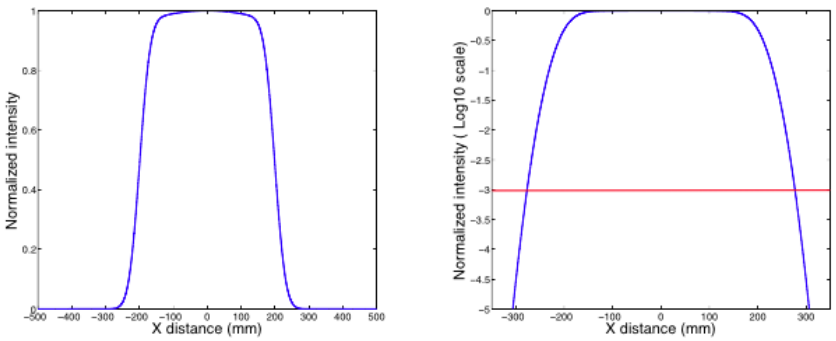

Figure 6.15: (a) Normalized dose profile on the detector plane, the detector width is 400 mm, the collimator magnification factor Mag is 25, which is close to realistic design. With higher magnification, the intensity drops more slowly off the detector edge. (b) The normalized dose intensity plotted in log scale. The plot suggests the extra-focal radiation drops to the 10^{-3} order within 76.6 mm, which is less than the required 15 cm.

Table 6.3 summarizes the w_2 for the dose to drop to the 10^{-3} order for various collimator magnification factors. The results in the tables show that the higher the collimator magnification factor, Mag, is (the closer the collimator is to the source), the slower the dose

Table 6.3: w_2 for various collimator magnification factor Mag using ideal collimator

Mag	1	5	6	7	8	9	10	15	19	20	25	30
w_2(mm)	3.1	15.5	18.5	21.4	24.6	27.6	31.0	46.0	58.9	61.3	76.6	91.9

drops to the 10^{-3} order mark (the wider the w_2). For a typical x-ray tube, the collimator is very close to the x-ray exit point. For $Mag = 30$, the source-to-collimator distance is 32.3 mm while the source-to-detector distance is 1000 mm, which is very close to a realistic x-ray tube. The dose profile is shown in Figure 6.16, the w_2 when dose drops to 10^{-3} order is 91.9 mm, which is less than the 15 cm requirement.

The simulation model predicts that the dose drops very quickly off the detector edge, which is expected. However, this model with the ideal collimator does not consider the limited attenuation effect of the collimator, which may be inaccurate when higher energy

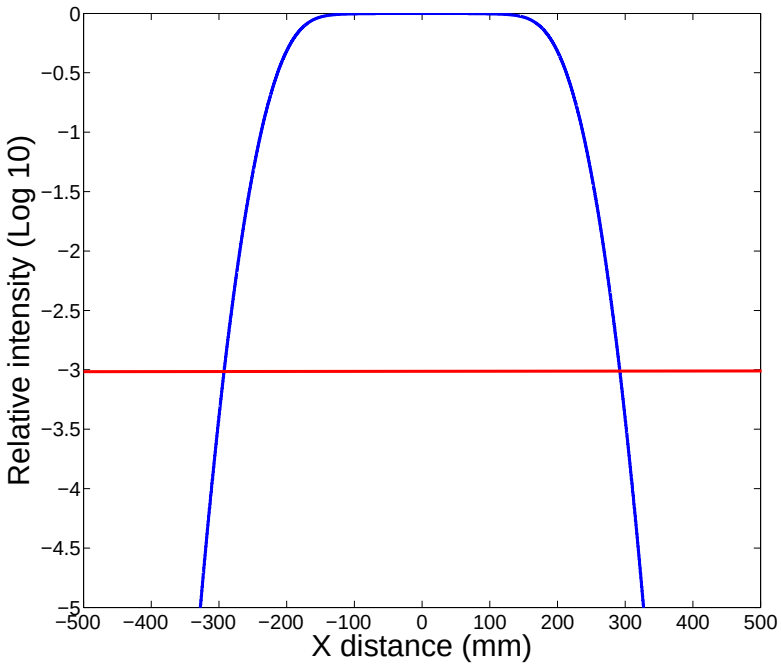

Figure 6.16: Normalized dose profile for $Mag = 30$, the dose drops to 10^{-3} order in 91.9 mm, which is less than the 15 cm requirement.

photons are involved. Therefore, a modified simulation algorithm was performed to simulate the attenuation of the collimator.

1D dose profile simulation for real collimator

The extra-focal radiation dose profile with a 6.35 mm (0.25 in) lead collimator placed at various source-to-collimator distances were simulated. The simulation evaluates the worst scenario, which assumes a monochromatic x-ray of 80 keV. The attenuation coefficient of lead at 80 keV was used, which is $\mu_{80keV} = 2.74/\text{mm}$. Table 6.4 summarizs the w_2 measured at 10^{-3} order for all simulated magnification factors. Figure 6.17(a) shows the simulated dose profile plotted in log scale for magnification factor $Mag = 25$, where the source-to-collimator distance is 38.5 mm. The dose still drops very fast off the detector edge, as the extra-focal radiation drops to 10^{-3} order in $w_2 = 131.8$ mm, which is still less than the 15 cm requirement.

Table 6.4: w_2 for various collimator magnification factor, Mag, using 1/4 in lead collimator

Mag	1	5	10	15	20	25	30
$w_2(mm)$	5.7	24	48.3	74.3	102.3	131.8	164.8

The two simulation models using "ideal" and "real" collimators were compared at the same parameters, and the simulated dose profiles are plotted in Figure 6.17(b). Both simulations are done with the same collimator-to-source distance. The comparison shows that the dose drops more slowly in the worst scenario (80 keV x-ray photon and 6.35 mm lead collimator) than in the "ideal" collimator, as the w_2 were 131.8 mm vs. 76.6 mm. The true extra-focal radiation dose profile should be between these two simulated profiles. Even though the dose drops more slowly in the worst case scenario, the w_2 was still less than the required value of 15 cm, since the 6.35 mm lead sheet blocked most of the x-rays.[3]

[3]Only $e^{-2.74\times6.35} = 7.2\times10^{-8} = 7.2\times10^{-6}\%$ x-ray photons can pass through the 6.35 mm thick lead.

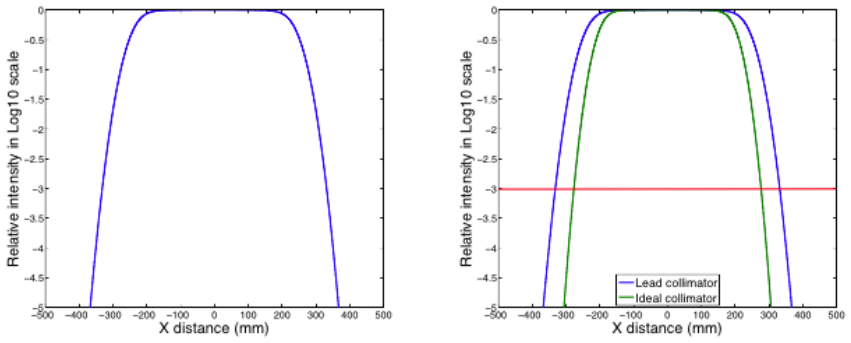

(a) (b)

Figure 6.17: (a) Extra-focal radiation dose profile for $Mag = 25$ with 1/4 in lead collimator. The w_2 is 131.8 mm, which is less than the 15 cm requirement. (b) Comparison of "Ideal" collimator and "real" collimator for $Mag = 25$. The blue curve shows the simulated dose profile with "ideal" collimator, which can block all x-rays. The green curve shows the simulated profile with a 6.35 mm lead collimator with 80 keV monochromatic x-rays. The "real" scenario shows slower dose drop. However, both w_2s are less than the 15 cm requirement.

The widening of the profile was mostly due to the relatively short path at the edges of the collimator opening, which blocks less x-ray photons.

Due to the relatively long focal spot size in the x-direction and relatively small detector in experimental setup, a narrower tungsten collimator was implemented. The tungsten collimator was 5 mm wide, and was collimated the exposure area to 57.5 mm wide on the detector (measured width in experiment). To compare the simulation results with the experimental measurement, another set of simulations were performed using a narrower tungsten collimator. The simulation used a 12.7 mm (0.5 in) tungsten block as a collimator. In this set of simulations, to evaluate impact of the magnification factor, we assumed the collimated exposure width was kept same when changing the magnification factor.[4] Simulations were performed at various magnification factors, Mag. The w_2 at 10^{-3} order were measured and listed in Table 6.5.

[4]The width of the tungsten collimator opening changes with the magnification factor to maintain the same collimated area.

Table 6.5: w_2 for various collimator magnification factors, Mag, using 1/2 in tungsten collimator

Mag	1	5	10	10.5	15	20	25	30
$w_2(mm)$	4.0	19.4	41.0	43.5	66.5	97.2	133.8	178.8

Experimentally measured dose profile

Projection images of the 6.35 mm thick lead collimator were collected. Due to a larger focal spot size in the x- direction and the small detector, a narrower tungsten collimator was implemented to narrow the beam in order to measure the radiation distribution outside the collimated area, as shown in Figure 6.14. The tungsten block was 13.7 mm thick, had a sharp edge, and was separated by 5 mm. The detector pixel reading was used as a quantitative measure of the imaging dose. To reduce the imaging noise, 100 frames of collimator images were acquired. 100 frames of the dark field images were also acquired to perform an offset correction to the collimator images. Each image was acquired at 80 kVp and 5 mA anode current in a 30 ms pulse. Figure 6.18(a) shows the corrected projection image of the collimator. As discussed in previous sections, analysis was focused on the dose profile in the x-direction. Figure 6.18(b) shows the raw pixel count. The FWHM of the raw profile was measured and used to determine the magnification factor, Mag, as

$$Mag = \frac{FWHM}{5\ mm} - 1 \tag{6.6}$$

where the 5 mm is the width of the opening of the extra tungsten collimator. By normalizing and plotting the dose profile on a log scale, the w_2 where the dose drops to the 10^{-3} order was measured. To compare to the simulation results, the w_2 at 10^{-1} and 10^{-2} orders were also measured.

The measured $FWHM$ of the dose profile was 302 pixels, which was 57.38 mm in width. The calculated collimator magnification factor was 10.47. The normalized dose profile is

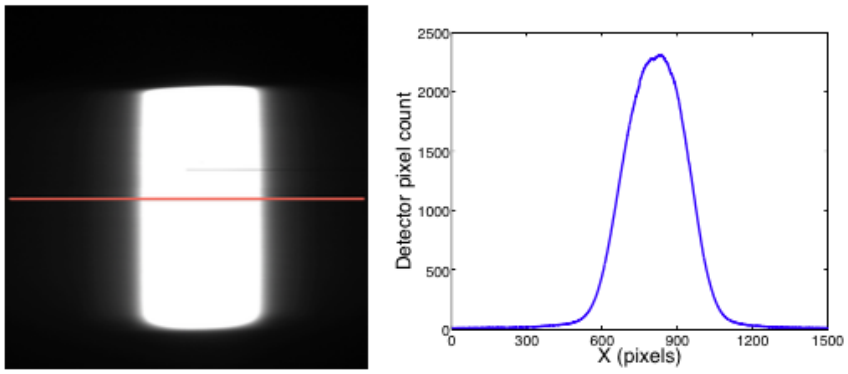

(a) (b)

Figure 6.18: (a) Projection image of the lead collimator. The dose profile along the x-direction was measured, as marked by the red line. (b) The raw pixel number profile of the collimator image along the x-direction (the red line shown in (a)).

plotted in log scale in Figure 6.19. As shown in the figure, the dose drop rate decreases. The dose never dropped to 10^{-3} order as expected. Table 6.6 lists the measured w_2 where dose drops to the 10^{-1} order and 10^{-2} order.

Table 6.6: Measured w_2 for dose to drop to the 10^{-1} order and 10^{-2} order in the x direction.

Order	10^{-1}	10^{-2}	10^{-3}
w_2 (mm)	18.24	59.47	N/A

Comparison of experiment and simulation results

The measured extra-focal radiation dose profile was compared to the simulated dose profile. Figure 6.20 shows the normalized dose in log scale for the experimentally measured dose, 6.20(a), and the simulated dose, 6.20(b) and 6.20(c). The simulations used the same condition: 1060 mm SID, a 13.7 mm tungsten collimator with 5 mm opening, and $Mag = 10.47$. The w_2 were also measured from the dose profile at the 10^{-1}, 10^{-2} and 10^{-3} orders of dose level. Table 6.7 summarizes the measured w_2 of the experimental dose profile and

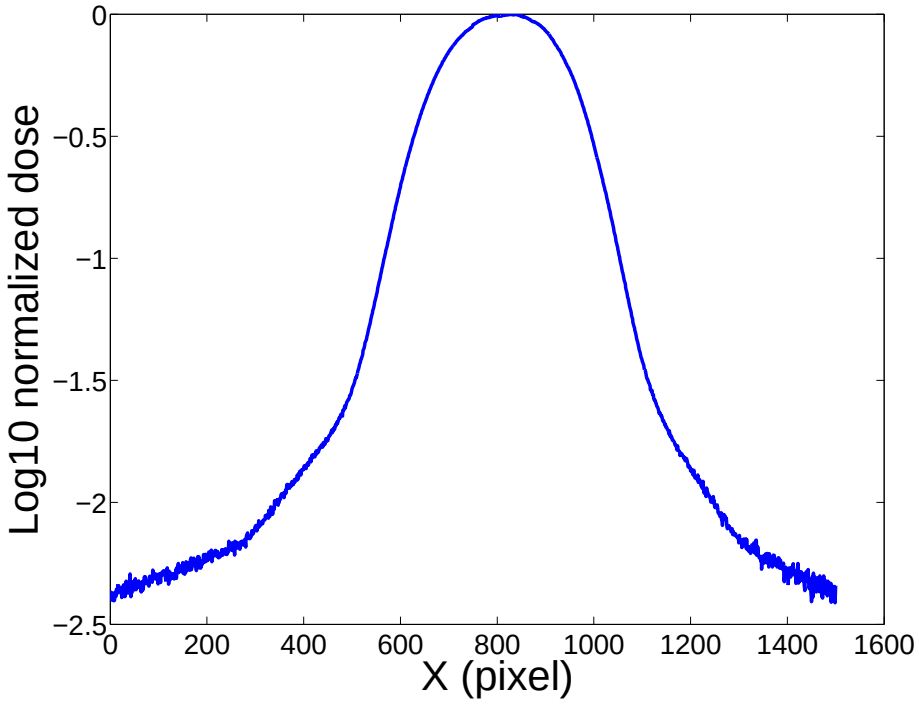

Figure 6.19: Experimentally measured normalized dose profile plotted in log scale. The dose does not drop to the expected 10^{-3} order.

simulated profile, and the relative error for all three magnitude orders. The simulation model 0 (Simu. M0, Figure 6.20(b)) refers to the the algorithm assuming "ideal" collimator, while the simulation model 1 (Simu. M1, Figure 6.20(c)) is the worst scenario assuming a monochromatic x-ray of 80 keV.

Table 6.7: Comparison of the experimentally measured w_2 and simulated w_2 using both simulation models.

Order	Exp. (mm)	Simu. M0 (mm)	Error (%)	Simu. M1 (mm)	Error (%)
10^{-1}	18.24	13.5	−26.0	20.9	+15.1
10^{-2}	59.47	24.5	−58.7	33.8	−43.0
10^{-3}	N/A	32.5	N/A	43.5	N/A

As shown in the figure, the experimentally measured dose profile still shows a fast drop

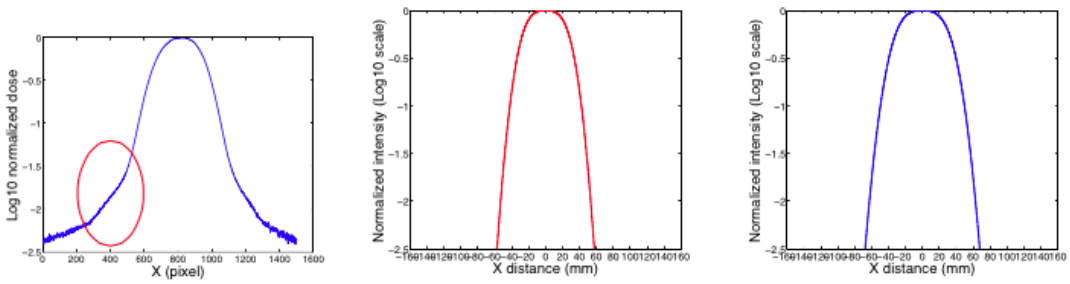

(a) (b) (c)

Figure 6.20: (a) Experimentally measured dose profile in the x-direction. The dose drop rate decreases dramatically at approximately $10^{-1.5}$ order. (b) Simulated dose profile using an ideal collimator (Model M0) for the same condition. (c) Simulated dose profile using a 13.7 mm tungsten collimator, and 80 keV monochromatic x-rays (Model M1).

in dose at the edges of collimator. The drop rate:

$$Rate = \frac{\mathrm{d}}{\mathrm{d}x} \log Dose \tag{6.7}$$

decreases as $|x - x_0|$ increases, where x_0 is the center of the collimated area. At the dose level of the $10^{-1.5}$ order (red circled region in Figure 6.20(a)), the change in the drop rate becomes significant. However, the drop rate in the simulated cases, both using model M0 and M1, stay almost the same as $|x - x_0|$ increases. Due to this unexpected dose drop rate in the experimentally measured dose profile, the w_2 at 10^{-3} order was not measured in the experiment.

By comparing the measured w_2 at different dose levels for experiment and two simulation models (Table 6.7), we can see the experimentally measured w_2 at 10^{-1} order was 18.24 mm, which was in between the simulation results of 13.5 mm in ideal situation (model M0), and 21.0 mm in the worst scenario (model M1). As briefly discussed before, the real extra-focal radiation dose profile should be between the results from simulation models M0 and M1. The measured results agree with the previous discussion.

However, at the order of 10^{-2}, the experimentally measured w_2 was 59.47 mm, which was

greater than both the simulated w_2 of 24.5 mm (model M0) and 33.9 mm (model M1). The discrepancies between the simulation and experiment results were due to the changed dose drop rate measured in experiment. Efforts to explain these discrepancies will be discussed in the following sections.

Discussions on experiment and simulation discrepancy

Discrepancies between simulation and experimental results were found. This section discusses the possible reasons for these disagreements.

By looking at the experimentally measured dose profile, as shown in Figure 6.19, it can be seen that the dose profile becomes noisy when $|x - x_0|$ increases. Since the detector reading was a quantitative measure of the dose, the detector noise may be the reason for the noisy signal. The detector noise was evaluated by measuring the standard deviation (σ) of a small region in the dark field images, already an average of 100 dark field images in order to reduce the noise. The region of interest was near the region showing noisy signal. The σ was measured several times, and the average standard deviation was used as a measurement of the detector noise. Table 6.8 lists the measured noise and the average value. The average noise was $\sigma = 7.19$.

Table 6.8: Summary of measured noise in the dark field images.

	1	2	3	4	Average
σ	7.18	7.25	7.35	6.99	7.19

The raw dose profile in Figure 6.18(b) shows that the maximum dose (measured in detector counts) is ~ 2300. Comparing the measured noise and the peak dose, the order of the noise is about

$$O(Noise) \sim \log(\frac{7.2}{2300}) \sim -2.5 \tag{6.8}$$

which was about the same order where the noisy signal showed in the measured dose profile.

Moreover, since the minimum count that the detector can readout is 1, we have a measuring limit of the detector of

$$O(limit) \sim \log(\frac{1}{2300}) \sim -3.4 \tag{6.9}$$

Combine that with the noise level of the detector, we can say any dose measurement around the order of 10^{-3} using this detector is inaccurate. Therefore, we cannot use the experimental method described in this section to accurately evaluate the extra focal radiation up to 10^{-3} order. However, the experimental methods still can be used to evaluate the extra-focal radiation up to 10^{-2} order, given the fact that the noise only kicks in until the 10^{-2} order.

Now, the focus shifts to finding out the reasons causing the discrepancies between simulation and experiment at 10^{-2} order. Noticing the red circle region in the experimentally measured dose profile (Figure 6.20(a)), there is a "hump" added to the dose profile that decrease the dose drop rate. This "hump" is the cause of the discrepancy of the simulation and experiment. Possible explanations for this "hump" could be the leakage radiation of the tube, the penumbra effect at the collimator corners, or scattering x-rays. All will be discussed, respectively, in the following sections.

Leakage radiation of the tube

The CNT source array has leakage radiation at 80 kVp. The leakage radiation can be reduced with further conditioning of the tube. The leakage radiation may introduce extra radiation and cause the discrepancy between the simulation and experiment.

The leakage radiation was constant when the anode reached 80 kVp. To isolate the leakage radiation, true dark field images and dark field images with the anode at 80 kVp (dark field image + leakage radiation image) were acquired. By subtracting the true dark field image from the dark field images with anode on, the leakage radiation images can be separated. Figure 6.21 shows the subtracted leakage radiation image and a line profile across the collimated area (red line). The image show a bright spot in the collimated area due to the leakage radiation of the tube. The line profile was averaged over a strip of 11 lines to

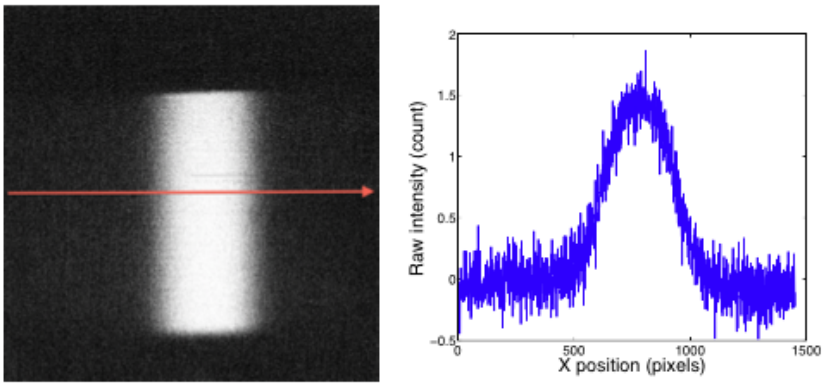

(a) (b)

Figure 6.21: (a) Subtraction image of the leakage radiation. The bright collimated area shows the leakage radiation. The red arrow marks the analyzed line profile. (b) A line profile across the collimated area. The leakage radiation contributes little radiation.

reduce noises. From the line profile, an intensity of ~ 1.5 was measured at the peak in the collimated area, and almost 0 outside the region, since the leakage radiation is small and most of it has been attenuated by the collimator. Thus, the leakage radiation barely contributes to the experimentally measured dose profile, as the leakage radiation was on the order of

$$O(leakage) \sim \log(\frac{1.5}{2300}) = -3.2 \tag{6.10}$$

Therefore, the tube leakage radiation was not the reason of the discrepancy between simulation and experiment. The leakage radiation also contributed little to the extra-focal radiation.

Penumbra effect of the collimator

The penumbra effect of the collimator usually happens at the corner of the collimator, as illustrated in Figure 6.22, where the collimator material was thin in the x-ray path, thus the x-ray photons cannot be fully attenuated. Cutting the edges of collimator precisely can prevent such an effect. However, in the experimental setup, there is no access to a dedicated collimator, so a tungsten block with a sharp edge was used as a collimator instead. This

may have caused the penumbra effect.

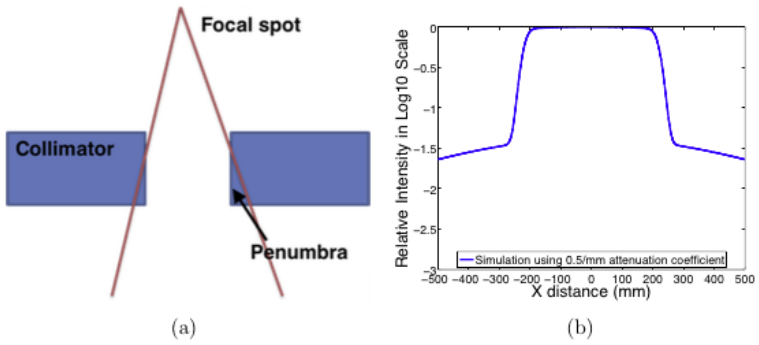

Figure 6.22: (a) Illustration of the penumbra effect caused by the collimator. (b) A simulation with a low attenuation collimator.

In the second simulation model, this effect was already taken into account. To form a penumbra as strong as was measured in the experiment, the collimator must be made using a material with very low attenuation coefficient or very thin material, as illustrated in Figure 6.22(b). An arbitrary, small attenuation coefficient of $\mu = 0.5/mm$ was assigned to a 6 mm thick collimator at $Mag = 15$ to demonstrate the idea.

Therefore, the penumbra effect of the collimator was not the reason of the discrepancy between simulation and experiment.

Scattered x-rays

The interactions between x-ray photons and the collimator material cause scattered x-rays, which could contribute to the "hump" in the extra-focal radiation measurement. X-ray scattering was not included in the simulation model; therefore, this may be the source of discrepancy. If the scattered x-ray intensity can be measured, then the hypothesis can be verified.

However, direct measurement of scattered x-rays is difficult, because the scattered signal is much smaller compared to the primary beam passing through the collimator. To evaluate the contribution of the scattered x-rays, scattered signal needs to be isolated from the primary

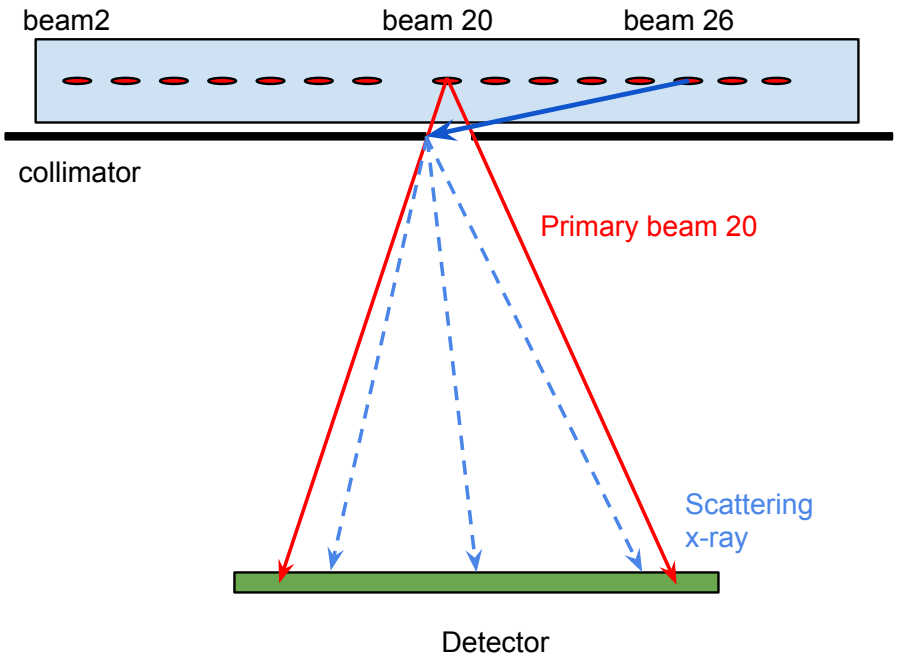

Figure 6.23: Illustration of the experiment to evaluate scattered x-rays. The collimator was aligned to source 20, which is located roughly in the center of the source array. By firing source 20, the primary beam (red line) will pass through the collimator and shine on the detector. The primary beam and the scattered x-rays mix together, thus it is hard to measure the scattered x-rays. But by firing source 26, which is 48 mm away from source 20, the primary beam and scattered x-rays can be separated. The primary beam of source 26 (dark blue line) is $\sim$ 55 cm away from the center of the detector based on a simple geometry calculation. But the scattered x-ray (blue dashed line) can reach the detector and can be measured.

x-ray beam. Given the setup of the experiment, the edges of the collimator opening will generate the most scattered x-rays. So we designed a simple experiment to separate the primary beam and scattered signals so that we can evaluate the influence of the scattered x-rays. The experiment is illustrated in Figure 6.23. (*Note: The illustration was not drawn to scale.*) The same collimator as that used in the extra-focal radiation measurements was used here. The collimator opening was aligned to source 20, which is roughly in the center of the source array. The primary beam of source 20 was collimated to the detector, therefore it was very difficult to measure the scattered x-ray signal from this source. To separate the

primary beam and the scattered x-ray, we fired all the x-ray sources inside the source array one by one, and examined the image acquired from each source to determine which sources have the primary beam and scattered x-rays separated. When firing the sources at the two ends of the source array, the primary beam and scattered x-ray were definitely separated, however, due to the large scattering angle, the scattered x-rays were very weak. Figure 6.24 shows the image acquired for source 2, which is at the left end of the source array. The image was similar to the leakage radiation image acquired, the leakage radiation is stronger than the scattered signal. By examining the projection images from all sources, source 26 was found to have a good separation between primary beam and scattered signal. The source was 48 mm away from source 20, therefore the primary beam of it was ~ 55 cm away from the center of the detector according to the geometric relationship. This distance is sufficient to isolate the scattered x-ray from the primary beam.

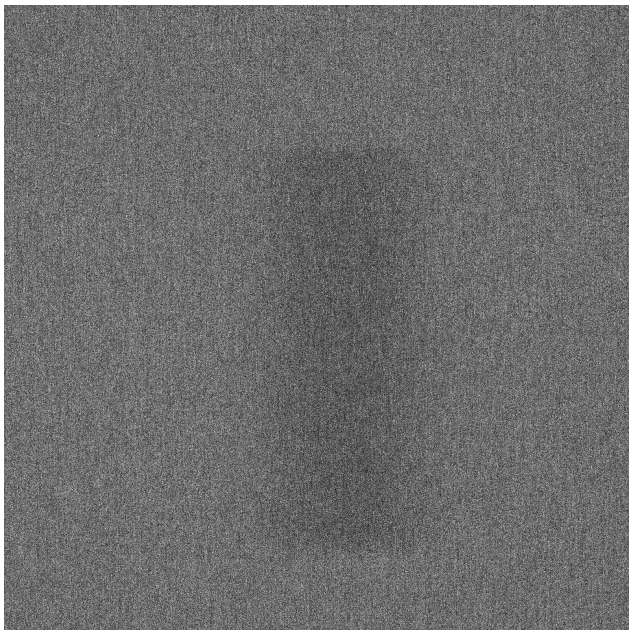

Figure 6.24: Projection image of scattered image of source 2. The image is similar to the leakage radiation image since the scattered signal is much less than the leakage radiation

Scattered x-ray image of source 26 was acquired. As shown in Figure 6.25(a), the bright band along the x-direction was the scattered signal from the edge of the collimator. The

intensity line profiles across the image in x and y directions are plotted in Figure 6.25(b). The profile in blue shows the intensity of scattered x-rays in the x-direction, while the red profile is the scatter in the y-direction. The average intensity of the scattering signal along x-direction was ~ 13. This value can be used to estimate the scattered x-ray intensity from source 20. For source 20, since the collimator opening was aligned to the source, the scattered at the collimator edge should be slightly stronger than the scattered from source 26. But the scatter signal should be on the same order. Therefore, the order of the scattering x-rays was estimated to be:

$$O(scattering) \sim \log(\frac{13}{2300}) \sim -2.2 \tag{6.11}$$

The order of the scattered x-ray was in the range of the "hump" signal in the measured extra-focal radiation dose profile. *Therefore, we indirectly verified that the scattered x-ray was the source the discrepancy between the simulation and experiment.*

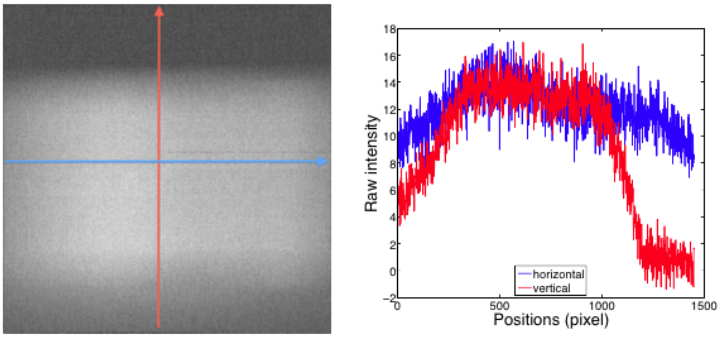

Figure 6.25: (a)Scatter x-ray image of source 26. The bright band in the image is due to the scatter radiation from the collimator edge. (b) Intensity profiles along the x-direction (blue) and y-direction (red).

The scattered x-ray forms a "band" along the y-direction, the scatter signal drops quickly to almost "0" at the top of the "band". This may be because the focal spot was aligned better with the top edge of the collimator opening, thus there was less scatter signal at the large scatter angle. By changing the position of the focal spot relative to the collimator

opening, the scatter intensity off the top edge and bottom edge change. If we move the collimator up, the scatter intensity from the top edge will increase, while the scatter from the bottom will decrease. Another simple experiment was designed to verify this hypothesis.

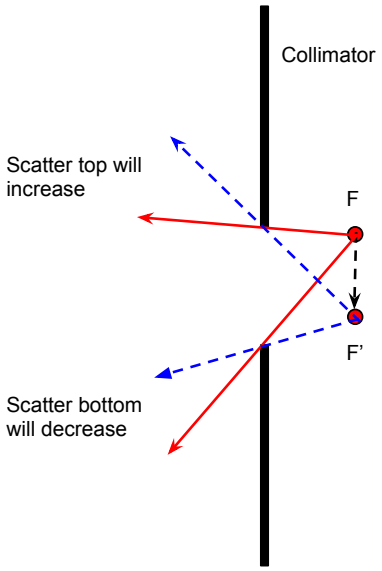

Figure 6.26: By changing the relative position of the focal spot and collimator opening, the scatter intensity on the top and bottom edge will change. Initially, the focal spot F is aligned better with the top edge, therefore there is less scatter off the top edge. By gradually moving the collimator up, the focal spot moves to F' relative to the collimator, and the scatter off the top edge will increase while the scatter from the bottom edge will decrease.

The experiment is illustrated in Figure 6.26. Initially, the focal spot was aligned better with the top edge of the collimator opening, resulting in less scatter off the top edge, as shown in Figure 6.25. As the collimator moved up, the focal spot F moved down relative to the collimator to a lower position F', where the scatter from the top edge will increase and the scatter off the bottom edge will be reduced.

The scattered x-ray intensities were measured in the same way so that the scatter signal could be compared as the collimator was moved. Figure 6.27 shows the acquired image with the collimator moving 2 mm (6.27(a)) and 4 mm (6.27(c)), and the line profile across x and y directions 6.27(b) and 6.27(d), respectively. As expected, by moving the collimator up, the

scatter "band" structure moved up as well. The profile in the y-direction shows the scattered x-ray slowly drifting to the top as the collimator moved up. The intensity of the scattered x-ray in the y direction was comparable to the scattering in the x-direction.

Even though the scattering x-ray intensity on source 20 cannot be directly measured, the scattered x-rays of source 26 was successfully isolated and measured . Assuming the magnitude of the scattered x-rays of source 20 was on the same order of beam 26, which was true in the experiment setup, we can conclude that the scattering x-ray photons from the edge of the collimator opening contributed to the "hump" we measured in the extra-focal radiation experiment, and it was the main source of the discrepancy between the simulation and experiment.

6.3.4: Discussion and Conclusion

The extra-focal radiation of the CNT source array model 2008-08-L75-002 was evaluated. The evaluation consisted of simulation and experimental measurements. The criteria for the extra-focal radiation was based on requirement from IEC 60601-2-54, which states the boundary of the radiation should be less than 15 cm at the 1 m source-to-detector distance. However, the IEC doesn't specifically state the criteria to determine the boundaries of the x-ray radiation. Neither an absolute entrance dose nor a relative dose to the exposing area is given. In this study, we initially used the criteria of a relative dose of 0.1% to the exposing area (3-order magnitude dose drop) to determine the boundaries of the extra-focal radiation. Given the performance of this tube, the 3-order drop of the dose should be enough to meet the dose requirement. Currently, the source is running at 80 kVp and 5 mA anode current. The pulse width of each pulse is programmable. When acquiring images with the Varian 3030D detector, which was used to experimentally measure the dose profile in this study, a maximum 30 ms pulse was used for full resolution mode (1×1 binning), and a 12 ms pulse width was used for the 2×2 binning mode. Based on the pulse width, a maximum of 0.15 mAs tube exposure was used in one projection view, resulting a maximum 1.3 mR exposure

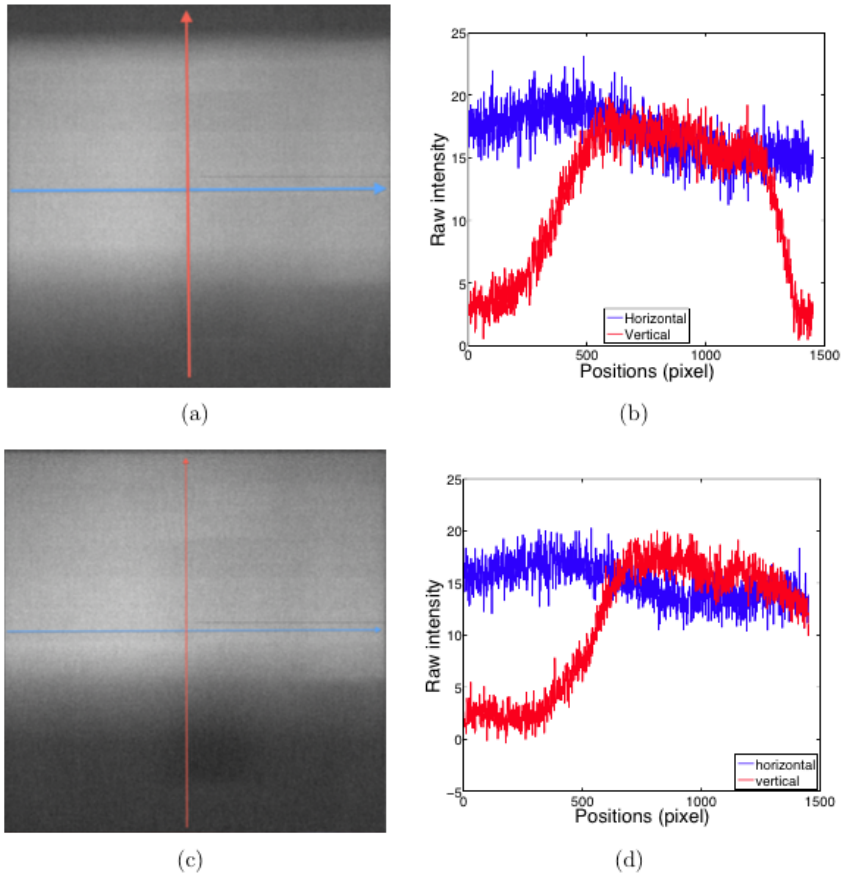

Figure 6.27: (a) Projection image of the collimated area with source 26 fired. The image shows the scattered x-ray intensity. The collimator was moved up 2 mm. (b) The line profile across x- (blue) and y- (red) direction for figure (a). (c) Scattering x-ray image with collimator moved up for 4 mm. (d) The line profile along x- and y- direction for figure (c).

on the exposing area. Using the 3-order magnitude dose drop as the criteria to determine the width of extra-focal radiation, it is expected that the radiation drops to 1.3 μR within 15 cm, which should meet the dose requirement.

The developed simulation models do not have calculations of the scattered x-rays. To better estimate the extra-focal radiation, the scatter model should be included. However, accurately simulating the scatter is difficult since the scattered x-rays usually do not have a direction, and the scatter signal depends on the collimator material and the spectrum of the x-ray source. Therefore, a simple simulation model was used to focus on the dominant

factors that cause extra-focal radiation, such as focal spot size, position of the collimator, etc. Based on the simulation results, the extra-focal radiation, which is the convolution of system geometries, drops quickly off of the collimated area. The closer the collimator is to the focal spot, the greater the distance required for the extra-focal radiation to drop to the 10^{-3} order.

The detector reading was used to measure the dose profile experimentally. Due to the limited ability to measure low dose and the detector noise, only dose up to the 10^{-2} order could be accurately measured using this detector. The scattered x-rays from the collimator contributes approximately 10^{-2} order of x-rays to the extra-focal radiation profile. The measured extra-focal radiation is a mix of the real extra-focal radiation and scatter radiation, which becomes the dominate radiation as distance increases from the edge of the collimated area. Therefore, the 3-order dose drop cannot be used as the criteria to determine the width w_2 of the extra-focal radiation. Expanding the requirement to 1% (2-order magnitude drop), a maximum of 13 μR radiation would be expected as the criteria to define the boundary of the extra-focal radiation.

The scattered x-rays can contribute up to 1% of the dose of the extra-focal radiation. This is because the collimator used in this study was simply a cut hole in a lead sheet, and two tungsten blocks. The opening of the collimator was not precisely cut to match the x-ray beam path, resulting in increased scatter from the collimator. We have demonstrated this by using a simple experiment. If a dedicated collimator is made and used in the experiment, the measured extra-focal radiation could be reduced by eliminating the scattered x-rays.

Section 6.4: Anode Thermal Analysis

6.4.1: Introduction

As discussed in Section 2.5, one of the main tradeoffs in the x-ray tube design is the photon flux and the focal spot size on the anode. Increasing the tube current (electron beam

power) can increase the x-ray photon output, however, the power is limited by the anode melting and lifetime degradation due to the thermal cycling.

The maximum power for conventional x-ray tubes running in DC mode have been studied both theoretically and experimentally.[75, 76] The CNT based x-ray source can be operated more efficiently using pulsed mode, due to the fast switching capability of CNT cathodes. The anode thermal loading in CNT x-ray sources needs more detailed study.

The purpose of this section is to study the factors that determine the maximum power of the CNT x-ray source in both DC and pulsed modes.

6.4.2: Simulation Model

In the CNT based field emission x-ray tubes, as shown in Figure 6.28, the electron beam is generated by applying an electric field between the CNT cathodes and gate mesh. The emitted electrons are accelerated and focused by focusing electrodes toward anode. The bombardment of high-energy electrons heats the target area on the anode and produces a local high temperature distribution. Finite element analysis simulations were used to study the thermal loading on the anode. For a given anode of fixed dimensions; and knowing the incident electron beam power, exposure time, and duty cycle, the anode temperature distribution was determined by solving the time dependent inhomogeneous heat equation:[77]

$$\rho c_p \frac{\partial T(\mathbf{x},t)}{\partial t} = (P_{in}(\mathbf{x},t) - P_{rad}(\mathbf{x},t)) \cdot t - \nabla \cdot (k \nabla T(\mathbf{x},t)) \tag{6.12}$$

where ρ is the density of the anode material, c_p is the heat capacity, and k is the thermal conductivity. Both k and c_p are functions of the temperature T. The term $k\nabla^2 T(\mathbf{x},t)$ describes the heat conduction in the anode, the term $P_{in}(\mathbf{x},t)$ describes the incident power due to the interaction of the electron beam with the anode, and the term $P_{rad}(\mathbf{x},t)$ describes the thermal energy radiating out from the anode surface due to the grey body radiation,

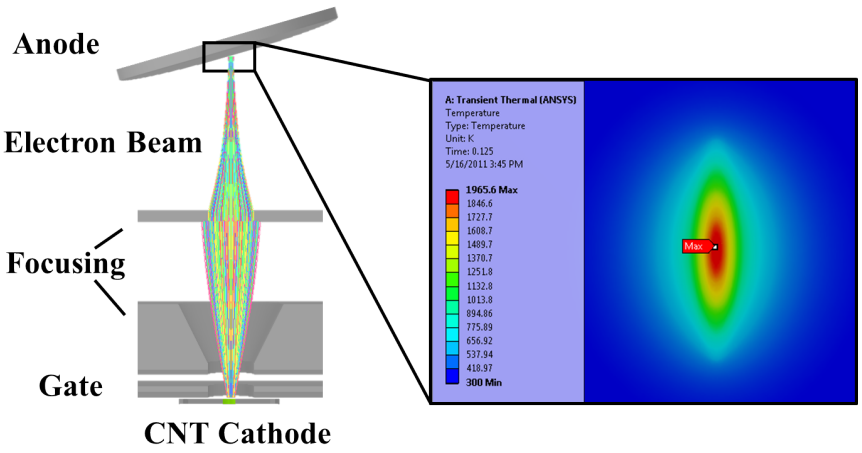

Figure 6.28: Schematic of the structure of the CNT based field emission micro-focused x-ray tube and the demonstration of the temperature distribution on the anode surface.

given by $P_{rad} = \epsilon\sigma(T^4 - T_0^4)$.[5]

Finite element analysis was employed to numerically solve the heat equation. In this study, the Transient Thermal Solver in a commercial software, Ansys Workbench 12.1 (Ansys Inc. Canonsburg, PA), was used to analyze the anode heat load. The temperature dependency of the heat capacity and thermal conductivity is very important in solving the heat equation. The thermal diffusivity $\alpha(T)$, which is defined as:

$$\alpha(T) = \frac{k(T)}{\rho c_p(T)} \tag{6.13}$$

is a measure of how fast heat transfers in a material. Figure 6.29 shows the temperature dependency of thermal diffusivity for tungsten; illustrating the large change in $\alpha(T)$ from 0.66 cm^2/s at 300 K to 0.24 cm^2/s at 3000 K.[78] It is essential that this temperature dependence of the thermal diffusivity be included in the simulation.

The anode is usually mounted at a tilted anode angle, θ. The image quality is determined by the effective focal spot size, f_s. The real focal spot size, defined as the area bombarded by the electron beam, is an ellipse with a short axis $a = f_s$, and long axis $b = ef_s = f_s/\sin\theta$,

[5] ϵ is the surface emissivity, which depends on materials and the surface smoothness.

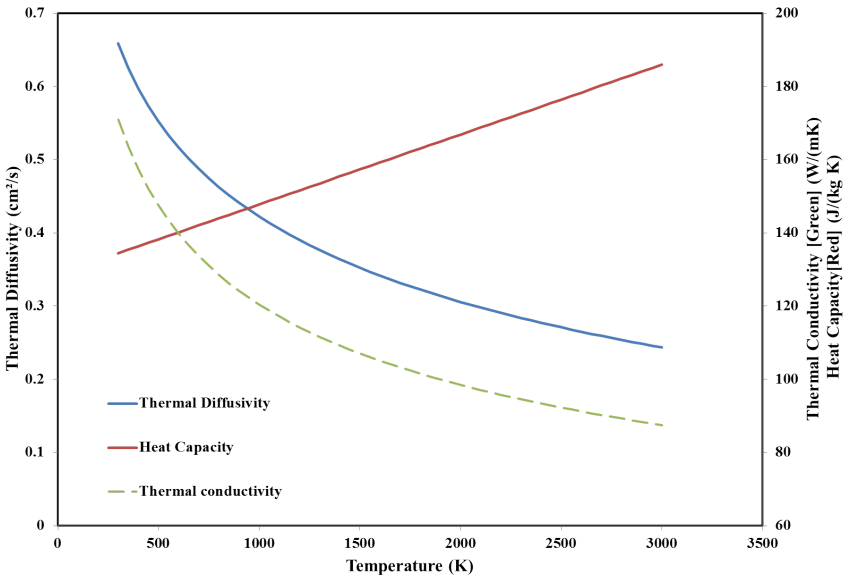

Figure 6.29: Temperature dependence of the thermal diffusivity, thermal conductivity, and heat capacity of tungsten. The thermal conductivity decreases with the temperature while the heat capacity increases with the temperature, thus the thermal diffusivity decreases from 0.66 cm^2/s at 300 K to 2.4 cm^2/s at 3000 K. It is important to include the temperature dependency of both the thermal conductivity and heat capacity in anode thermal analysis.

where $e = 1/\sin\theta$ is the projection factor. In this paper, all focal spot sizes refer to the effective focal size, f_s. However, the real focal spot size, which takes into account the anode angle, was used in the simulations.

6.4.3: Validation of the Model

Validation of the simulation model was done by comparing the simulation results with those of the electron beam melting experiment reported by D E Grider.[75] The compared parameter was the size of the melted anode area. The simulation conditions were identical to the experimental setup described in the paper. Cylindrical anodes made of tungsten and molybdenum, with a 1 cm diameter and 2.5 cm height, are hit by high energy electron beams produced by a micro-focused x-ray tube. The incident electron beam's power ranged from 3 W to 18 W in 3 W increments. The focal spot radius of the electron beam was measured to

be 7 µm, beam penetration depth was set to 10 µm, and the exposure time was 60 s. The electron beam penetration depth, d, in the micro-focus tube is given by: [21]

$$d(\mu\text{m}) = \frac{2.76 \times 10^{-2} A E_0^{1.67}}{\rho Z^{0.89}} \tag{6.14}$$

where A is the atomic weight, Z is the atomic number, and E_0 is the accelerating voltage in units of kV. For a typical x-ray tube running from 30 kVp to 100 kVp, the electron beam penetration depth of tungsten is calculated to be between 1.6 µm and 12.5 µm. However, these simulations used different electron beam penetration depths ranging from 1 um to 15 um showed that the temperature distributions on the anode were not significantly dependent on the penetration depth, in this range. Therefore, the penetration depth is not a sensitive parameter in the simulation. The thermal conductivity, k, and heat capacity, c_p, of the anode material used in the simulation are temperature dependent. Temperature distribution on the anode was simulated and the melted spot size was determined by the area where the temperature was greater than the melting temperature of the anode material. The simulated melting spot size was then compared with experimentally measured results reported by D E Grider.

The simulation results of the relationship between the melted area and electron beam power are plotted in Figure 6.30. The relative error between simulated results and experimentally measured results were less than 10%. The results suggest great agreement between simulation and experiment. It is concluded that the simulation method can be used as a reliable numerical tool to analyze the anode heat load in the micro-focus x-ray tubes.

6.4.4: Anode heat simulation for CNT micro-CT

One of the advantages of the CNT based field emission x-ray tube is that the tube can be electronically programmed for fast switching. Therefore, the tube can be operated in pulsed mode to achieve high temporal resolution.[79] Respiratory and cardiac gated micro-

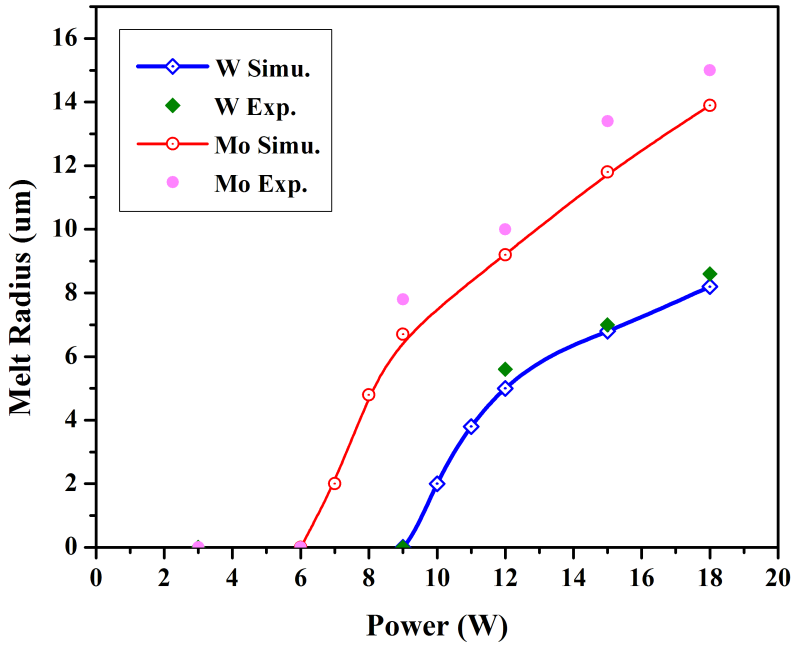

Figure 6.30: Comparison of electron beam melting radius in the micro-focus tube between simulated and experimental results. The open symbols with fitted smooth lines are simulation results; the scattered solid points are experimental results. The agreement between simulated and experimental results suggests that the simulation is reliable for investigating thermal loading of the anode.

CT imaging to non-periodic physiological signals have been reported on the CNT micro-CT system.[45, 79] For example, to get clear dynamic imaging of a mouse cardiac cycle, a temporal resolution of 10 ms is desired. To perform prospective respiratory gating, only one projection view (one x-ray pulse) is used during each respiratory cycle of a small animal ($\sim$ 1 second for mice). Thus, the typical tube operation duty cycle is close to 1%.[79]

To study the factors determining maximum CNT x-ray tube power, the same pulse chain of 10 ms pulses and 1% duty cycle were used. The simulated tungsten anode was a cylinder with a 4 mm diameter and 5 mm height, which is very similar to the dimension of the anode used in the actual CNT micro-focus x-ray source. An effective focal spot size (f_s) varying from 20 µm to 200 µm was used to study the maximum power. A set of simulations operated

in DC mode at 10° anode angle is compared with the pulse mode at pulse width of 10 ms. Three sets of simulations in both DC mode and pulsed mode were performed with anode angles of 6°, 10°, and 20° respectively, to find out how the anode angle affects the maximum tube power. The criteria to determine the maximum power is when the maximum anode temperature does not exceeds 80% of the melting temperature of the material, 3000 K for tungsten.

Maximum power in DC mode

Maximum power of the CNT micro-focus tube at a 10° anode angle for various focal spot sizes was studied for both DC and pulsed modes. The results are shown in Figure 6.31. In conventional micro-focus x-ray tubes with stationary anodes in DC mode, an empirical formula of the maximum power, $P(W)$, as function of focal spot size $f_s(\mu m)$ has been reported by Flynn et. al. as:[76]

$$P = 1.44 f_s^{0.88} \tag{6.15}$$

These empirical results are also shown in Figure 6.31 as a reference. At 10° anode angle, the results are in good agreement with this empirical formula.

Figure 6.32 shows the dependence of the maximum power on the effective focal spot size for three different anode angles of 6°, 10°, and 20°, respectively. It can be seen that the maximum power in DC mode for small anode angles is higher than that at larger anode angles. This is expected because the smaller the anode angle, the larger the actual focal spot size. Thus, heat can transfer more quickly. The results show that the dependence of the maximum power, P, on the effective focal spot size, f_s, can be described by a simple power law for all anode angles,

$$P(W) = (\frac{0.24}{\sin\theta} + 1.64) f_s^{0.73}(\mu m) \tag{6.16}$$

This simple relation fits well for all three anode angles. In the case of the 10° anode angle, this

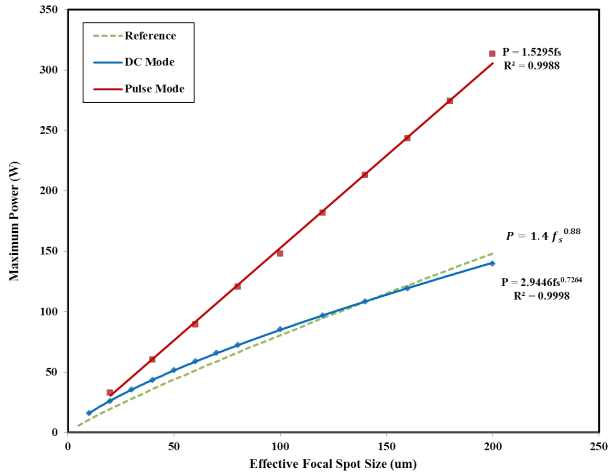

Figure 6.31: Maximum power of a micro focus CNT x-ray tube as a function of effective focal spot size for a 10° tungsten anode. In DC mode, the simulated results agree well with Flynn's empirical formula (dashed curve). However, in pulsed mode, the allowed maximum power is approximately a factor of 2 higher.

formula is close to the empirical relationship given by Equation 6.15. However, Equation 6.15 cannot describe the results for different anode angles.

Maximum power in pulse mode

The real focal spot area, defined as the area bombarded by the electron beam, is much smaller than the anode metal piece in the micro-focus tube. The focal spot area can be heated up/cooled down rapidly when the electron beam is turned on/off within a short pulse. Figure 6.33 shows the maximum temperature on the anode vs time, up to 50 ms, for the tube running at 50 kVp, 3 mA, 10 ms x-ray pulse width, and 100 µm effective focal spot size. The maximum temperature, at the center of the focal spot area, rises very quickly when the electron beam is turned on. It rises from 300 K to 2800 K in the first 5 ms. When the electron beam is turned off, the anode cools down rapidly from 3000 K in 20 ms. This suggests that if the tube operats in short pulse mode with a low duty cycle, the heat can dissipate very fast. Therefore, the allowed power during the pulse-on period can be significantly larger than that in the DC operating mode.

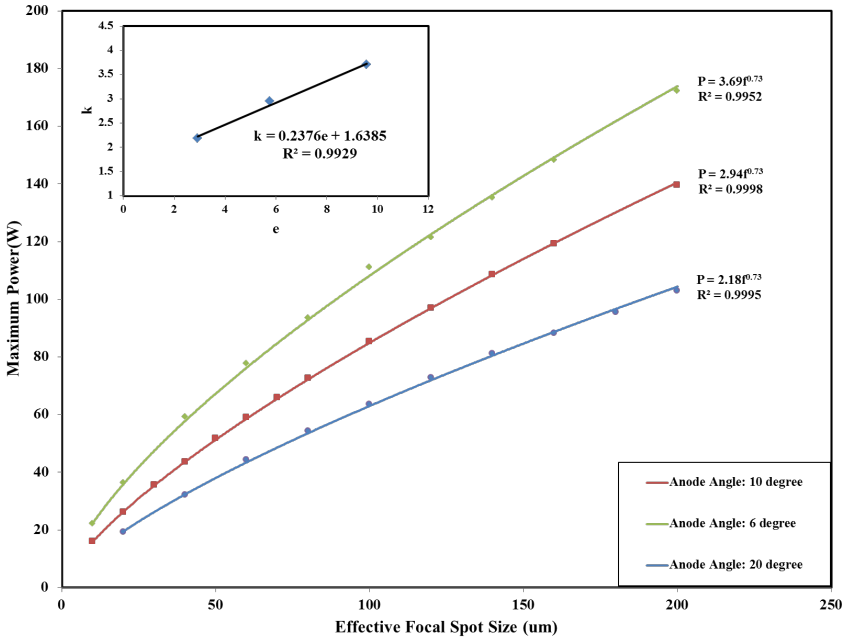

Figure 6.32: Maximum power of an x-ray tube running in DC mode as a function of effective focal spot size at 6°, 10°, and 20° anode angles. The maximum power in DC mode is a power function of effective focal spot size, $P = kf_s^{0.73}$, where the coefficient k is a linear function of e, $k = 0.24e + 1.64$. Simulated results suggest that the maximum power is related to the anode angle in DC operation mode; the smaller the anode angle, the higher power the x-ray tube can apply.

For pulse mode, the maximum allowed power is significantly higher than that in DC mode. The relationship between the maximum power in pulsed mode and the effective focal spot size is shown in Figure 6.34, for three different anode angles. In all three cases, it is found that P linearly increases with the effective focal spot size, f_s. Results show that the maximum power can be described by the simple relation:

$$P(W) = (\frac{0.20}{\sin\theta} + 0.35) f_s(\mu\text{m}) \tag{6.17}$$

It can be seen that at smaller anode angles, the anode can withstand higher power. For example, for 10° anode angle and 100 µm effective focal spot, CNT x-ray tubes can operate at 153 W with 10 ms temporal resolution, a factor of two higher than previously thought possible.[76] Experimentally, we have operated the CNT micro-CT system at 100 W for in-

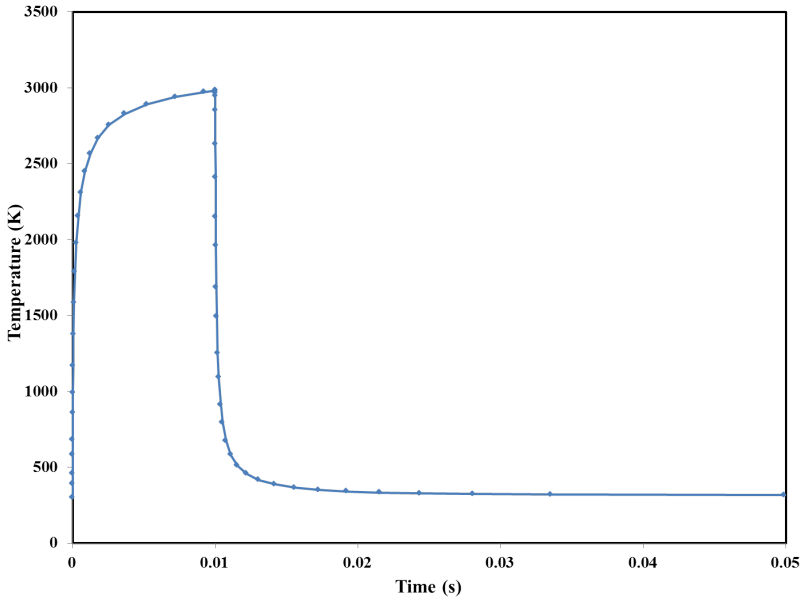

Figure 6.33: Maximum temperature over time in a 10 ms pulse. The temperature both rises and drops rapidly when the electron beam is turned on or off. This result suggests heat can be dissipated very quickly in pulsed mode with low duty cycle. Thus, the tube can be operated at a significantly higher power than that in DC mode.

vivo animal imaging for almost two years, without any anode thermal loading issues.[79, 45] Simulation results suggest it is possible to increase the x-ray tube power by another 50% without running into thermal loading issues.

6.4.5: Anode heat simulation for s-DBT and s-DCT systems

Thermal simulations were performed at various power levels for the s-DBT systems. The maximum stable power was determined by the heat load of the stationary anode. For the s-DBT system, the power was selected according to the expected operating conditions of the x-ray tube, up to 38 kVp effective anode voltage at various tube currents and pulse widths. The anode target was a tungsten block. The effective focal spot size was 0.6 mm $\times$ 0.6 mm FWHM.[47] The power density was distributed on the anode as a Gaussian function with the measured FWHM of the focal spot size. The temperature distribution on the whole anode

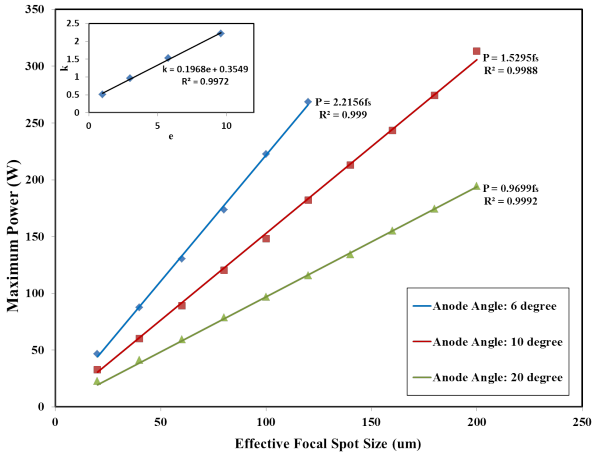

Figure 6.34: Maximum power of CNT micro-CT x-ray tube running in pulsed mode as a function of effective focal spot size, with anode angles at 6°, 10°, and 20°. Simulation results suggest the maximum power for pulsed mode linearly increases with focal spot size, and can be described by a simple scaling law.

Table 6.9: Simulated anode maximum temperature for 0.6 mm × 0.6 mm FWHM focal spot size at various conditions.

High voltage (kVp)	Tube current (mA)	Power (W)	Pulse width (ms)	Max temperature (K)
38	38	1444	183	3872
38	28	1064	250	2811
38	20	760	250	1962

structure was simulated for the targeted focal spot size.

For the s-DCT system, anode heat simulation is needed in order to design a new source array (Section 5.5). The targeted focal spot size is expected to be 0.6 mm × 0.6 mm, equivalent to current commercial systems. The anode was made of tungsten. Because the heat distribution is only determined by the anode material, focal spot size, and pulse width, the same conclusions can be applied to the s-DCT system.

Table 6.9 summarizes the maximum temperature for a 0.6 mm × 0.6 mm focal spot (FWHM) on a tungsten anode, at various conditions. Figure 6.35 shows the time profile of the maximum temperature for the conditions listed in Table 6.9.

The temperature profiles show a fast increase in the temperature within the first 10 ms.

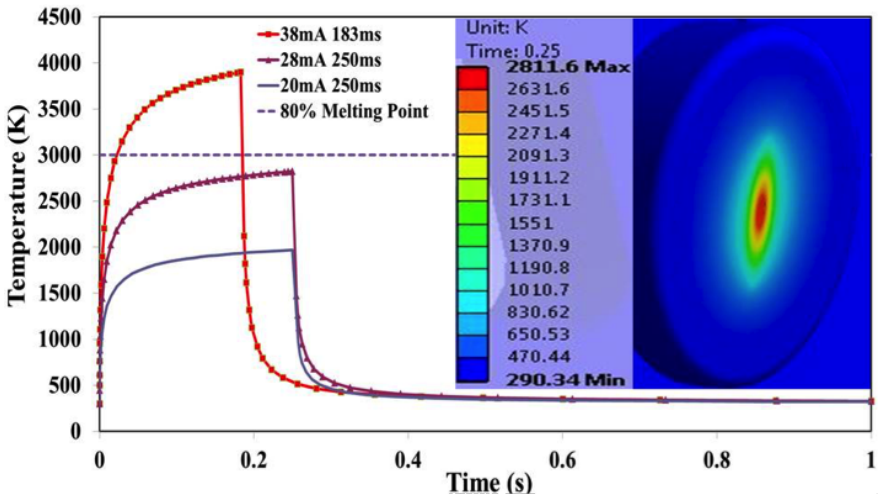

Figure 6.35: The simulated temperature profile over time at the center of the focal spot during a single x-ray exposure at three different power levels. The dashed horizontal line indicates 80% of the melting temperature of tungsten. The insert shows the temperature distribution on the anode surface for the 38 kVp, 28 mA, 250 ms exposure.

This is because on this time scale, the heat does not transfer far. Nearly all of the kinetic energy of the incident electrons transfers to heat in the finite volume near the focal spot region. The heat capacity of tungsten increases with temperature, meaning more energy is needed to increase the temperature of the same volume by 1 K. Therefore, the rate of temperature increase slows down. Meanwhile, the heat transfers to the surrounding material, bringing out a large portion of the incident energy. As the temperature goes up, the energy radiating out from the hot surface increases as well. This radiation is mainly in the form of infrared, with the radiation power proportional to T^4. Together, all these factors bring the system close to a quasi-equilibrium state. The smaller the incident power, the faster this quasi-equilibrium state is reached.

The transient temperature drops very quickly to the base value after the exposure, due to heat transfer and thermal radiation. The falling edge of the temperature profile has a similar time scale to the rising portion. In about 10 ms, the temperature drops more than 80%.

Under condition II (1064 W, 38kVp, 28 mA, and 250 ms pulse width), the highest anode

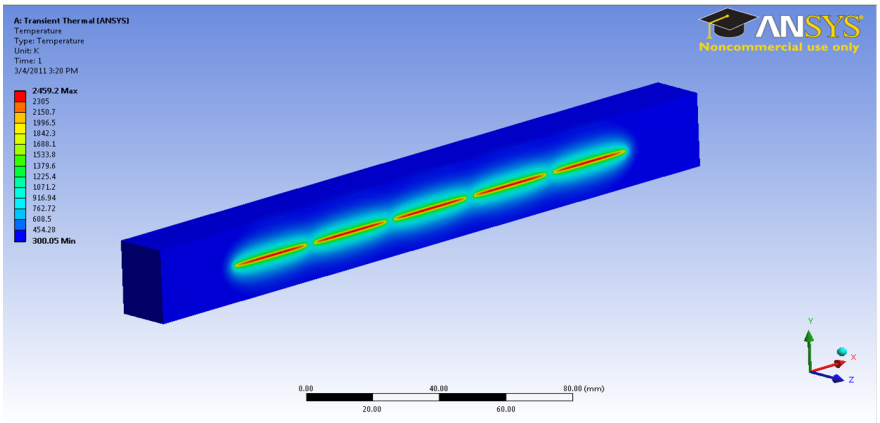

Figure 6.36: Anode temperature distribution for MRT system operated at 160 kVp, 35 mA, 1 s pulse width.

temperature was found to be 2811 K, which is less than 80% of the melting temperature of tungsten. Therefore, the x-ray source can be safely operated at a power level of approximately 1.1 kW for an effective focal spot of 0.6 mm $\times$ 0.6 mm, for both s-DBT and s-DCT systems.

Based on the results of simulation, for the next-generation s-DCT source array, which has a target focal spot size of 0.6 mm $\times$ 0.6 mm, the maximum tube current at different kVp level can be estimated. Table 6.10 lists the estimated tube current from 80 kVp to 120 kVp.

Table 6.10: Estimation of s-DCT operating conditions based on anode heat load simulation.

High voltage (kVp)	Tube current (mA)
80	13.8
100	11
120	9.2

6.4.6: Anode heat simulation for MRT system

Similar anode heat simulations were performed for the CNT based MRT system. The anode of the MRT system is made of a 222 mm $\times$ 26 mm $\times$ 17 mm molybdenum block with

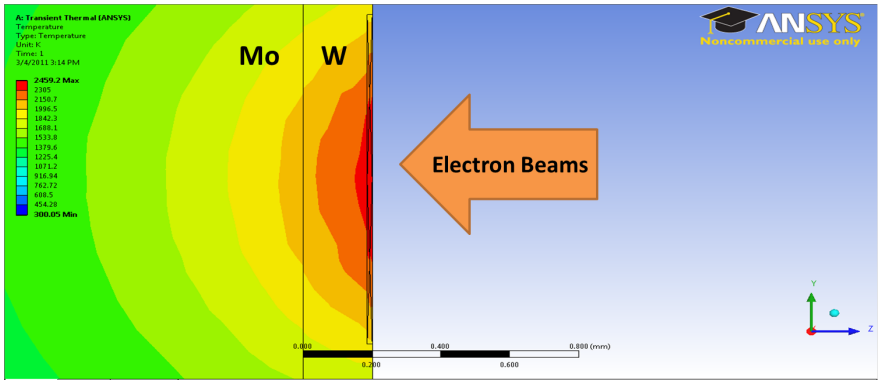

Figure 6.37: Anode temperature distribution in the cross-section for the MRT system operated at 160 kVp, 35 mA, 1 s pulse width.

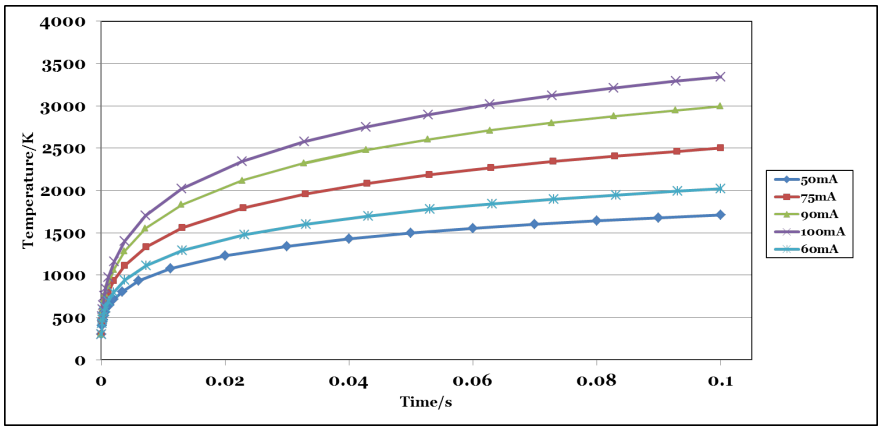

Figure 6.38: Anode maximum temperature profile for the MRT system at various tube currents.

a 200 µm tungsten coating on top. Molybdenum is used to increase the heat dissipation capability of the anode. The focal line of the MRT system consists of five focal spots, 30 mm × 200 µm each. Typical operating conditions of the MRT system is 160 kVp, 35 mA anode current, and 5% duty cycle.[48]

The temperature distributions on the anode surface and the cross-section at 160 kVp, 35 mA, and 1 s pulse width, are shown in Figure 6.36 and Figure 6.37, respectively. The maximum temperature at various operating conditions are plotted in Figure 6.38.

6.4.7: Conclusions

A numerical anode heat simulation model was built using a finite element analysis method. It was found that the anode thermal limit is determined by the incident power at a given focal spot size, anode material, and pulse width. CNT x-ray sources can generate x-rays in pulsed mode, which increases the maximum power compared to conventional x-ray tubes operating in DC mode.

The results of the anode heat simulations have been used to help design CNT x-ray sources and operation protocols. Some of the results from this section can be used qualitatively to estimate the tube thermal limit, or to evaluate the imaging protocol. However, detailed simulations need to be performed to quantitatively analyze the anode heat load issue.

For the next generation s-DCT source array (discussed in Section 5.5), the permitted power for a 0.6 mm $\times$ 0.6 mm (FWHM) focal spot is around 1.1 kW. If the s-DCT operats at 120 kVp, as in conventional DCTs, the tube current could reach 9 mA.

Section 6.5: CNT Source Array Geometry Calibration

6.5.1: Introduction

Knowing the positions of the focal spots is crucial for tomosynthesis reconstruction. The relative positions of focal spots to the detector is determined using a geometry calibration procedure. The most commonly adopted method is acquiring images of fiduciary markers, which are typically made of high attenuating materials. Based on the position and/or shape of the markers in the images, the focal spot position is calculated.[80]

In this section, a simple geometry calibration method using an in-house geometry calibration phantom will be introduced. Methods to determine and optimize the position of the focal spot will be covered. Some results will be provided.

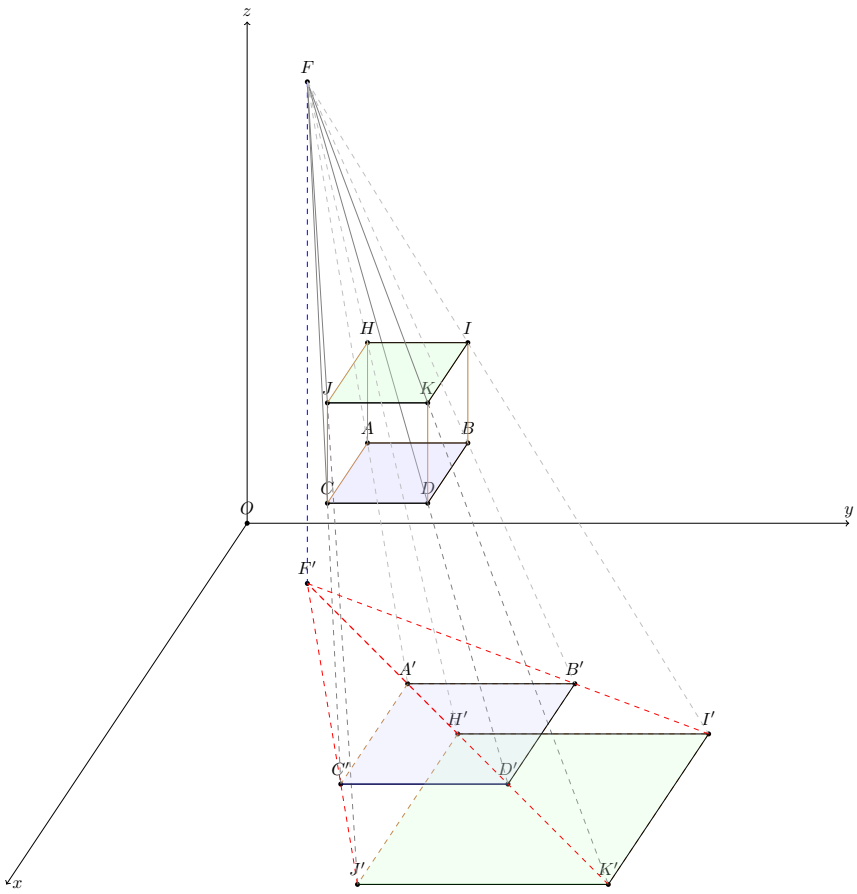

Figure 6.39: Illustration of the geometry calibration method. F denotes the position of the focal spot. Metal beads (ideal point) A, B, C, D, H, I, J, and K are placed in the image field, and projected images of the beads are at A', B', C', D', H', I', J', and K', respectively. Plane $ABCD \parallel HIJK$.

6.5.2: Geometry calibration method

The geometry calibration method is illustrated in Figure 6.39. In the coordinate system $x - y - z$ set up on the detector, the detector plane is the $x - O - y$ plane. F denotes the position of the focal spot. Metal beads (ideal point) A, B, C, D, H, I, J, and K are placed in the image field, and projected image of the beads at A', B', C', D', H', I', J', and K', respectively. Plane $ABCD \parallel HIJK \parallel x - O - y$. JC, KD, IB, and HA are all perpendicular ($\perp$) to the $x - O - y$ plane. F' is the projected point of focal spot F on the $x - O - y$ plane. Clearly, the x and y coordinates of F' are the same for F. The position of

F' is determined by finding the intersection point of line $J'C'$, $K'D'$, $I'B'$, and $H'A'$.

The z coordinates of the focal spot F, can be found by:

$$\frac{z}{z_C} = \frac{C'D'}{CD} = M_1 \tag{6.18}$$

$$\frac{z}{z_J} = \frac{J'K'}{JK} = M_2 \tag{6.19}$$

Where the M_1 and M_2 are the magnification factors for the top and bottom plane of the phantom. If we know the distance between the two planes in the phantom, d, then the z of focal spot F can be determined as:

$$z = \frac{M_1 \cdot M_2}{|M_1 - M_2|} \cdot d \tag{6.20}$$

Therefore, the x, y, and z coordinates of the focal spot are determined.

In this method, it is important that the prerequisites of planes $ABCD$ and $HIJK$ being parallel to plane $x - O - y$ are satisfied. The flat panel detector can be seen as a good flat surface. A geometry calibration phantom that can be placed parallel to the detector plane should suffice for the calibration. Based on the principles of geometry calibration discussed here, a phantom was constructed and tested.

6.5.3: Geometry calibration phantom

An in-house geometry calibration phantom was constructed. The phantom, as shown in Figure 6.40, consists of two layers acrylic, eight 5 mm diameter stainless steel beads, and four 35 mm long tungsten bars. The two sheets were connected using four tungsten bars of the same length, so the two layers are parallel and the tungsten bars are perpendicular to the acrylic. Four beads were embedded in each layer.

During the geometry calibration procedure, the phantom was placed on the detector. Since both the detector and phantom were flat, the requirement of the phantom to be

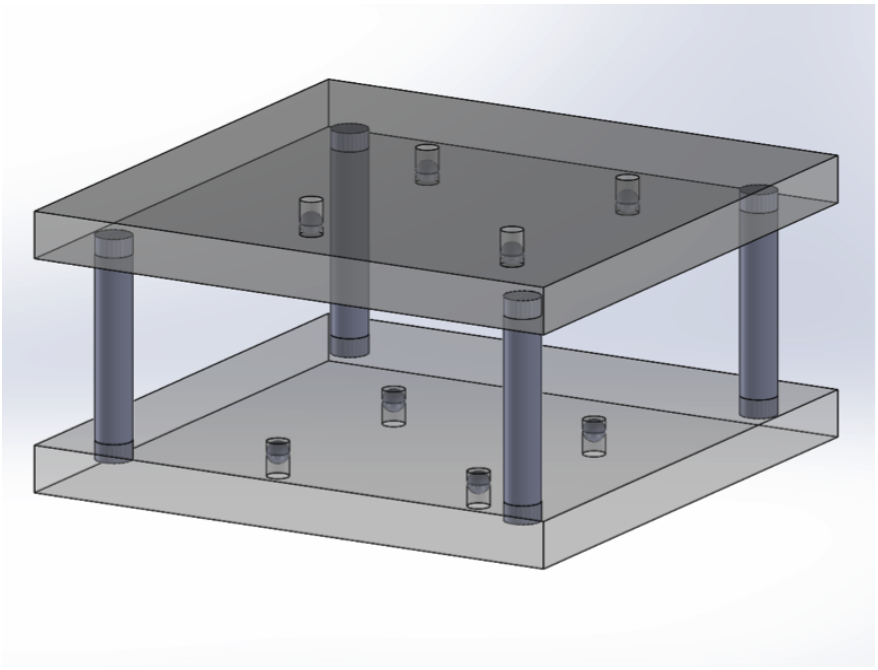

Figure 6.40: CAD drawing of the geometry calibration phantom. The phantom has two acrylic sheets parallel to each other. Four tungsten bars were placed perpendicular to the acrylic layer. Each acrylic plate had four metal beads embedded inside.

parallel to the detector was satisfied. X-ray images of the calibration phantom were acquired. An example image is shown in Figure 6.41. The image went through standard gain and offset corrections. A Matlab program using feature recognition was developed to identify the beads and vertical bars in the projection images. The distances between metal beads were measured. The magnification factors M_1 and M_2 were calculated using the measured distances and actual distances between beads. Based on the measurements, the z coordinate of the focal spot was calculated.

The centerline of the four projected tungsten bars were found, and the intersection point of them gave the x and y coordinates of the focal spot. However, due to the uncertainties in finding the centerline of the bars and the finite size of the focal spot,[6] *the four centerlines do not guarantee intersection at one point.* The four lines could intersect at up to 6 different points. Therefore, we need to estimate the position of the intersection point based on the

[6]Due to the uncertainties in the edge detection algorithm. The identified centerline can have errors on the orientation of the line.

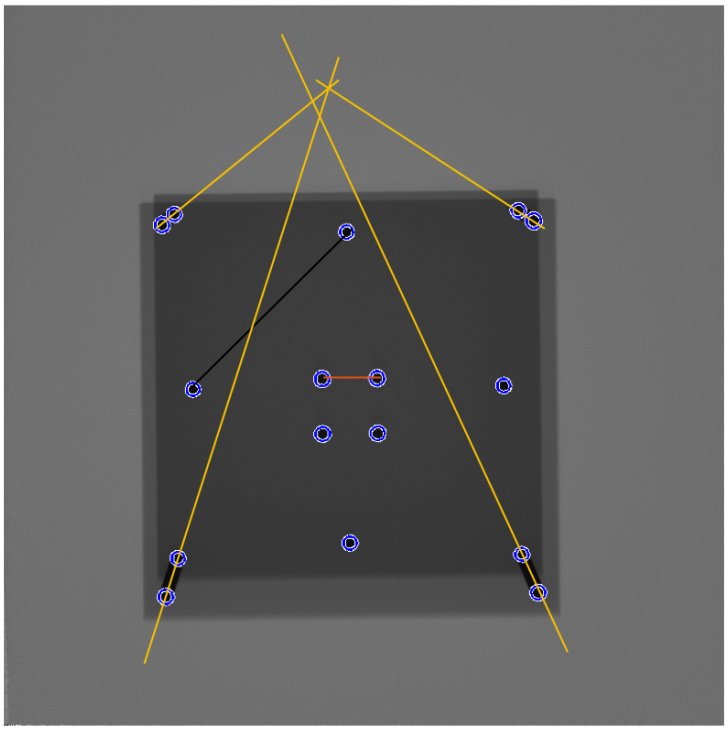

Figure 6.41: An example projection image of the geometry calibration phantom. Yellow lines are the centerlines of the four vertical tungsten bars. The intersection point of these four lines gives the x, and y coordinates of the focal spot. The distance between metal beads can be used to calculate the magnification factor M_1 and M_2 for the top and bottom layer of the phantom. Thus, the z coordinate of the focal spot can be calculated.

multiple intersections. One simple way to estimate the x and y coordinates is using the average x and y coordinates of all intersection points. However, this straightforward method does not always provide the best estimation of x and y.

Why is the average of the intersections not the best?

The main source of error causing multiple intersections is the uncertainty in determining the orientation of the centerlines. Figure 6.42 illustrates one situation.[7] Centerlines l_1, l_2, l_3,

[7]This situation happens when the x-ray source is above or close to one or more vertical bars. Since the source array contains multiple x-ray sources, it is hard to avoid this situation in geometry calibration. One example is shown in Figure 6.41, the focal spot is close to the top left and top right bars, causing the projected bars to have shorter lengths, which increases the uncertainties in determining the orientations of these two centerlines.

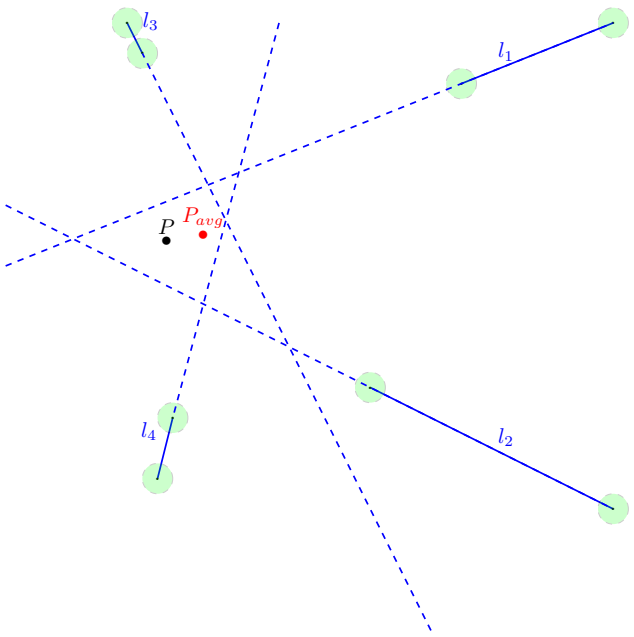

Figure 6.42: Illustration of the source of error using average coordinates of all intersection points to estimate the focal spot's x and y coordinates.

and l_4 intersect at 6 points, and P_{avg} is the estimated location calculated using the averaged x and y of all six points. Each centerline is determined by the two end points, assuming the same uncertainty in determining each end point, as indicated by the green circle around each end point. It is clear that the shorter the length of the bar, the larger error on its orientation. Therefore, one would expect the best estimate of the intersection point P to be closer to the lines with a smaller error in orientation, thus further away from the shorter centerlines.

If two centerlines have a very small angle in between, using the average coordinates would result in a large error when estimating the x and y coordinates of the focal spot.[8] As illustrated in Figure 6.43, the intersection point of l_1 and l_2 is far away from the other intersection points due to the small angle between l_1 and l_2. The estimate of the projected focal spot using averaged coordinates of all the intersection points P_{avg} is close to the intersection with larg error, degrading the accuracy of geometry calibration.

[8]This situation typically occurs with focal spots near the two ends of the source array, where the projection angle is small for all vertical bars.

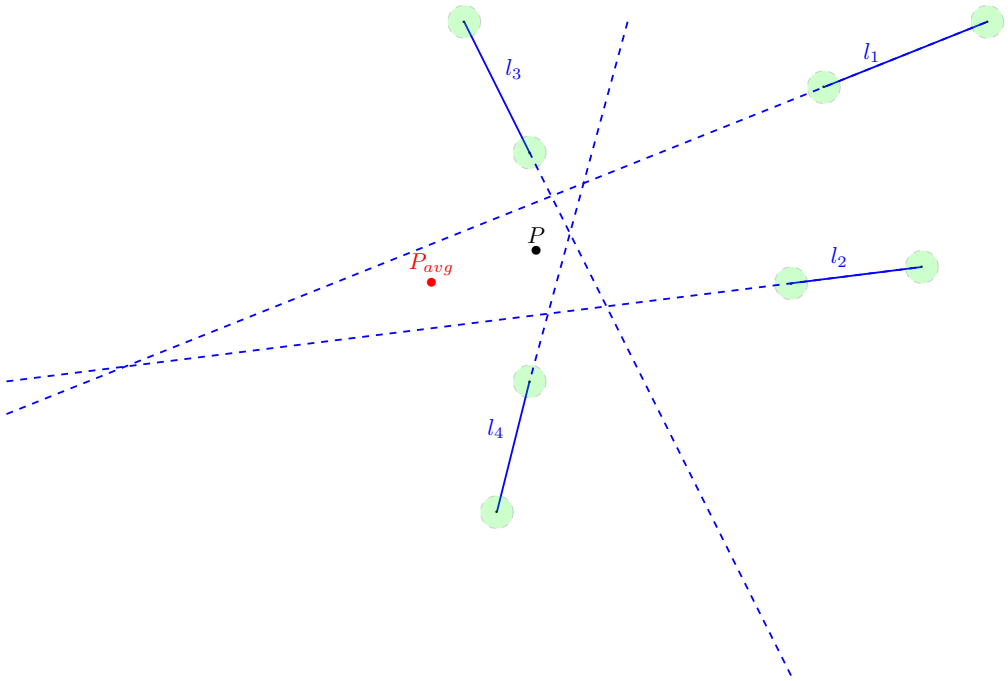

Figure 6.43: Illustration of the source of error in an extreme case using average coordinates of all intersection points as focal spot x and y positions. The intersection point of l_1 and l_2 is far away from other intersection points due to the small angle between l_1 and l_2. The averaged point, P_{avg}, produces a large error.

6.5.4: A statistical model based optimization method

Since there is always uncertainty when identifying features in an image, another way to improve the accuracy of the geometry calibration procedure is to minimize errors when estimating the location of intersections. A statistical model-based optimization method was investigated for this purpose.

$A(x_1, y_1)$ and $B(x_2, y_2)$ are the two points used to determine one line in this geometry calibration procedure. The point $P(a, b)$ is the intersection point of all the lines. In principle, P, A and B should be on the same line, therefore we have:

$$(b - y_1) \cdot (x_2 - x_1) = (a - x_1) \cdot (y_2 - y_1) \tag{6.21}$$

The position of A and B can be measured, then this equation can be written as a linear

equation to solve the unknown coordinates of intersection point P as:

$$a \cdot (y_1 - y_2) + b \cdot (x_2 - x_1) = x_2 y_1 - x_1 y_2 \tag{6.22}$$

Ideally, two lines would be enough to solve the coordinates of the intersection point P. Due to the measurement error in determining positions of A and B, the equation above is not always true, and there will be a error term ϵ.

$$a \cdot (y_1 - y_2) + b \cdot (x_2 - x_1) = x_2 y_1 - x_1 y_2 + \epsilon_1 \tag{6.23}$$

Two equations would not be enough to determine the coordinates of P, as the error terms ϵ_1 and ϵ_2 would be unknown.

For a given image that we used to do geometry calibration, there are n lines used to determine the intersection point P. Writing n linear equations, gives:

$$\begin{bmatrix} y_1^{(1)} - y_2^{(1)} & x_2^{(1)} - x_1^{(1)} \\ \vdots & \vdots \\ y_1^{(k)} - y_2^{(k)} & x_2^{(k)} - x_1^{(k)} \\ \vdots & \vdots \\ y_1^{(n)} - y_2^{(n)} & x_2^{(n)} - x_1^{(n)} \end{bmatrix} \cdot \begin{bmatrix} a \\ b \end{bmatrix} = \begin{bmatrix} y_1^{(1)} x_2^{(1)} - y_2^{(1)} x_1^{(1)} \\ \vdots \\ y_1^{(k)} x_2^{(k)} - y_2^{(k)} x_1^{(k)} \\ \vdots \\ y_1^{(n)} x_2^{(n)} - y_2^{(n)} x_1^{(n)} \end{bmatrix} + \begin{bmatrix} \epsilon_1 \\ \vdots \\ \epsilon_k \\ \vdots \\ \epsilon_n \end{bmatrix} \tag{6.24}$$

where $x_1^{(k)}$ and $y_1^{(k)}$ are the x and y coordinates of the first point in the k-th line. We can rewrite the equation array in matrix form:

$$\mathbf{X} \cdot \beta = \mathbf{Y} + \epsilon \tag{6.25}$$

Due to the measurement error, the equation array above generally does not have a solution.

The aim is to find the best estimate of intersection point $P(a, b)$ (vector β). By using a

linear regression method, we can find the vector β such that the error is minimized.

$$\underset{\beta}{\text{minimize:}} \sum_{i=1}^{n} \epsilon_i^2 = \begin{bmatrix} \epsilon_1 & \epsilon_2 & \dots & \epsilon_n \end{bmatrix} \cdot \begin{bmatrix} \epsilon_1 \\ \epsilon_2 \\ \vdots \\ \epsilon_n \end{bmatrix} = \epsilon'\epsilon \tag{6.26}$$

which is equivalent to:

$$\underset{\beta}{\text{minimize:}}\ \epsilon'\epsilon = (\mathbf{X}\beta - \mathbf{Y})'(\mathbf{X}\beta - \mathbf{Y}) \tag{6.27}$$

Take the first derivative with respect to β

$$\frac{\mathrm{d}}{\mathrm{d}\beta}(\mathbf{X}\beta - \mathbf{Y})'(\mathbf{X}\beta - \mathbf{Y}) = \mathbf{0} \tag{6.28}$$

$$\mathbf{X}'\mathbf{X}\beta = \mathbf{X}'\mathbf{Y} \tag{6.29}$$

Solve the above linear equation array to get vector β, then the best estimate of the intersection point $P(a, b)$ is solved.

The physical meaning of the optimization method

The purpose of the optimization method above is to minimize the total error. The error term is minimized to:

$$\begin{aligned} \epsilon'\epsilon &= \sum_{i=1}^{n} \epsilon_i^2 && (6.30) \\ &= \sum_{i=1}^{n} \left[\left((x_2^{(i)} - x_1^{(i)}) \cdot b - \left(y_2^{(i)} - y_1^{(i)} \right) \cdot a \right) - (x_2^{(i)} y_1^{(i)} - x_1^{(i)} y_2^{(i)}) \right]^2 && (6.31) \\ &= \sum_{i=1}^{n} l_i^2 h_i^2 && (6.32) \end{aligned}$$

where l_i is the length of i-th line, and h_i is the distance between the estimate of intersection point $P(a, b)$ and the i-th line. Equation 6.32 shows the physical meaning of this minimizing

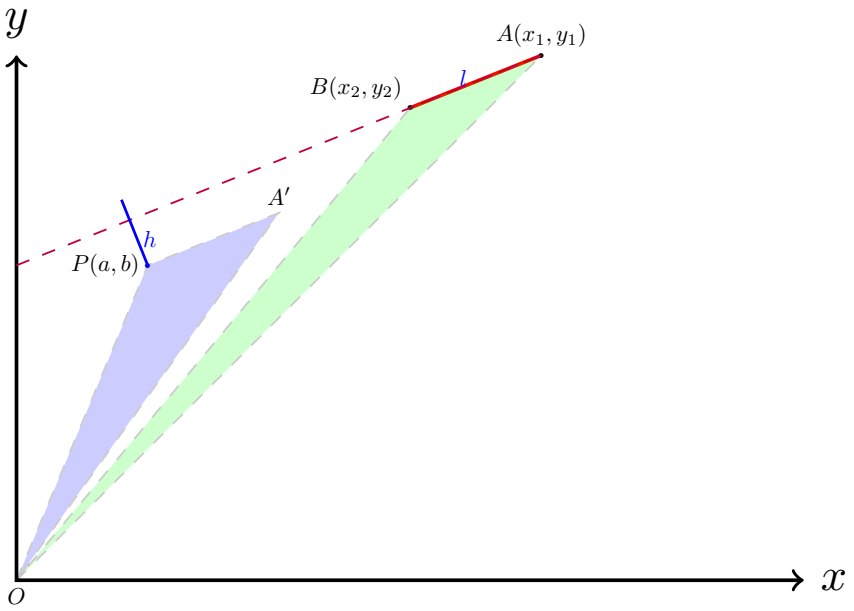

Figure 6.44: Illustration of the physical meaning of the optimization method.

method, as illustrated in Figure 6.44. Let points $A(x_1, y_1)$ and $B(x_2, y_2)$ be the two end points of a bar, the length of AB is l. The first term in Equation 6.31 for $n = 1$ is:

$$(x_2 - x_1)b - (y_2 - y_1)a = 2S_{\triangle OA'P} \tag{6.33}$$

where vector $A'P$ is parallel to vector AB. Similarly, the second term in Equation 6.31 is:

$$x_2y_1 - x_1y_2 = 2S_{\triangle OAB} \tag{6.34}$$

So Equation 6.31 is:

$$[(x_2 - x_1)b - (y_2 - y_1)a - (x_2y_1 - x_1y_2)]^2 = 4(S_{\triangle OA'P} - S_{\triangle OA'P})^2 \tag{6.35}$$

$$= 4 \cdot (\frac{1}{2}l \cdot h)^2 = l^2h^2 \tag{6.36}$$

Therefore, the minimization of the error term $\epsilon'\epsilon$ is equivalent to minimizing $\sum_{i=1}^{n} l_i^2 h_i^2$,

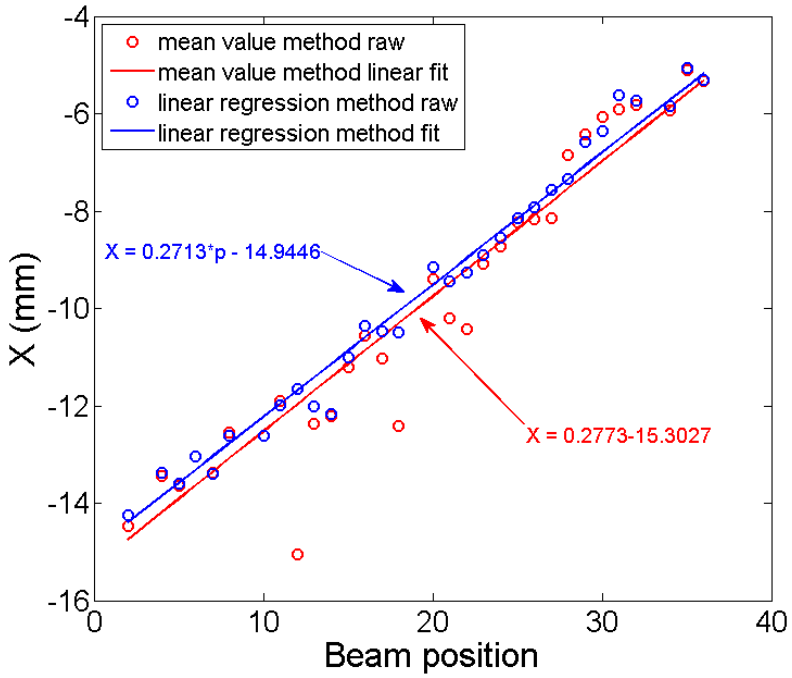

Figure 6.45: The geometry calibration results of the x coordinates of focal spots in the s-DCT source array, using mean value method and optimization method. The optimization method shows better calibration accuracy.

where h_i is a weighting factor. As shown in Figure 6.42, for the centerline with shorter length we know the orientation error is large, thus the estimate of focal spot should be further away from the centerline (larger h_i), and vice versa. For the situation where two centerlines have a small angle (Figure 6.43), moving away the intersection of these two lines dramatically decreases the error term.

Using the optimization method was mainly discussed in the context of minimizing the error when estimating the x and y coordinates of the focal spot. Similar models can be applied to estimate the z coordinate of the focal spot, as well.

6.5.5: Comparison of the two calibration methods

Geometry calibration results using the optimization method were compared to results using the average value method, as shown in Figures 6.45 and 6.46. Figure 6.45 shows the

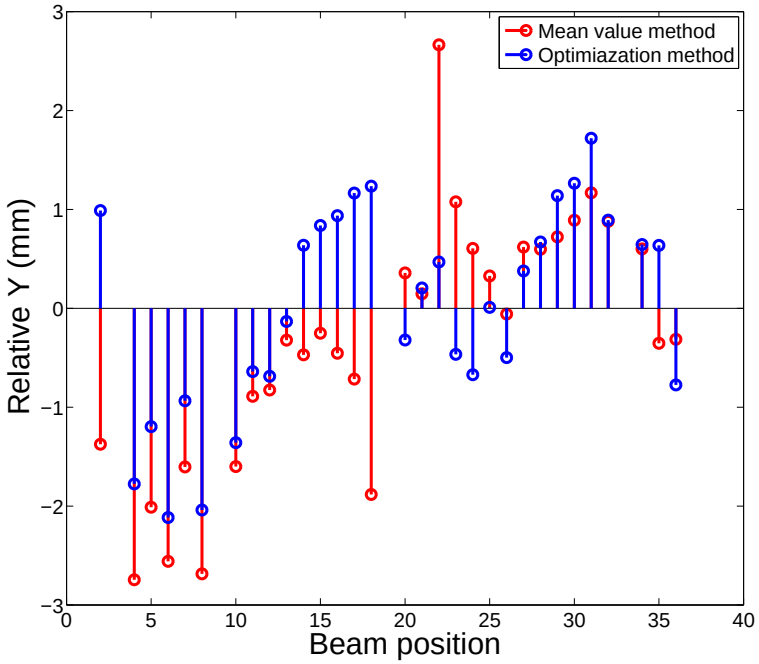

Figure 6.46: Comparison of the geometry calibration results of the y coordinates between the mean value method and optimization method. The optimization method shows better calibration accuracy.

comparison along the x direction, while Figure 6.46 shows the comparison along y direction. The raw calibration results are fitted to a line because the source array was designed and manufactured in a linear pattern. Since the source array is placed parallel to the y direction, the relative y value instead of the absolute y value were compared. The results using the optimization method shows better accuracy for the calibration of both x and y coordinates of the focal spots in s-DCT source array.

6.5.6: Discussion

In this section, we introduced an in-house geometry calibration procedure for the s-DCT system. The procedure utilizes a simple geometry calibration phantom and a statistical model based optimization method to analyze the data. Reconstructed images using the recovered coordinates of the focal spots using this procedure produces good image quality

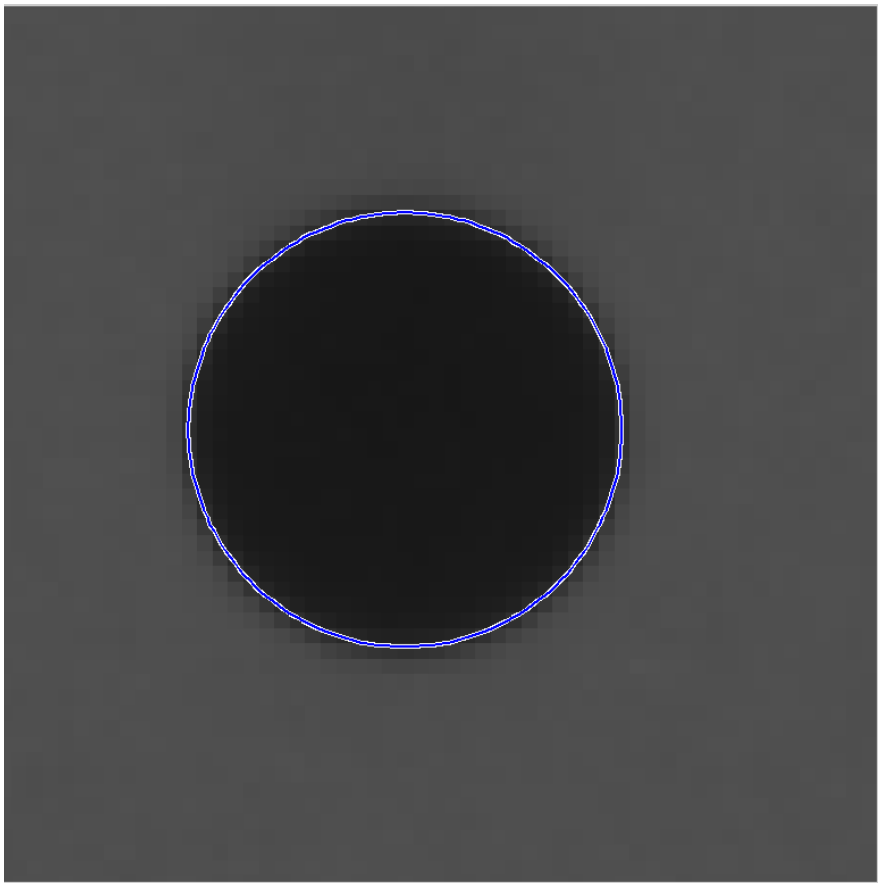

Figure 6.47: An image of a metal bead used in the geometry calibration procedure. The blurred edge of the bead increases uncertainty in edge detection and feature recognition of the image.

and spatial resolution, as well as a lack of image artifacts, suggesting the procedure can provide an accurate geometry calibration for the s-DCT system. This procedure can be also applied to other imaging systems, such as s-DBT system.

The main source of error of this procedure comes from the uncertainty in identifying features from the projection images. Due to the finite size of the focal spot, instead of ideal point, and the fact that metal beads can not block all x-rays, the image of the beads typically have a blurred edge(Figure 6.47). The blurred edge increases uncertainty in finding the edges or features of the fiduciary markers in the image. However, it is crucial to find the center of the bead (or one focus of the ellipse) in the geometry calibration procedure.[81] A high accuracy algorithm to identify features and edges from the image is desired.

The introduced in this section gives a more accurate estimation of the focal spot positions. This method provides a better estimate *statistically*, so it does not mean it is the best estimate every time.

CHAPTER 7: Evaluation of imaging geometries for the s-DCT system

Section 7.1: Overview

The feasibility of *stationary* digital chest tomosynthesis (s-DCT) using a distributed carbon nanotube x-ray source array was demonstrated in Chapter 5. The technology has the potential to increase the imaging resolution and speed by eliminating source motion. In addition, the flexibility in the spatial configuration of the individual sources allows new tomosynthesis imaging geometries beyond the linear scanning mode used in conventional systems. In this chapter, we investigate the effects of tomosynthesis imaging geometry on the image quality. The study was performed using the bench-top s-DCT prototype. System MTF and ASF were used as a quantitative measurement of the in-plane and in-depth resolution, respectively.

In this chapter, imaging geometries with the x-ray sources arranged in linear, square, rectangular, and circular configurations were investigated using comparable imaging doses. Anthropomorphic chest phantom images were acquired and reconstructed for image quality assessment. It was found that wider angular coverage resulted in better in-depth resolution, while the angular span had little impact on the in-plane resolution in the linear geometry. Non-linear imaging geometry lead to more isotropic in-plane resolution and better in-depth resolution compared to a linear imaging geometry with comparable angular coverage.

Section 7.2: Purpose

In Chapter 5, we have demonstrated the feasibility of a CNT-based s-DCT system using the CNT source array. The CNT source array has been shown to deliver sufficient x-ray output for chest tomosynthesis applications.

The flexibility of the CNT source array also allows novel imaging configurations that conventional DCT systems cannot easily achieve. In current DCT systems, one x-ray source is moved in a linear path to acquire projection images.[1, 4] While the imaging configuration has been optimized for linear imaging,[5, 71, 30] the impact of non-linear imaging geometries on image quality has not been investigated, except in a few studies, due to the difficulties of managing tube momentum of a moving X-ray source.[82–84]

The purpose of this study is to investigate the relationship between source configuration and the tomosynthesis image quality using an s-DCT system.

Section 7.3: Methods

The same bench-top s-DCT system introduced in Chapter 5 was used for this study. Images were acquired using different x-ray source configurations. The system resolution, characterized by reconstructed tomosynthesis modulation transfer function (MTF) and artifact spread function (ASF), were measured for all imaging geometry configurations. Anthropomorphic chest phantom images were acquired and reconstructed for quality assessment.

7.3.1: System Descriptions

The bench-top s-DCT, as shown in Figure 7.1, consists of a CNT source array and a flat panel detector mounted on a translation stage. Only a subset of 75 focal spots in the source array were used to acquire projection images. The same CsI based detector (Model DRX-1C) with 139µm × 139µm pixel size and 35cm × 43cm field of view was used. The source-to-detector distance was 1100 mm.

7.3.2: Imaging Geometries

Since the source array used in this study has a relatively short tube length, the detector and phantom were mounted on a stage that could be translated simultaneously to simulate

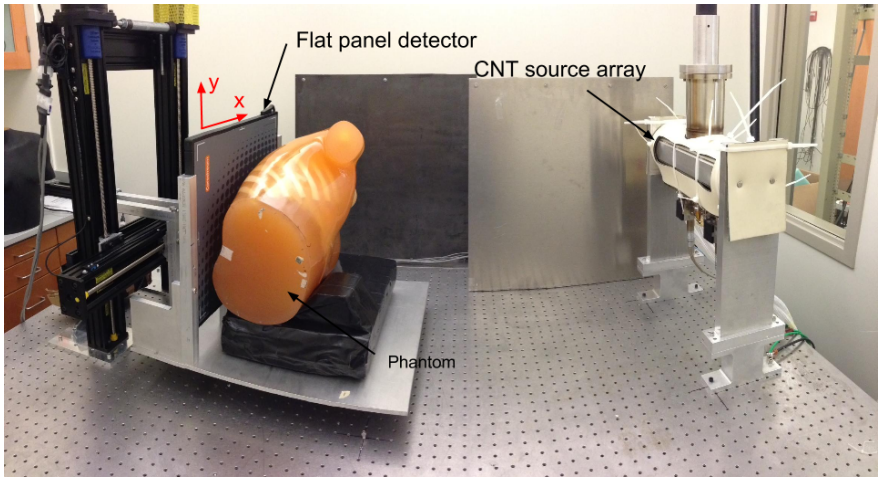

Figure 7.1: The s-DCT system consists a linear CNT source array, a flat panel detector, a phantom and translation stages. The detector and phantom can be simultaneously translated to simulate various imaging geometries.

various imaging geometries. The SID was kept at 1100 mm. By translating the detector and phantom along both the x direction and y direction, an effective source matrix relative to the detector was emulated. Subsets of projection images from this effective source matrix were selected to simulate all imaging geometries. Figure 7.2 shows the imaging geometries studied. The effective source array of each imaging geometry was centered at the detector center. By translating the detector and phantom along the scanning direction (x-direction), three 1D linear geometries with different angular spans of 11.6°, 23°, and 34° were created. Each had 29 projections which were acquired at 80 kVp and 0.5 mAs per projection.

Translation of the detector perpendicular to the scanning direction (y-direction) allowed simulation of square, rectangular, and circular imaging geometries. All three 2D source array imaging geometries included 32 projections. Each projection image was acquired at 80 kVp and 0.5 mAs. All 6 geometries studied had comparable total imaging dose. The square geometry had a length of 192 mm and 10° angular coverage on each side. The rectangular geometry had a length of 256 mm (13.3° angular coverage) and a width of 192 mm (10° coverage) along x and y direction respectively. The circular geometry had a radius of 192 mm and 10° angular coverage.

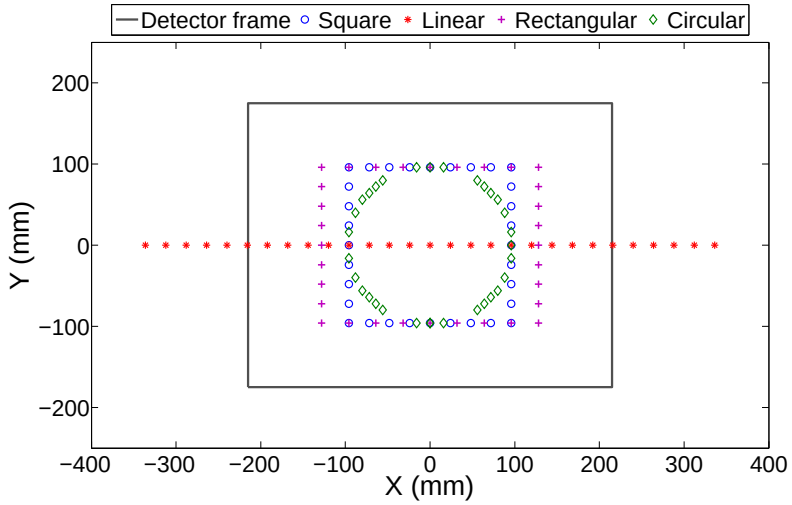

Figure 7.2: Imaging geometry configuration studied. All imaging configurations are using same SID of 1100 mm. A linear imaging geometry with angular span of 11.6°, 23°,and 34°, a square geometry centered with detector center and 10° angular span on each side, a rectangular geometry with 13.3° and 10° angular coverage along x and y direction, and a circular geometry with 10° angular coverage are studied. The x-direction is along the source array scanning direction, which is also corresponding to the phantom spine direction, while the y-direction is defined as perpendicular to the scanning direction, as noted in both figures.

7.3.3: Image Analysis

System MTF and ASF were used to quantify the tomosynthesis in-plane and in-depth (z-axis) resolutions. They were measured using a 100 µm diameter tungsten cross-wire phantom. Projection images of the phantom were acquired and reconstructed into tomosynthesis slices using commercial software from Real Time Tomography (Villanova, PA). The data set was reconstructed with 1 mm spacing.

7.3.4: Anthropomorphic Phantom Images

Projection images of an anthropomorphic chest phantom (Kyoto Kagaku Co. Ltd., Kyoto, Japan) were acquired and reconstructed into tomosynthesis slices for all the imaging geometries studied. The phantom was positioned as shown in Figure 7.1, with spine direction aligned along the source array scanning direction. The projection images were acquired at

Table 7.1: MTFs and FWHM of ASF measurements for linear imaging geometries with angular coverage varying form 11.6° to 34°.

Angular Span	10% of MTF_x [cycles/mm]	10% of MTF_y [cycles/mm]	FWHM of ASF [mm]
11.6°	1.7	3.4	9.5
23°	1.6	3.2	5.8
34°	1.5	3.2	5.2

80 kVp and 0.5 mAs per projection.

Section 7.4: Results

7.4.1: System MTF and ASF for All Imaging Geometries

Table 7.1 lists the measured system MTFs (in both x and y directions) and the FWHM of the ASF for all linear imaging geometries. This particular source array has an elongated focal spot size along the scanning direction (x-direction), which led to asymmetric MTFs. The smaller focal spot size in the y direction results in better in-plane resolution of 3.4 cycles/mm. As the angular coverage increased from 11.6° to 34°, the in-plane resolution remained essentially the same in both directions, with 1.6 cycles/mm in the x-direction and 3.2 cycles/mm in the y direction. However, as the angular coverage increases, the in-depth resolution improves significantly from 9.3 mm to 5.1 mm. These trends agree with previous studies on imaging configurations for linear tomosynthesis. [5, 71, 30, 70]

Table 7.2 displays the MTFs and FWHM of ASF for the square, rectangular, and circular imaging geometries. The non-linear imaging geometries gave more symmetric MTFs measured as 2.5 cycles/mm in the x-direction and 3.0 cycles/mm in the y direction. The out-of-plane artifacts spread in both x and y directions in non-linear imaging geometries. Therefore, the ASF was measured in both directions. For symmetric geometries, such as square and circular, isotropic ASFs were found. The in-depth resolution for square geometry

Table 7.2: MTFs and FWHM of ASF measurements for non-linear imaging geometries.

Imaging Geometry	10% of MTF_x [cycles/mm]	10% of MTF_y [cycles/mm]	FWHM of ASF [mm]
Square - 10°	2.5	3.0	5.6
Rectangular	2.5	2.9	4.9
Circular - 10°	2.5	2.9	6.35

was found to be better than circular due to the larger angular coverage of sources located at the corners of the square.

7.4.2: Anthropomorphic phantom Imaging

Projections images were reconstructed into tomosynthesis slices with 4 mm spacing. Figure 7.3 shows tomosynthesis slices reconstructed from linear imaging geometries with 11.6° and 34° angular coverage. Both images clearly show multiple generations of airways and detailed vascular structures inside the phantom. The slice with larger angular coverage shows less out-of-plane artifacts of the ribs and other structures.

Figure 7.4 compares the linear imaging geometry with 11.6° angular coverage and the square imaging geometry with similar 10° angular coverage. The images reconstructed from the square imaging geometry show more fine structures in the x direction than the linear imaging geometry. This is because the square geometry yields more isotropic MTFs and better in-plane resolution in the x-direction, as shown in table 7.2. The visibility of the out-of-plane ribs was also reduced due to better in-depth resolution.

Section 7.5: Discussion

The CNT tube operated reliably with consistent source-to-source output. System MTFs and ASF measurements show that a wider angular coverage improves the system in-depth resolution, but has little impact on the in-plane resolution in the linear imaging geometry.

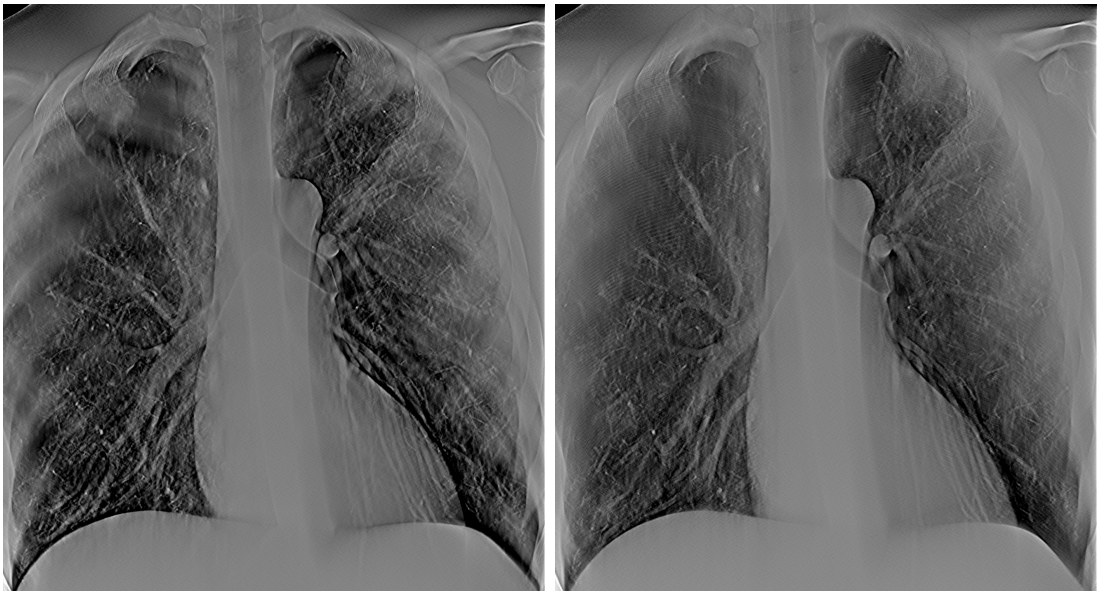

(a) linear 11.6° (b) linear 34°

Figure 7.3: Comparisons of tomosynthesis reconstructed using projection images acquired with 11.6° and 34° angular coverage in linear geometry. Both slices clearly show airways and detailed vascular structures inside the phantom. The wider (34°) angular coverage results in better reduction of out-of-plane artifacts of ribs.

The 2D source array imaging geometry shows more symmetric in-plane resolutions and better in-depth resolution compared to the 1D linear source array geometry with similar angular coverage. More geometries will be studied in the future and the optimum imaging geometry for stationary chest tomosynthesis will be determined.

The source array used in this study was not originally designed for medical imaging. Therefore, the asymmetric in-plane resolution (10% of MTFs) of the current system in both 1D linear and 2D imaging geometries was mainly due to the anisotropic focal spot size of the source array. The system in-plane resolution of the s-DCT can be further improved with a tube designed for chest tomosynthesis. The 2D source array imaging geometry has shown better in-depth resolution (FWHM of ASF) when compared to 1D linear array geometry with a similar tube footprint. This study suggests that a 2D source array would be more compact than a 1D linear design and have comparable in-depth resolution.

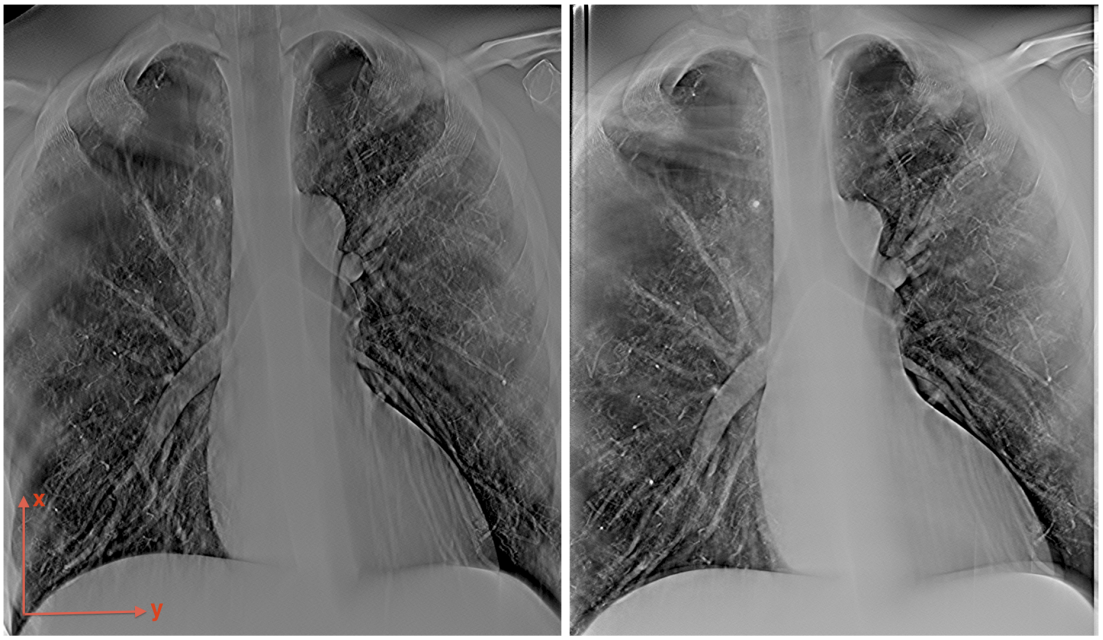

(a) linear 11.6°

(b) square 10°

Figure 7.4: Comparison of tomosynthesis slices of linear imaging geometry and square imaging geometry with comparable angular coverage. The slice of square imaging geometry shows more fine structures along x direction and better reduction of artifacts of ribs from other slices.

CHAPTER 8: Prospectively Gated s-DCT

Section 8.1: Overview

The electronically controlled CNT x-ray source enables physiologically gated imaging, which will minimize image blur due to the patients' respiration motion. In this chapter, we will investigate the feasibility of prospective gated chest tomosynthesis using a prototype s-DCT system with a CNT source array, a high-speed flat panel detector and realistic patient respiratory signals captured using a pressure sensor.

Tomosynthesis images of inflated pig lungs placed inside an anthropomorphic chest phantom were acquired at different respiration rates, with and without gating for image quality comparison. Metal beads of 2 mm diameter were placed on the pig lung for a quantitative measure of image quality. Without gating, the beads blurred to 3.75 mm during a 3 s tomosynthesis acquisition. When gated to the end of the inhalation and exhalation phases the detected bead size reduced to 2.25 mm, much closer to the actual bead size. With gating the observed airway edges were sharper and there were more structural details visible in the lung.

The results demonstrated the feasibility of prospective gating in s-DCT, which substantially reduces image blur associated with lung motion.

Section 8.2: Purpose

Commercial digital chest tomosynthesis (DCT) systems mechanically moves an X-ray source over a large distance to acquire projection images.[1, 3, 13] Typical scans last about 10 s, during which patients are required to hold their breath.[8, 12] Patient motion blur is a main source of image degradation due to long scanning time, even if projection images

are acquired within one breath hold.[33] Respiration motion during the image acquisition may cause severe artifacts.[14] A literature review by AAPM task group showed the motion of nodules due to respiration can be up to 20 mm.[32] The feasibility of stationary chest tomosynthesis system (s-DCT) using a CNT based distributed X-ray source array has been demonstrated.[85, 86, 49] The s-DCT acquires projection images by switching individually controllable CNT x-ray sources without moving the x-ray tube, saving the time to move the source. The fast switching capability of the CNT x-ray source also allows prospectively gated imaging using physiological signals, such as respiration signals.[45, 79]

The purpose of this chapter is to investigate the feasibility of physiologically gated s-DCT, and to study the effect of gating on image quality.

Section 8.3: Methods

8.3.1: System Description

Figure 8.1 shows the prototype s-DCT system with a linearly distributed CNT x-ray source array. The system consists of a CNT linear x-ray source array, a flat panel detector (Varian 3030D, Varian Medical Systems Inc., CA) and an electronic control unit. The detector has an effective imaging area of 30 cm $\times$ 30 cm with 1536 $\times$ 1536 pixels in full resolution. The pixel size is 194 µm $\times$ 194 µm in full resolution mode. The detector can be operated up to 12.5 fps in full resolution mode and 30 fps in 2 $\times$ 2 binning mode. The source to detector distance is 100 cm, and the tomosynthesis angular coverage is 16.9°.

A switching system is used to control individual x-ray sources in the tube. Coupled with a physiological signal sensor, the x-ray beams can be gated to a specific phase of the signal. The timing graph of the gating scheme is shown in Figure 8.2. The detector was operated in continuous mode. The ready to exposure signal was used as a master signal to trigger the x-ray sources. A logical AND operation was applied between the master signal and the physiological signal. A LabVIEW program automated the image acquisition. Tomosynthesis

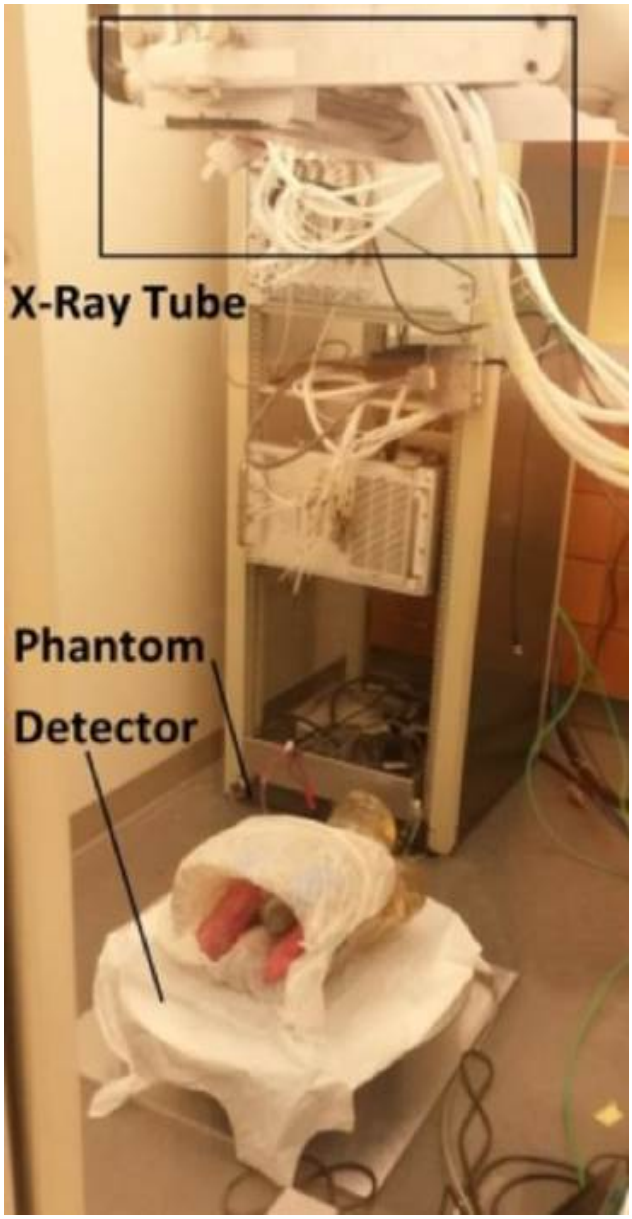

Figure 8.1: Stationary chest tomosynthesis system consisting of a CNT source array, a flat panel detector and an anthropomorphic phantom mounted on the same translation stage. The source array contains 75 focal spots, and has a 298 mm end-to-end length. The detector is 30 cm $\times$ 30 cm, and can acquire images at up to 30 fps in the 2×2 binning mode.

images were reconstructed using an adaptive fan-beam volume reconstruction algorithm, where the 3D cone beam reconstruction was broken down into a series of 2D fan-beams to accelerate the reconstruction.[87]

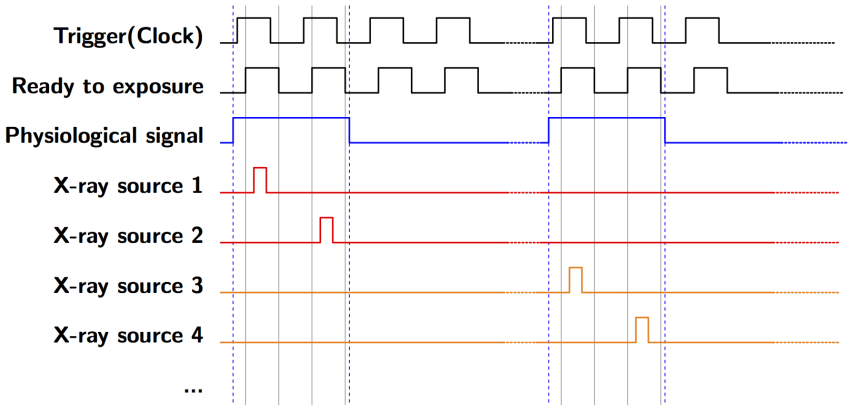

Figure 8.2: Timing graph of physiologically gated s-DCT. In this study, the detector ready to exposure signal is filtered by the physiological signal captured by the Bio Vet sensor. The x-ray source only fires when the lung is in a certain respiration phase.

8.3.2: Dynamic Phantom

A dynamic phantom was constructed using porcine lungs, as shown in Figure 8.3. Pig lungs and heart block was placed inside an anthropomorphic chest phantom (Model RS-320, Radiology Support Devices, Long Beach, CA). The lungs were connected to a ventilator to simulate the respiration motion with respiration cycles and volume comparable to human. The lung motion was monitored using the Bio Vet sensor (m2m Imaging Corp., OH), the sensor measured the maximum pressure when the lung reaches maximum volume (the end of inhalation phase).

8.3.3: Physiologically Gated Tomosynthesis

Trigger signals gated to certain phase of respiration was sent to x-ray source array to activate x-ray exposure, as illustrated in Figure 8.4. Based on the length of gating window, one or more gated images were acquired per respiration cycle. To quantitatively measure the image blur due to the respiration motion, small metal beads of 2 mm in diameter were fixed on the surface of lungs. Anterior-posterior (AP) projection images were acquired at various imaging acquisition speed, breath periods, respiration phases, and with or without

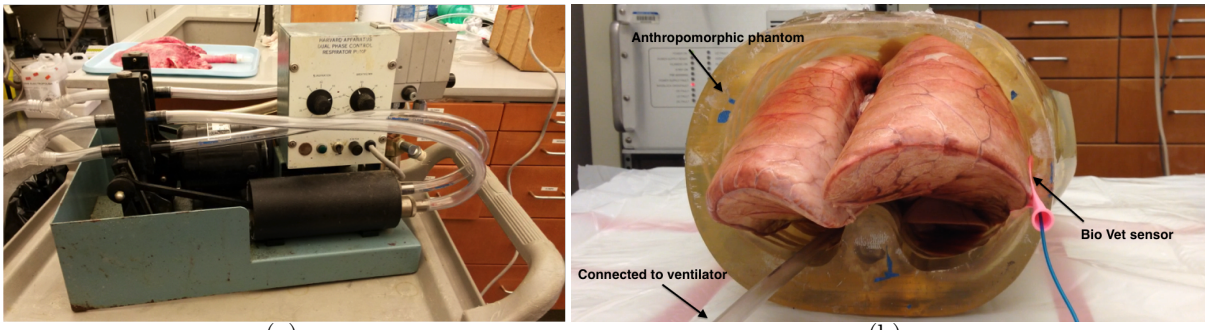

(a) (b)

Figure 8.3: (a) Mechanical ventilator used for the dynamic phantom. The ventilation speed (bpm) and volume per ventilation (percentage of lung volume) can be adjusted to simulate various respiration patterns. (b) The dynamic phantom. Porcine lung and heart block were placed inside the anthropomorphic phantom. Lungs were pumped by the ventilator. The respiration motion was monitored using the pressure based Bio Vet sensor.

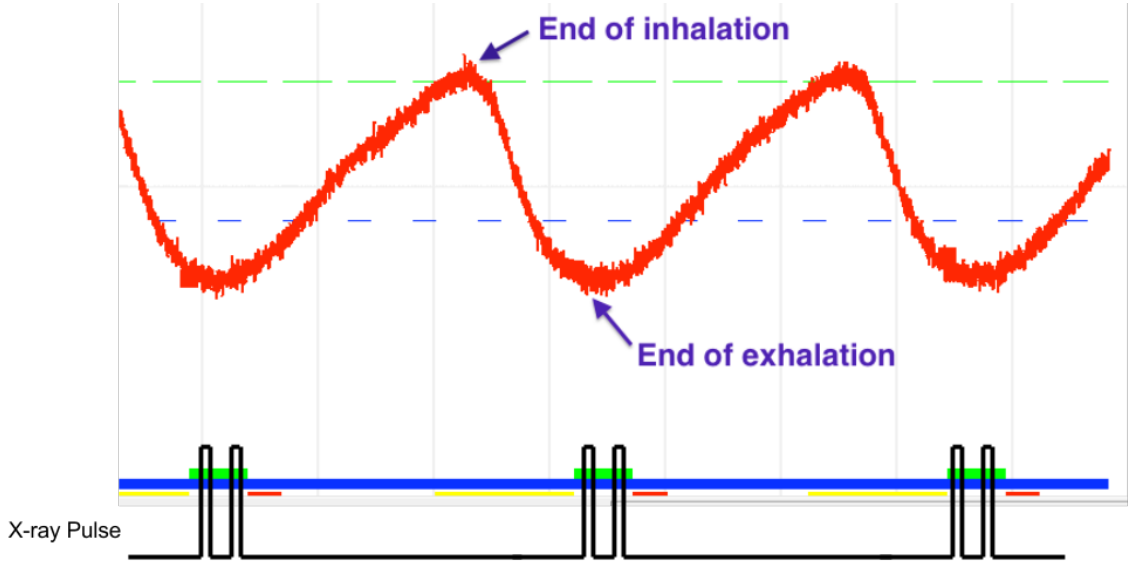

Figure 8.4: Illustration of physiologically gated tomosynthesis. The red curve represents the respiratory motion of the ventilated lungs captured by the Bio Vet sensor. The sensor captures the maximum pressure at the end of inhalation phase. The green bar indicates the gating window. A trigger signal (TTL) is sent to the switching electronics for each gating window.

gating to investigate the effect of gating on image blur reduction.

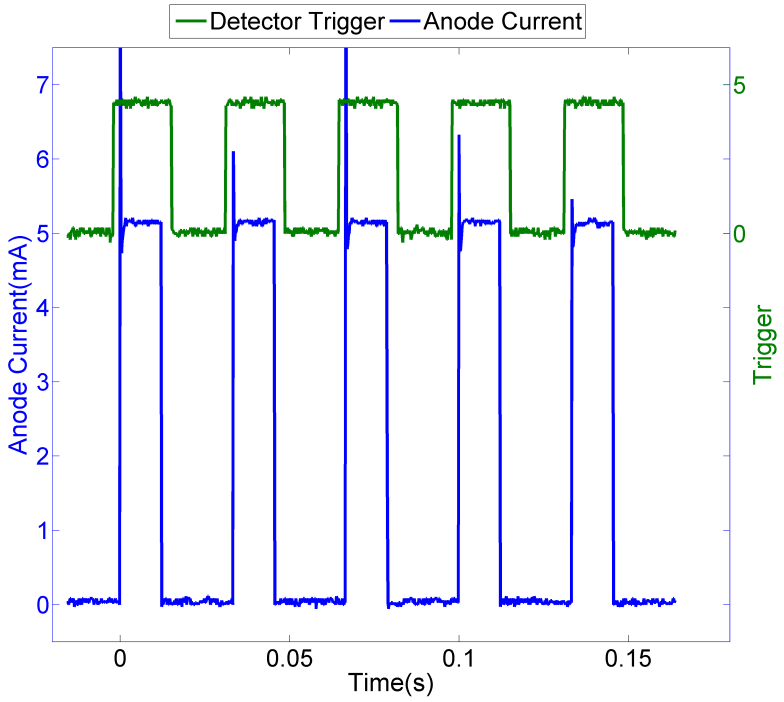

Figure 8.5: The anode current waveforms from 5 different sources during a tomosynthesis scan at 30 fps. The pulse width was 12 ms, within a 16 ms detector integration window. The waveforms show anode current consistency from source to source, and fast switching of individual sources.

Section 8.4: Results

8.4.1: CNT X-ray Source Array

31 sources with a pitch of 8 mm were used for tomosynthesis scans in this study. Figure 8.5 shows the anode current waveform for 5 different sources at 30 fps acquisition speed. All 5 sources consistently output 5 mA anode current with a 12 ms pulse width. The waveform shows the fast switching capability of the CNT x-ray sources and consistent x-ray output from beam to beam.

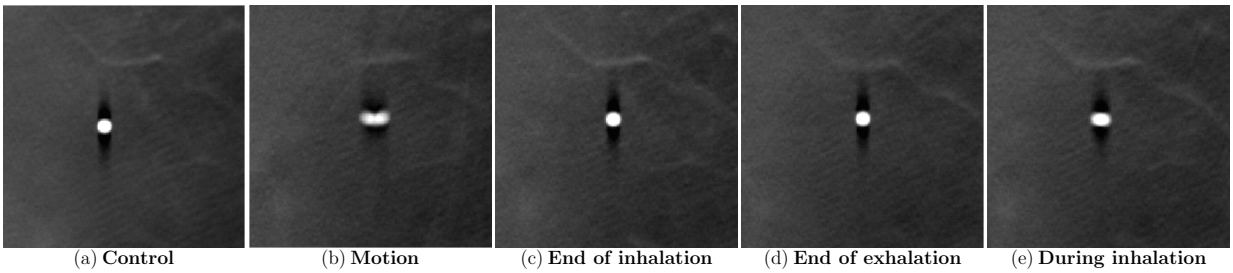

(a) **Control** (b) **Motion** (c) **End of inhalation** (d) **End of exhalation** (e) **During inhalation**

Figure 8.6: (a) Image of the inflated static lung as control. (b) Images of the ventilated lung without gating, the size of the bead was measured to be 3.75 mm. (c) Image acquired gated to the end of inhalation phase. (d) Image acquired at the end of exhalation phase. (e) Image gated to the middle of inhalation. Motion blur was reduced by 85% using physiologically gated tomosynthesis.

8.4.2: Physiologically Gated Tomosynthesis imaging

Images of lungs inside the anthropomorphic phantom were acquired at 80 kVp, 5 mA anode current with 25 ms and 50 ms pulse width per projection. The detector was operated at 10 fps in full resolution mode. The lung was ventilated at a respiration rate of 10 breaths per minute (bpm), comparable to humans.[32] The incident air kerma per projection at the beam entrance plane (25 cm away from detector) was measured to be 16.7 μGy and 33.3 μGy, respectively,[49] which was sufficient compared to average per projection dose of 16.7 μGy used in commercial DCT systems.[3]

Figure 8.6 shows the reconstructed tomosynthesis slices of the beads at different imaging conditions. (a) shows one tomosynthesis slice of one bead with inflated but not ventilated lungs. The motionless datasets shows sharp images of the bead and vascular structures in the background. The diameter of the bead was measured to be 2 mm. (b) shows the slice of the same bead on the ventilated lungs without physiological gating. The whole tomosynthesis sequence was acquired in 3 s, which is less than the whole respiration cycle of 6 s. The image quality was degraded due to respiratory motion of the lung. The metal bead was blurred along the lung motion direction, and the blurred bead was measured as 3.75 mm. (c) and (d) show the same tomosynthesis slices using projection images gated to the end of

inhalation and end of exhalation phase, respectively. The gating window was set as 500 ms, during which 5 projection images were acquired in one respiration cycle. The whole sequence took 36 seconds that span across 6 respiration cycles. The gated image reduced the image blur caused by the respiration motion, as seen by the sharper image of the bead and the boundaries of the airways in the lung compared to non-gated images. The size of the metal beads was measured as 2.25 mm for both cases, an 85.7% reduction in the motion blur. (e) shows the image gated to the middle of the inhalation, where the respiration motion has the largest speed. The gated window was 500 ms, and the whole tomosynthesis sequence took 36 seconds. The image shows blur on the metal bead as the width was measured as 2.75 mm. However, this image blur is smaller than the non-gated image, as the X-ray acquisition window was only 0.5 second compared to 3 seconds of the non-gated dataset, and the images were gated to a portion of the whole respiration motion. The images gated to end of inhalation and end of exhalation phase are sharper due to the slower respiration motion speeds in these two phases.

Figure 8.7 shows selected tomosynthesis images of the same region in the pig lung for image quality comparison. Figure 8.7(a) shows the control image acquired without respiratory motion. The wall of airways and bronchus was clearly visible. Figure 8.7(b) shows the image of the ventilated lung without physiological gating. The respiratory motion degraded the image quality. Figure8.7(c)-(d) show the images gated to end of inhalation phase and end of exhalation phase, respectively. Even though the image acquisition spans through several respiration cycles, the gated images achieved comparable image quality as the control set. The airways and other fine structures are more visible and sharper in the gated images compare to the images acquired without gating.

Section 8.5: Discussion

A physiological gated stationary chest tomosynthesis system was demonstrated using a CNT X-ray source array. Preliminary results have shown the method can greatly reduce

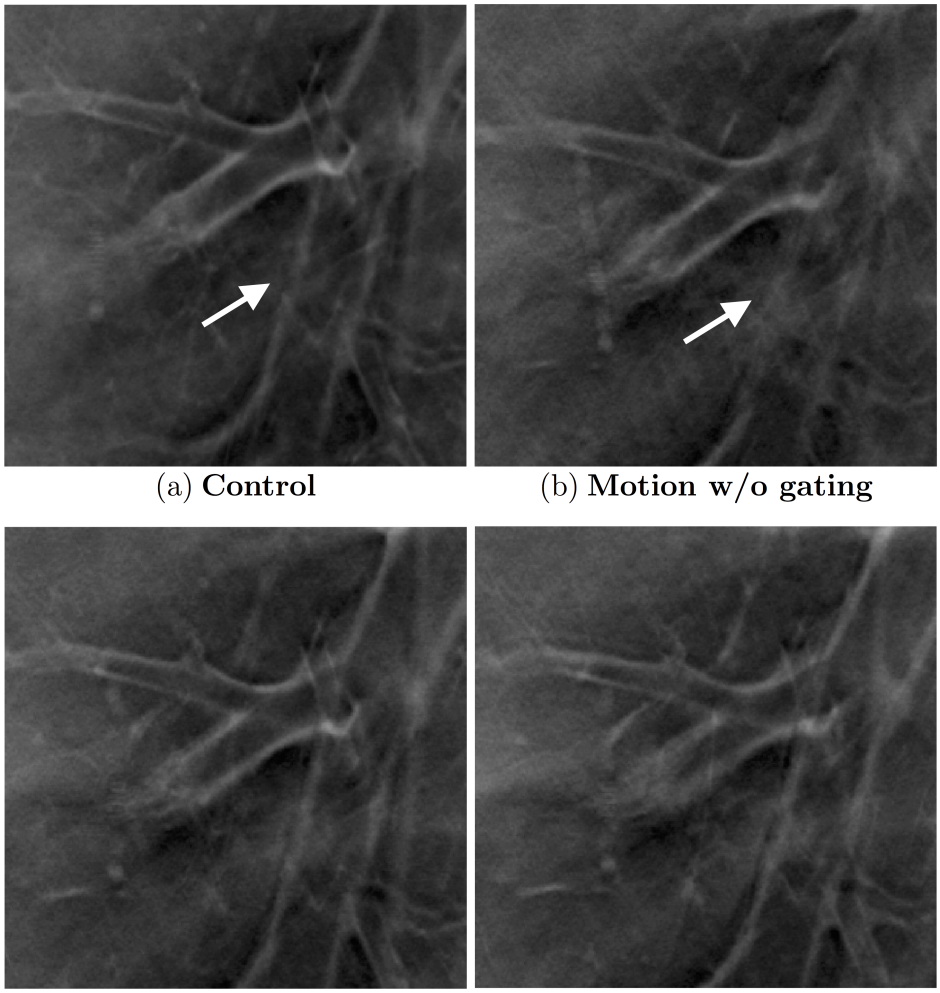

(a) **Control** (b) **Motion w/o gating**

(c) **Gated to end of inhalation** (d) **Gated to end of exhalation**

Figure 8.7: Comparison of the image quality of the lungs on selected tomosynthesis slices acquired under different conditions. (a) shows a bronchus of the inflated but not ventilated pig lung. (b) shows the same region of the ventilated lung without physiological gating. The airways were blurred due to the respiration motion. (c) and (d) show the same region gated to the end of inhalation phase and end of exhalation phase, respectively. The gated images show more fine features and better definition of the airways.

the image blur due to the respiration motion. Motion blur can be reduced up to 85% when images are gated to end of inhalation and end of exhalation phase of respiration cycle, where the motion speed is minimum.

The scanning time, however, was much longer than a conventional tomosynthesis due to the projection images are acquired over several respiration cycles. Other patient motion

during the long scanning time may become the main sources of image degradation. Using longer gating window within each respiration cycle and/or acquiring images at higher speed will reduce the total imaging time. The respiration pattern of a normal human has a short pause ($\sim$ 1 s) after each exhalation. During this pause, the respiration motion has a minimum speed, suggesting a longer gating window would be feasible. Consider a tomosynthesis sequence of 60 projection views with a 30 fps detector, and a gating window of 1 s per respiration cycle. The whole sequence can be acquired in 2 respiration cycles, which would be comparable to the scanning time of current conventional DCT system (10 s).

Section 8.6: Conclusion

The s-DCT system allows prospective gating to any phase of the respiration cycle, substantially reducing blur even with image acquisition over several respiration cycles. This technique can be applied to improve tomosynthesis image quality for patients with trouble holding their breaths.

CHAPTER 9: Applications of s-DCT and Techniques to Improve Image Quality

Section 9.1: Overview

This chapter will briefly discuss the applications of s-DCT and a scatter reduction method to improve the image quality for s-DCT. Section 9.2 will investigate the feasibility of diagnosis and monitoring of cystic fibrosis (CF) in pediatric patients using s-DCT. Section 9.3 will evaluate the effect of scatter reduction using a primary sampling apparatus (PSA) for chest tomosynthesis.

Section 9.2: Using s-DCT as Diagnosis and Monitoring Tools in Pediatric Cystic Fibrosis Patients

9.2.1: Purpose

Cystic fibrosis is a chronic systemic disease that affects approximately 70,000 people worldwide. About 75% of the patients are diagnosed by age of 2.[88, 89] The disease mainly affects the lungs. As the disease progresses, patients suffer inflammation and infections in the lungs. The accumulation of mucus in the lungs and airways also causes difficulties in breathing. Since the disease is a genetic disorder, currently there is no cure. The focus of care for CF patients is diagnosing the disease and any symptoms early, properly monitoring the progress of disease and treating the symptoms as they emerge.

X-ray images allows the monitoring of structural changes inside lungs, such as mucus plugging and airway thickening. Currently, CT is widely used to monitor the progress of the disease.[88–91] The disadvantages of the CT as a monitoring tool are its high examination cost and high dose to patient, especially to children that are more radiosensitive to radiations

than adults. Digital chest tomosynthesis (DCT) is an alternative low dose 3D imaging modality.[1] Multiple low dose x-ray projections are acquired over a limited angle. The reconstructed tomosynthesis slices have high in-plane spatial resolution, which may identify the symptoms better than CT. Vult Von Steyern et. al. have shown that DCT could be useful for monitoring CF.[12, 92, 93] A scoring system using DCT to monitor the progress of CF was developed.[94] Features such as mucus plugging and airway thickening are well defined in DCT slices, while some other symptoms like air trapping cannot be sufficiently viewed.

A conventional DCT scan typically lasts around 10 s as the result of moving single x-ray tube to multiple locations.[1] However, in previous studies, children younger than 8 years old were excluded due to their inability to steadily lay prone and perform a breath-hold up to 10 s.[12] The s-DCT using CNT x-ray source array allows fast scanning when coupled with a fast detector. The capability of performing respiratory gated tomosynthesis eases the requirement for breath holding, which may improve the imaging outcome for patients that are too young to hold their breath.

The purpose of this section is to investigate the feasibility of using s-DCT to identify CF pathologies using an *ex-vivo* CF lung model.

9.2.2: Methods

Ex-vivo CF lung model

Porcine lungs were used to simulate a CF lung model. Lungs were cleaned and any visible cuts on the surface were patched to allow inflation. A 0.5% agarose/water solution was used to simulate the mucus. The solution was first heated to the melting point to allow injection into the lungs. 10 - 15 mL of solution was injected into lungs. Then the lungs were stored in a refrigerator overnight to allow the agarose to gel properly.

System setup and imaging protocols

The processed lungs were placed in an anthropomorphic chest phantom (Model RS-320, Radiology Support Devices, Long Beach, CA). The lungs were inflated with compressed air. The imaging system was setup as Figure 8.1. The SID is set at 100 cm. 31 sources covering 16.9° were used for the tomosynthesis sequence. Images were acquired at 80 kVp with 5 mA tube current.[49] A flat panel detector (Varian 3030D) with 194µm × 194µm pixel size was used. Projection images were reconstructed using a commercial software developed by Real Time Tomography, LLC (Villanova, PA). The images were reconstructed with 3 mm interslice spacing.

9.2.3: Results

Figure 9.1 shows a comparison images of the CF lungs acquired using s-DCT and CT. The simulated mucus solution solidified in both lung lobes, as indicated by the red circles in both images. The tomosynthesis images demonstrated the feasibility of using s-DCT to identify mucus plugging in CF patients.

9.2.4: Discussion and Conclusion

An ex-vivo CF lung model was created to reasonably model some of the characterizations and symptoms of CF. A direct comparison between s-DCT and CT were performed. Tomosynthesis offers comparable image quality in terms of visualizing the build-ups of mucus and detailed airway structures inside lungs, while at a considerably low dose compared to CT. More CF lung models will be developed, and further studies evaluating the efficacy of s-DCT for detecting other CF symptoms will be performed. S-DCTs can also be prospectively gated to certain phase of respiration, allowing images for patients that are too young to hold their breath.[95]

This initial work shows great promises for the further translation of this technology

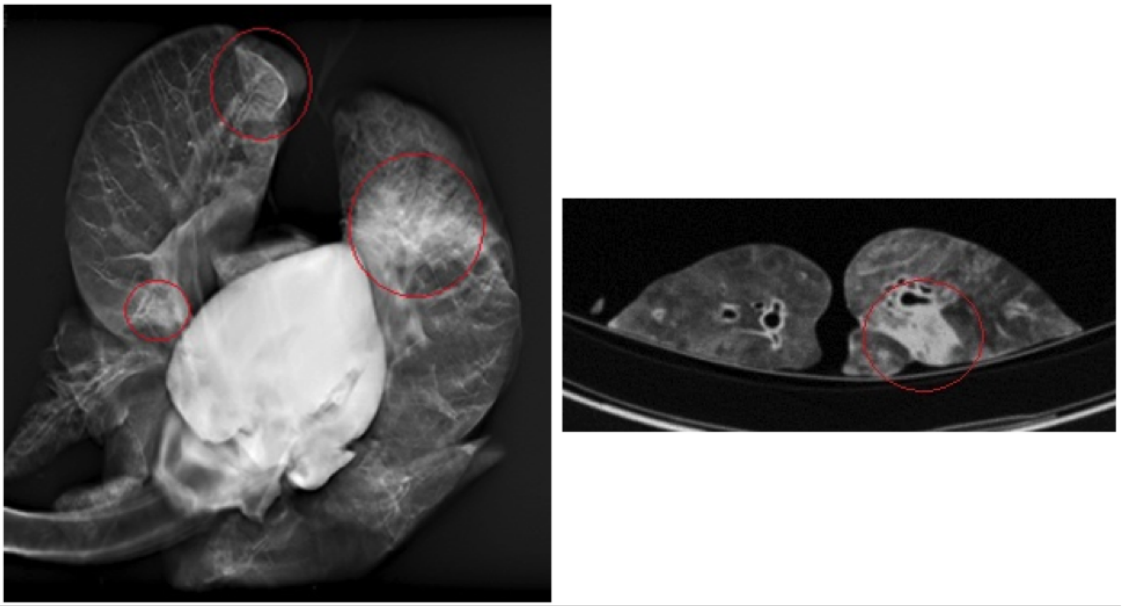

Figure 9.1: Comparison of the images of the CF lung model between s-DCT and CT. The left shows a reconstructed slice of the lung using s-DCT, while the right shows one CT slice of the lung. The red circles indicate the regions where the simulated mucus was injected.

towards CF diagnosis and care.

Section 9.3: A Scatter Reduction Technique for s-DCT

9.3.1: Purpose

Scatter is a well-known problem for many x-ray imaging modalities and applications.[96] The scatter signal from other dense tissues and bones often obscure the details in the soft tissues, especially for thoracic imaging, where the scatter-to-primary ratios can be up to 20.[96, 97] Traditionally, anti-scatter grid have been used in CXR, DTS, and CT for scatter rejections. The anti-scatter grid is placed on the detector, by blocking the scatter signal, the primary x-rays are blocked as well. In order to maintain the signal noise ratio (SNR), additional dose is delivered to patients.

Our lab has proposed a new scatter correction method using a primary beam sampling apparatus(PSA).[73] The methods allows effective scatter reduction with low dose. The

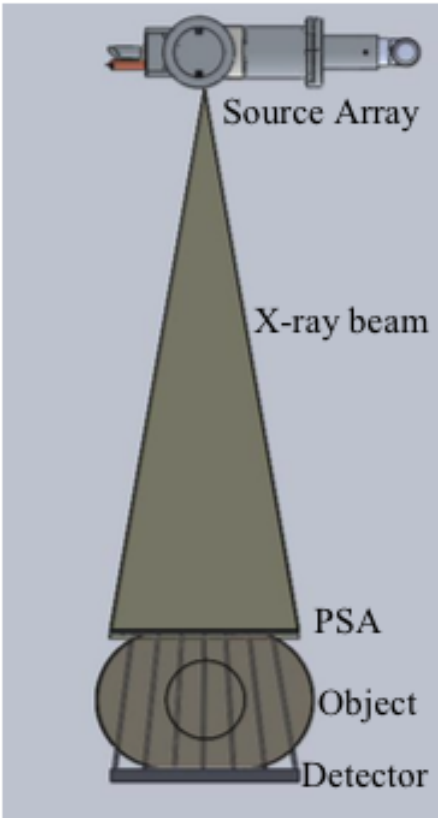

Figure 9.2: Schematic of PSA. PSA only allows passage of a small port of incident x-ray, enabling sampling of the primary beam.

technique has been implemented on the stationary digital breast tomosynthesis system. It is found to be efficient in rejecting the scatter with only 3% dose increase. The purpose of this section is to investigate the feasibility to apply the technology to s-DCT and study the effectiveness of the scatter reduction.

9.3.2: Methods

Primary sampling apparatus

The PSA is a lead collimator that is placed before the imaging object. The plate, which is made of 6 mm lead, contains an array of apertures, which are 6 mm in diameter and separated 31 mm apart. This array of apertures only allows 3% of incident x-ray passing through.

The scatter correction procedure is briefly described as follows. A normal tomosynthesis sequence is acquired without PSA. The value of each pixel in the image contains both the primary signal and the scattering signal from other tissues. Then the PSA is placed on top of the project, a second image is acquired, as shown in Figure 9.2. After the collimation of PSA, pencil beams pass through the object with much less scattering. The primary beam is then sampled from the PSA image. The whole procedure only results in 3% extra dose.

Scatter correction method

In the PSA images,[1] the primary beam is evaluated by sampling the detector pixels associated with the beam passing holes. The scatter signals at these positions are deduced by subtracting the measured primary signal from the normal image.

$$S_s = S_t - S_p \tag{9.1}$$

where the S_s, S_t, and S_p are the mean intensity of the scatter signal, total signal, and primary signal in the sampled regions, respectively. Since most of the scattering signals are low frequencies, the whole scatter map can be interpolated from the sparsely sampled regions using a biharmonic spline interpolation method. Scatter-to-primary ratio (SPR) is calculated for each pixel (x, y) using the interpolated signal and full field image as:

$$SPR(x, y) = \frac{S_s(x, y)}{S_t(x, y) - S_s(x, y)} \tag{9.2}$$

The SPR map is then convoluted with a Gaussian filter to make it smoother and recomputed as:

$$S_{s\_spr} = S_t \cdot \frac{SPR_f}{1 + SPR_f} \tag{9.3}$$

[1]Images acquired with PSA in place.

where the SPR_f is the filtered SPR map, and the S_{s_spr} is the recomputed scatter map. For tomosynthesis scan, the SPR map is dependent on the image angle of each projection. The scatter correct image is then calculated as:

$$S_{p\_cal} = S_t - S_{s\_spr} \tag{9.4}$$

Phantom and cadaver imaging

A physical phantom was constructed to quantitatively evaluate the effectiveness of the PSA. The phantom consists of a water-filled polyethylene container, 12cm × 20cm × 6cm, polyethylene foam, polyethylene spheres, and stainless steel beads, as shown in Figure 9.3(a). The physical phantom was placed inside an anthropomorphic chest phantom (Model RS-320, Radiology Support Devices, Long Beach, CA) to simulate anatomic structures and more scatters.

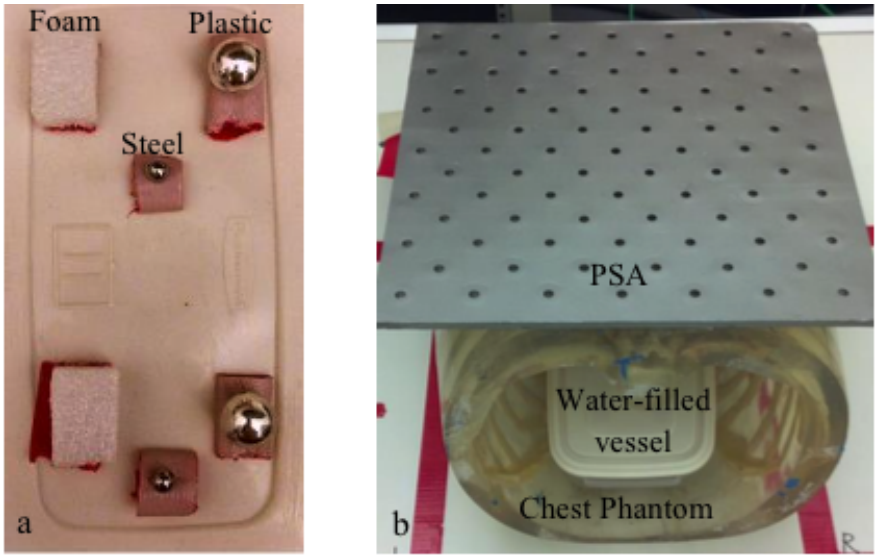

Figure 9.3: (a)Photo of the physical phantom. (b)Phantom setup with the PSA.

Cadaver sample was also imaged using PSA to assess the effectiveness of the technique for human imaging. An adult female thoracic cadaver was obtained through collaboration with colleagues in UNC School of Medicine. The thickness of the sample was 25 cm.

Tomosynthesis images were acquired for both the physical phantom and cadavers with and without PSA using the prototype s-DCT system describe in Chapter 5. Each scan includes 31 projection images. Images were acquired at 80 kVp and 5 mA tube current with various x-ray pulse width. Varian 3030D flat panel detector was used. A commercial anti-scatter grid (Mitaya, Japan) was used for comparison. The grid has a grid ratio of 8:1, 80 lines/cm, 112 cm focal length.

For the physical phantom, the images were acquired with 25 ms and 50 ms pulse width per projection, resulting in 3.86 mAs and 7.75 mAs per full scan, respectively. Scans were performed at 112 cm SID for normal images, PSA images, and images with anti-scatter grid. Cadaver images were acquired at 100 cm and 130 cm SID, with and without PSA. Anti-scatter grid was not applied to cadaver samples.

Tomosynthesis reconstruction

Tomosynthesis images are reconstructed using an adaptive fan-beam volume reconstruction algorithm, where the 3D cone beam reconstruction was broken down to a series of 2D fan-beam to accelerate the reconstruction. The algorithm used Simultaneous Algebraic Reconstruction Technique (SART) with 20 interactions.[87] The slice thickness of the tomosynthesis datasets was 3 mm.

Image analysis

Quantitative evaluation of the scatter reduction was performed for the physical phantom. Signal-difference to noise ratio (SdNR) was used as the metric. The SdNR is defined as:

$$SdNR = \frac{|\mu_{obj} - \mu_{bkg}|}{(\sigma_{obj} + \sigma_{bkg})/2} \tag{9.5}$$

where μ_{obj} and μ_{bkg} are the mean intensities for object and background, respectively. Their standard deviation are measured as σ_{obj} and σ_{bkg}. The analysis was not performed on cadaver

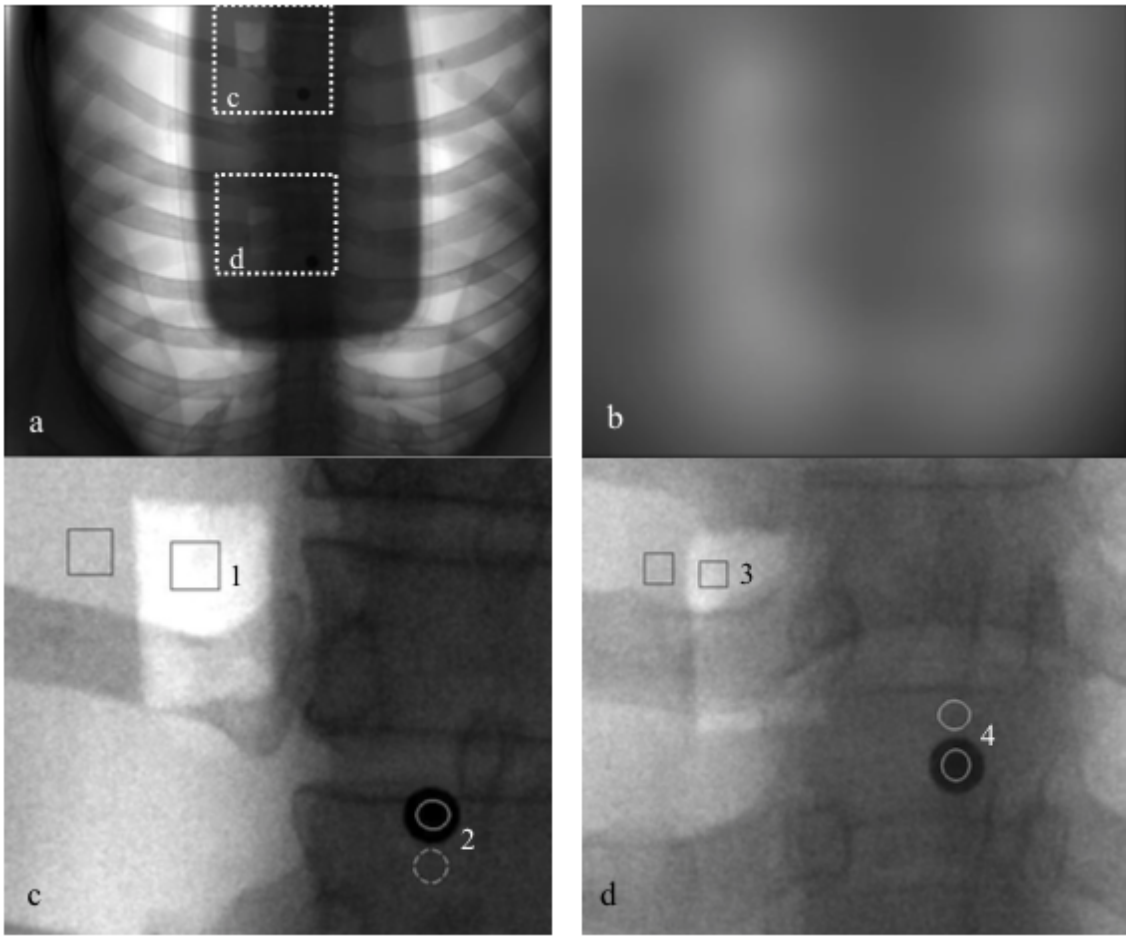

Figure 9.4: (a) Scatter-corrected projection image of the phantom, with ROI depicted. (b) Interpolated scatter map for projection image in (a). (c) Zoomed in image of ROI c. (d) Zoomed in image of the ROI d.

sample due to its lack of the well-define feature.

9.3.3: Results

Physical phantom images

Projection images of the phantom were processed using the scatter reduction method. A representative image is shown in Figure 9.4. The foams and metal beads were visible in all images, while the polyethylene spheres were not due to their similar attenuation coefficient to water. The SdNR for this four objects were analyzed for normal images of 7.75 mAs without

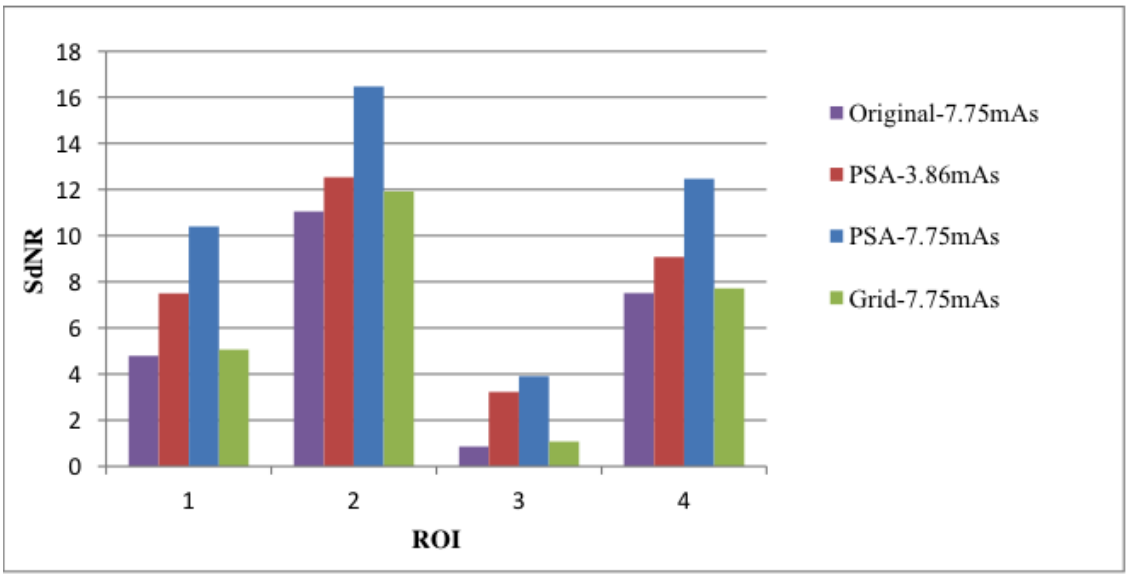

Figure 9.5: SdNR analysis for ROIs in the physical phantom. The SdNR for PSA corrected image increases significantly over that of the uncorrected images. The SdNR for PSA corrected images also outperforms the anti-scatter grid technique.

scatter-correction, PSA corrected images at 3.86 mAs, PSA corrected images at 7.75 mAs, and normal images with anti-scatter grid at 7.75 mAs. Figure 9.5 plots the measured SdNR for all four objects with four imaging parameters. Both PSA corrected images with low and high dose demonstrate improved SdNR over the uncorrected images and images with anti-scatter grid.

Cadaver images

Cadaver images were corrected and reconstructed. The corrected images demonstrates a significant increase in conspicuity of features compared to the uncorrected images. Selected projection images and reconstructed slices are shown in Figure 9.6. The scatter corrected images have improved histogram, which allowing visualization of subtle features.

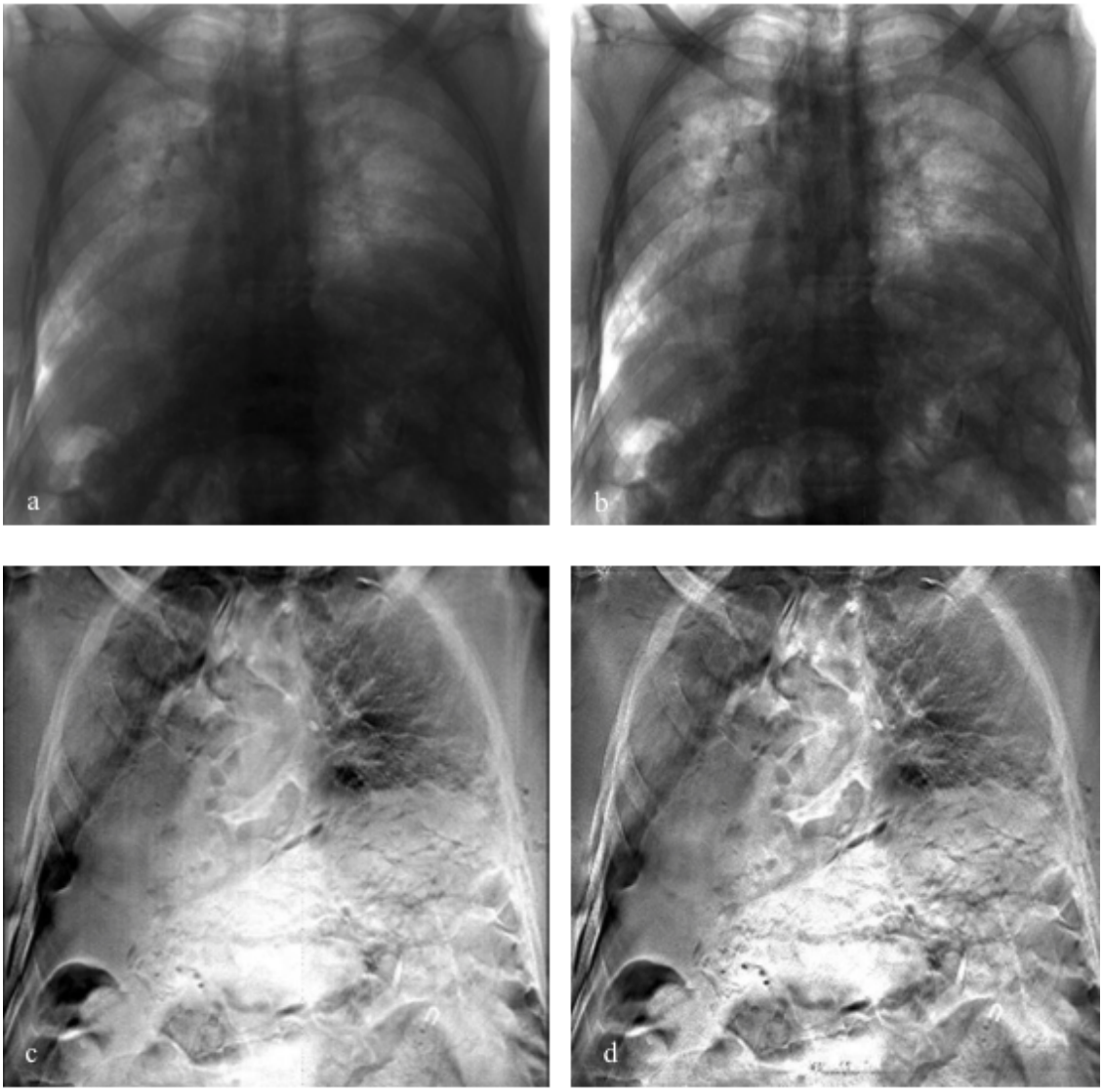

Figure 9.6: Comparison of PSA corrected images and uncorrected image for cadaver sample. (a) Projection image without scatter correction, and (b) with correction. (c) Reconstruction slice without correction, and (d) with correction.

9.3.4: Discussions and Conclusions

This study has successfully demonstrated the feasibility and effectiveness of the proposed scatter reduction method using PSA.

The PSA plate in this study had a sampling geometry with 3% opening area, thus resulting in 3% increase in patient radiation exposure. Effectiveness of this technique has

been evaluated using a physical phantom and cadaver sample. It is found that the PSA technique significantly increases image quality.

However, only one PSA configuration was explored in this study. PSA plate with more and smaller sampling apertures or/and non-uniform sampling pattern may improve the accuracy of the interpolated scatter map. One drawback of the technique is the doubled scanning time due to the second image acquisition with PSA. Longer scanning time may result in patient motion, causing degradation in image quality.

In summary, the scatter reduction method using PSA is effective at reducing scatters and enhancing the visibility of small features. The less dose penalty compared to conventional anti-scatter grid may be practical for clinical implementations.

CHAPTER 10: Clinical Implementation of an s-DCT Prototype

Section 10.1: Overview

The s-DCT prototype was constructed for use in a clinical trial. The bench-top proof-of-concept system was modified and mounted on a DR system. Initial construction was completed in our lab. The system was transferred and installed at Marsico Hall. The system underwent a series of electrical and radiation safety tests before patient trial to ensure the safety of both patient and operator.

This chapter will briefly summarize the clinical implementation of the system.

Section 10.2: Construction of the Prototype s-DCT

An s-DCT prototype was constructed by retrofitting the source array onto an existing DR system at the end of the 2013. The source array was mounted using a custom tube holder, which allows rotation of the source array for various tube positions and orientations.

Besides the mounting structure, and x-ray source, a variety of equipments were needed to for the system to be operational. The required components included an anode power supply, gate power supply, a high voltage multi-beam switching system, a flat panel detector and related electronics. Table 10.1 lists the power producing components and their ratings. All components were installed and secured in an electric rack, with proper connection and grounding for electric safety.[1]

The system was tested before moved to Marsico Hall for clinic evaluation. The system was installed in the clinical trial site and the cart was attached to the floor. Side panels and tube enclosures were made and attached to the system. Figure 10.1 shows the fully

[1]More details of preparing the system for electric safety test refer to Section 10.4.

Table 10.1: List of the power generating components of the system.

Component	Manufacturer	Model	Voltage Rating(kV)	Current Rating(mA)	Power Rating(W)
Anode Power Supply	Spellman	XRV160P1800	160	30	1800
Gate Power Supply	Heinzinger	PNC3000-200ps	3	200	600
Switching System	Xinran Systems	MPE	3	20	60

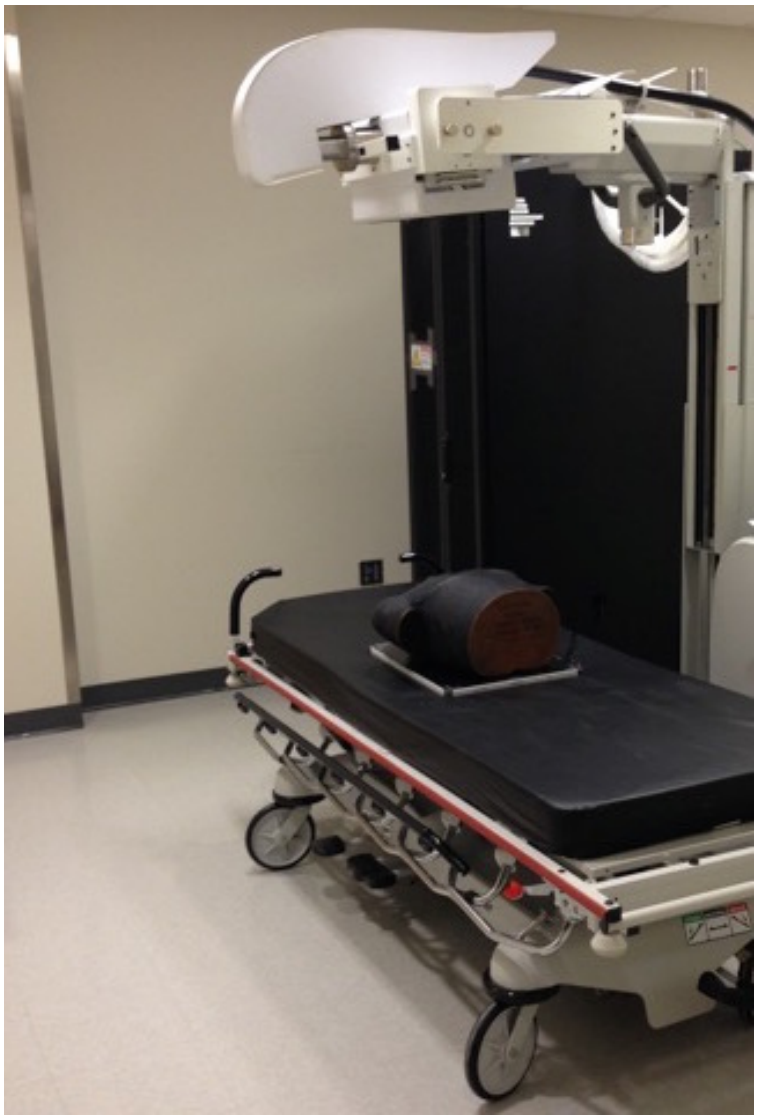

Figure 10.1: Photo of the fully assembled s-DCT system in Marsico Hall.

assembled s-DCT prototype system.

Section 10.3: Software for the s-DCT

A customized LabVIEW program was developed from scratch for the clinical trial, which will be operated by a technician. The flowchart of the program is shown in Figure 10.2. The program consists of two parallel parts, designed in modules. Three modules run parallel to each other, one module controls the anode power supply, one module controls the switching system MPE, and the last module communicates with the detector. Each module registers to event observers at the beginning of the program. The modularized design pattern allows easier maintenance and future expansions. The second thread of the program registers event observers. Once the operator triggers a certain event, certain handlers in the modules are called. The program ends when a full tomosynthesis sequence is acquired, or the operator aborts the sequence due to unexpected situations.

The interface of the program is optimized so minimum operator input is needed. The program also provides a step-by-step guide to the operator. The operator has to finish certain procedures before he/she can navigate through the program, which minimizes operator errors.

Section 10.4: Patient and Operator Safety

The safety of both patient and operator were the highest concern during the system construction. Since the system is an investigational system, it has not been approved or certified by any agency. Therefore, a third party was requested to test the safety of the equipment. MET Lab Inc. (MET southeast, Cary, NC) was employed to test and certificate the electrical safety of the system. The Department of Environment, Health, and Safety (EHS) at UNC tested and certified the radiation safety of the system.

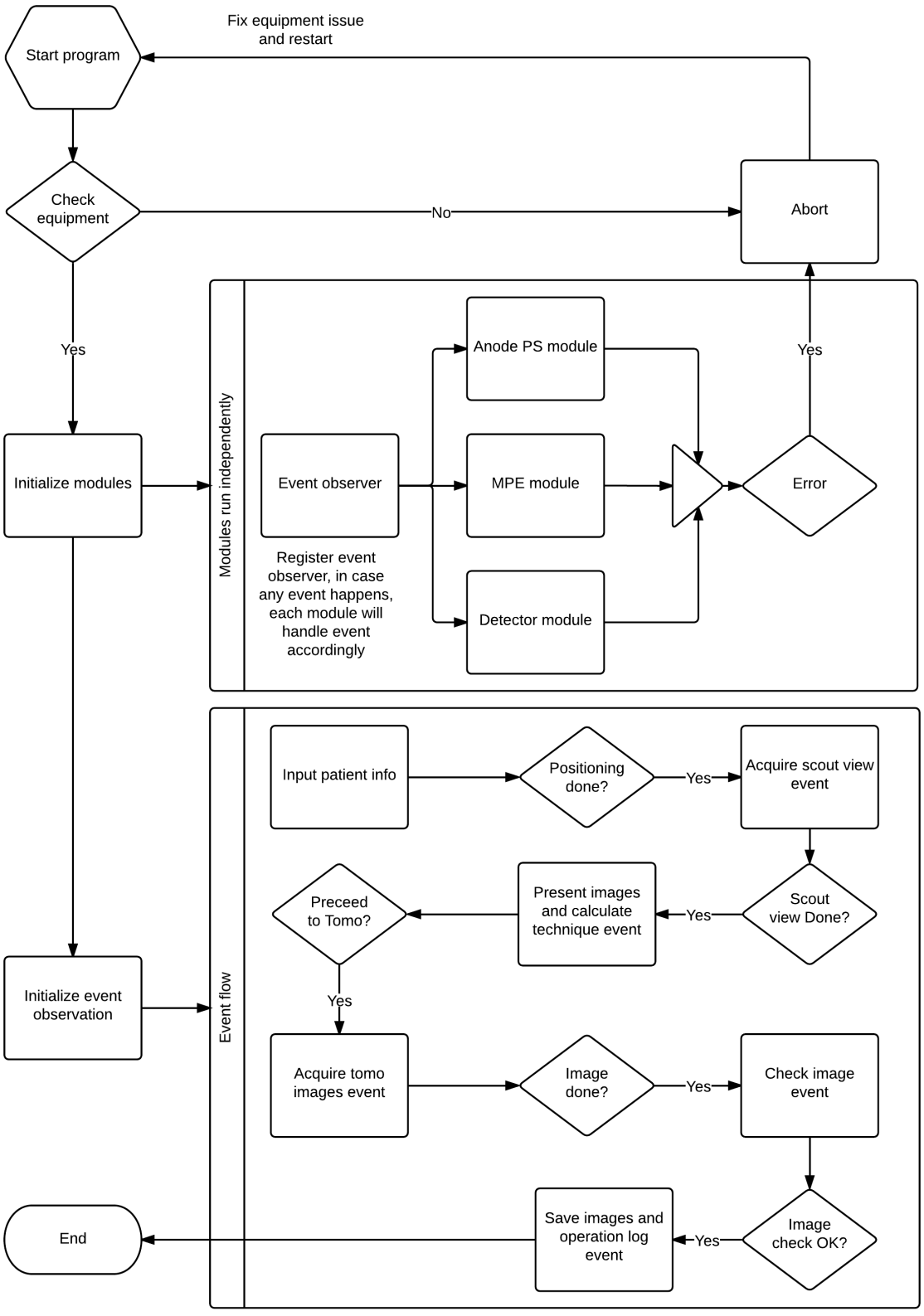

Figure 10.2: Flowchart of the s-DCT system program for clinical trial.

10.4.1: Electrical Safety

In order to use the s-DCT system for clinical trial, the system needed to be electrically safe. The electrical grounding scheme and the isolation of the high voltage generating units were the key issues need to be addressed. The field office of MET Lab Inc in Cary carried out the test and certification. The s-DCT system passed the test on January 22$^{nd.}$, 2015.

Grounding scheme

It is very important to ensure electrical grounding of the whole system be designed that any electrical short (if happens) does not pass through the patient, operator, or the switching electronics. High voltage or current passing through a human can be deadly. Therefore, all electronics were grounded to the grounding bus, and the shortest path was between the anode power supply and earth ground. Large diameter copper wires (gauges 4 and gauges 8) were used to ground the equipment to ensure good conductance to the ground. All grounding cables were coated with green insulator to distinguish them from other cables. Figure 10.3 shows a diagram of the grounding scheme of the system.

Proper isolation of the components

Power generating equipments are required to be certified for use on humans. However, none of the power supplies used in the s-DCT prototype are properly certified. The system can only be certified if these components are properly isolated and in-line ground fault circuit interrupters (GFIC) are used for over current protection. The purpose is to protect the system in fault conditions and prevent hazards from transmitting to the output of the system. Two isolation transformers were placed between the wall power outlet and the input of the power generating components. The transformers are selected based on the apparent power of the equipment connected to them. Peak current draw from equipments were measured when they are working in normal conditions. Table 10.2 list the measured apparent power for all power generating parts in the system. All equipments except the

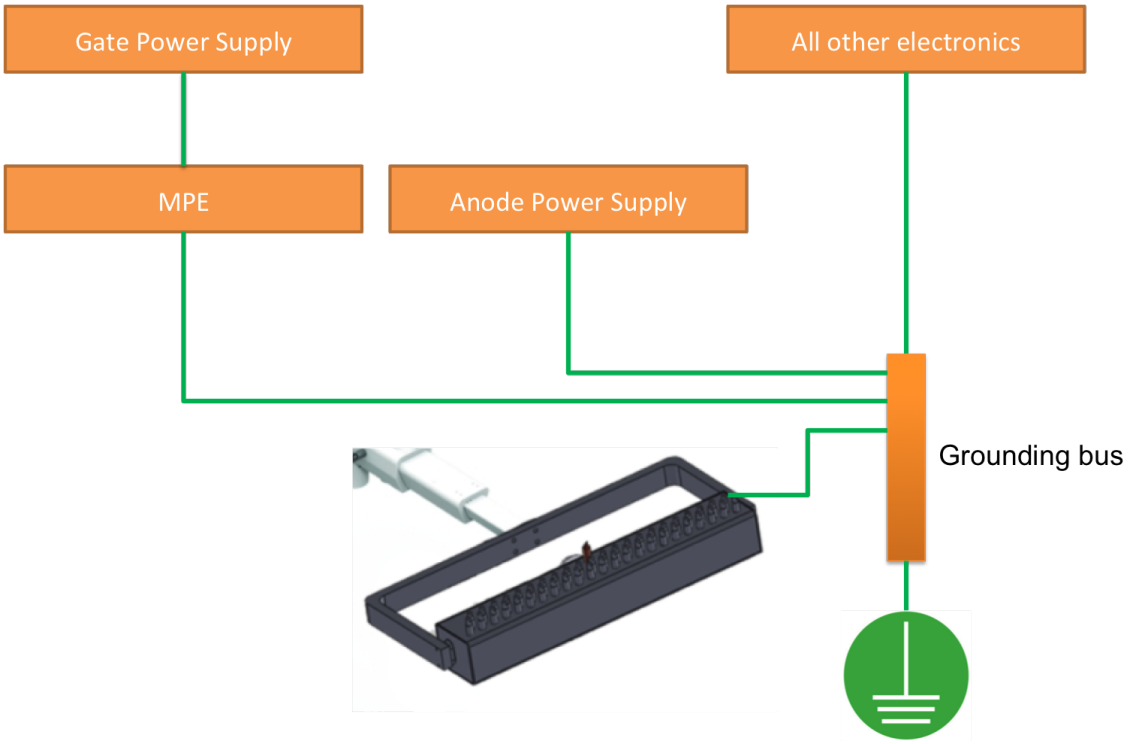

Figure 10.3: The grounding scheme of the s-DCT system. All components are grounded to the grounding bus.

Table 10.2: Measurement of apparent power for power generating equipments.

Equipment	Input Voltage (V)	Peak Current (A)	Peak Apparent Power (Va)
Anode Power Supply	220	10	2200
Gate Power Supply + MPE	120	1.46	175.2
Volteq HY3030D Power Supply	120	0.65	78
Agilent E3612A Power Supply	120	0.4	48
LED Light Field	120	0.1	12

anode power supply are connected to a medical grade isolation transformer (Toroid ISB-100W, input of 120 V) with a maximum power rating of 1000 Va. The total peak apparent power of these components was measured to be 313.2 Va. Another isolation transformer (Sola Hevi-Duty HS14F3BS) is used for the anode power supply. The peak apparent power of the anode power supply was 2.2 kVa, while the isolation transformer was rated to 3 kVa.

10.4.2: Radiation Safety

Radiation safety was evaluated by EHS. There were two main issues needing to be addressed by the radiation safety. The first one was beam collimation and off focal spot radiation. The second was a field survey of the radiation levels. The off focal spot radiation was evaluated and discussed in Chapter 6. This section will cover the collimation and shielding. EHS passed the system for human use on February $13^{\text{th.}}$, 2015.

X-ray collimation

Since the source array used in this s-DCT system was originally designed for other purposes, it is not equipped with a collimator. In order to prevent overdosing to the patient and remove extra scattered x-rays, proper collimation was required. However, because the source pitch in the s-DCT tube was so small (8 mm), designing an external collimator for each focal spot is impractical.

Alternative collimation was constructed, as shown in Figure 10.4. The new collimation consists of two parts. The first part was a tungsten collimator mounted at the source array to provide a beam collimation on the lateral direction. A collimator assembly, including two 1 mm thickness tungsten sheets, was mounted outside the x-ray window. The width between the tungsten blades was calculated based on the width of the detector and targeted SID. This collimator has fixed width since the SID in the clinical trial will be fixed. The black shadows in Figure 10.4 demonstrate the collimated regions in the detector plane by the collimator. The second part included lead aprons, and face shielding for beam "collimation" along the superior-inferior (SI) direction. A photo is shown in Figure 10.5 of the radiation shielding setup.

A light field was designed to facilitate positioning of the patient. The light field utilizes an LED flash light and a mirror to provide a rectangular illuminated area, adjusted to align with the collimated area and matched the size of the detector. The flux of the light was measured, and found to be more than the 100 lumens required by IEC-60601. By positioning

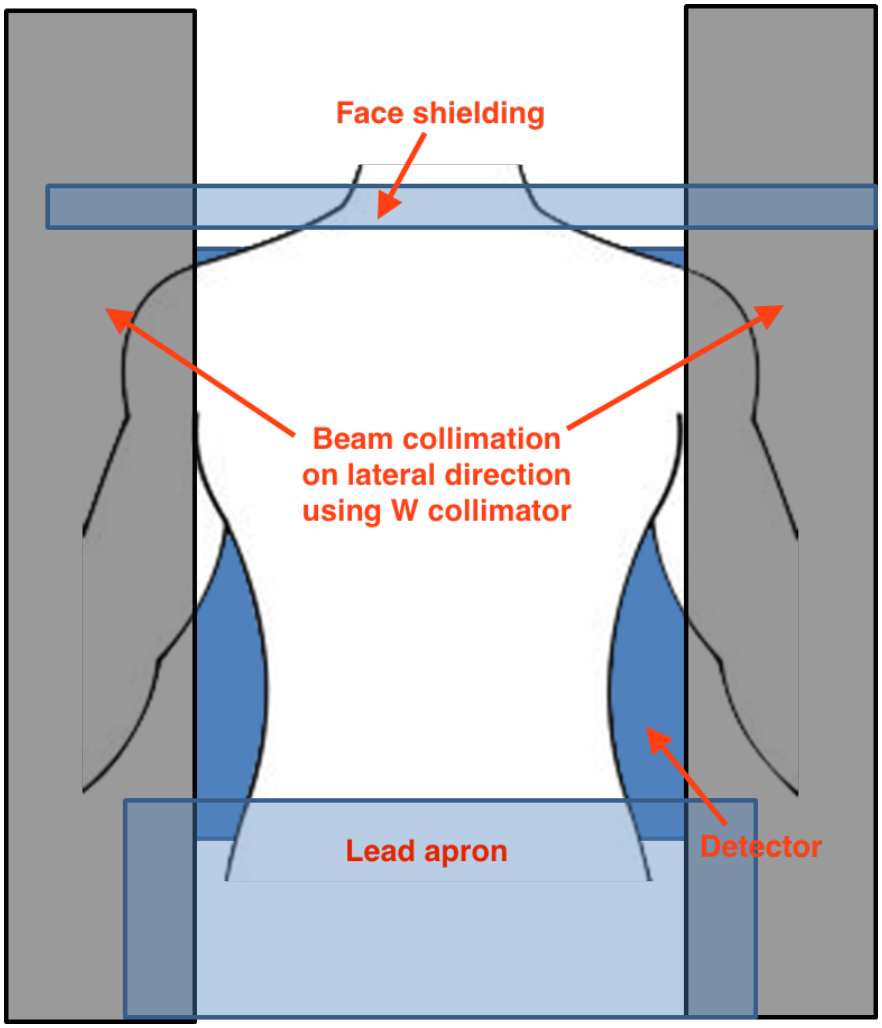

Figure 10.4: Illustration of the beam collimation. The black shadows demonstrate the collimated regions by the tungsten collimator mounted on the tube. The blue shadows show the face shielding and lead apron.

the detector and patient in the illuminated field, the collimated x-ray beam aligns with the detector.

Radiation shielding of the room

A radiation field survey was performed by EHS. The purpose of the survey was to measure the radiation levels to the operator and other people in nearby rooms. The radiation level must be below the regulatory levels. The survey measured the radiation levels at var-

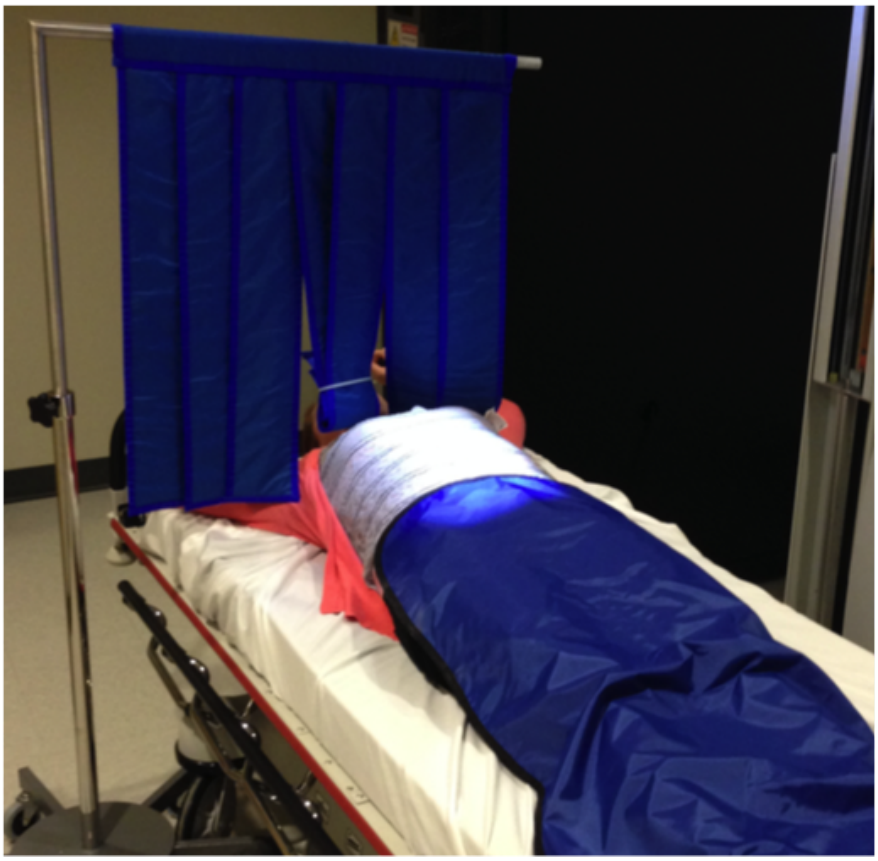

Figure 10.5: A photo demonstrating the radiation shielding on the patient side. The head shielding protects the patient's head from unnecessary x-ray exposure. The lead apron protects the patient's lower body.

ious locations, including the area where the operator works, the corridors, and rooms next to the imaging room, as shown in Figure 10.6. The regions marked by letters indicate where the survey was conducted. Both the s-DCT and the digital radiography system were surveyed. The survey was conducted using an ion chamber dosimeter (Inovision 451B). All measurements were well below the annual limits for radiation exposure.

Section 10.5: Workflow of s-DCT

The s-DCT system will be evaluated and compared to a Carestream digital radiography system. This section will discuss the workflow for the s-DCT image acquisition.

Figure 10.7 shows a diagram of the workflow.

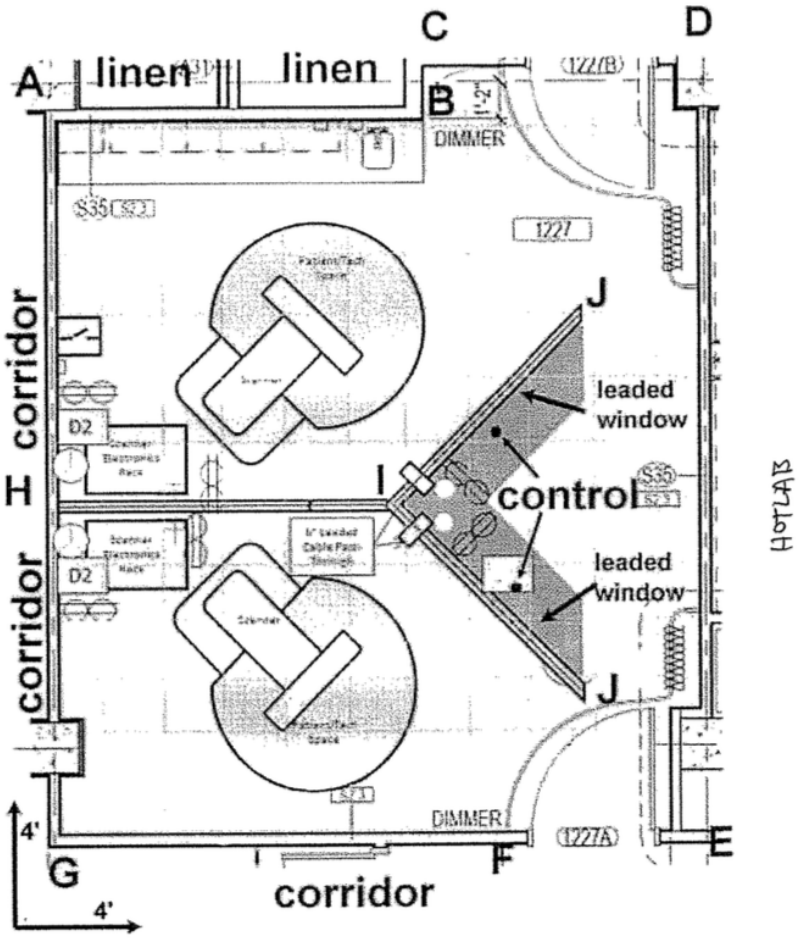

Figure 10.6: Room layout for the s-DCT system and the digital radiography system installed in Marsico. Radiation levels at where operator stands and nearby corridors and rooms are surveyed by EHS.

10.5.1: Patient Check-in

Beginning of each patient image, a system check will be performed to ensure every component in the s-DCT is working properly. If the system fails the check, the study will be postponed and the system will go through a troubleshooting process. If everything works as intended, the technician will assign a unique patient ID to the patient. The patient information will remain confidential throughout the study. Only the patient ID will be used.

The technician checks-in patients using the patient ID. All the images acquired will be saved in a folder associated with the patient ID, and the data will be encrypted.

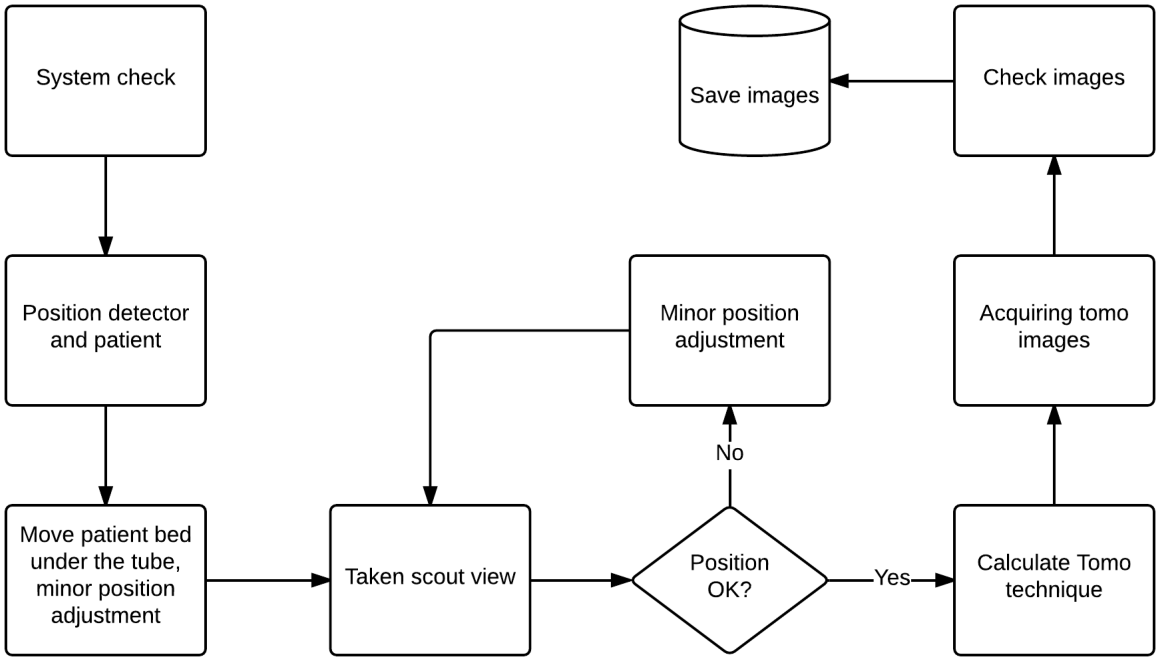

Figure 10.7: The workflow of an s-DCT acquisition.

10.5.2: Patient Positioning

The flat panel detector will be connected and placed on the patient bed. Technician will help the patient lie down on the detector, and adjust the position of detector or patient so that the detector is below the chest.

The light field will be turned on, and the patient bed will be moved below the x-ray tube. The technician needs to move the bed around to make sure the illuminated area is aimed at the patient chest, and roughly aligned with the detector. The face shielding and lead apron will be place on the patient for radiation protection.

During this step, technician needs to briefly go over the instructions for breath holding with the patient. The technician will allow the patient to practice several times, and answer any questions the patient may have. This step is crucial for the success of the imaging.

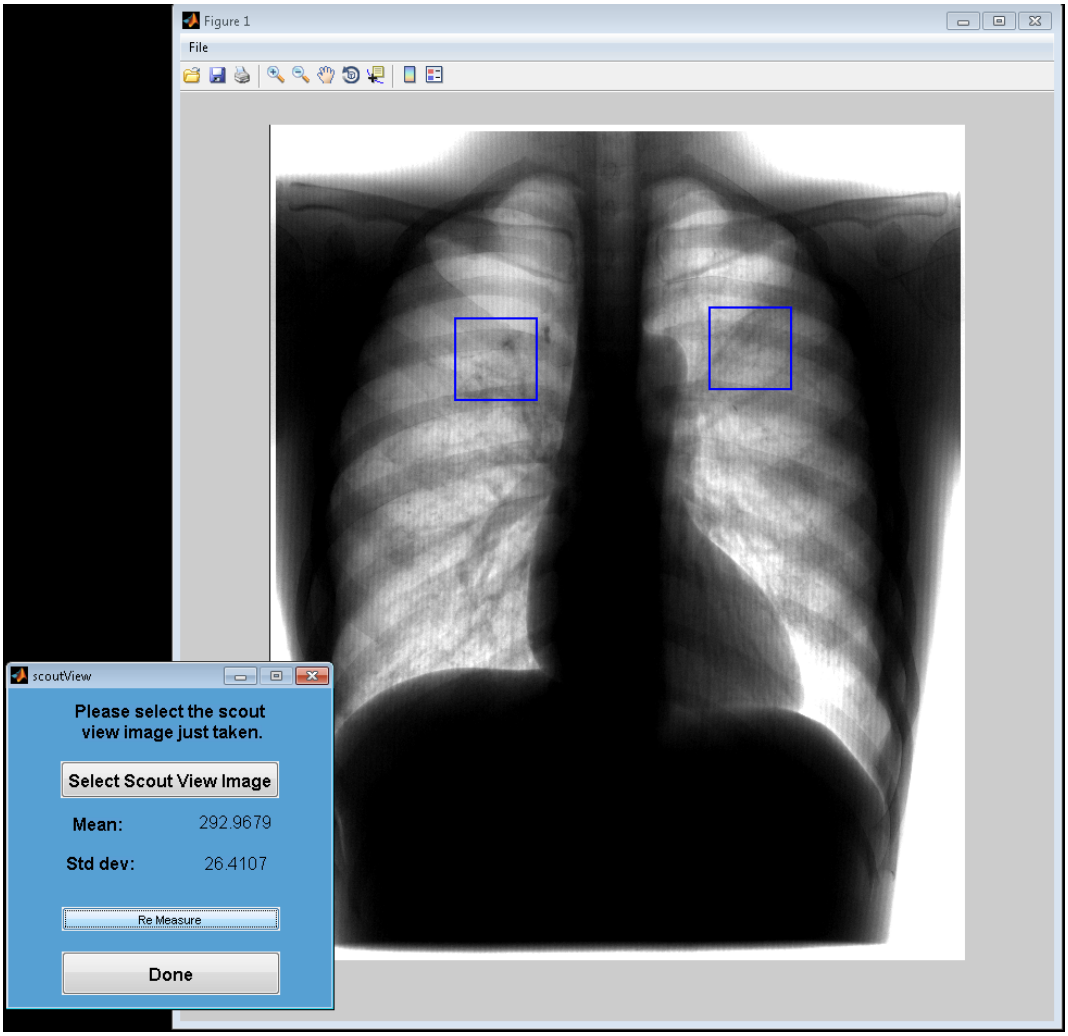

Figure 10.8: Demonstration of technique calculateon using a scout view image of a phantom.

10.5.3: Acquiring the Scout View

A low dose scout view is acquired before acquiring the tomosynthesis sequence. The first purpose of the scout view is to check patient positioning. If the patient is not aligned with the detector, the technician needs to adjust the position of the detector or bed based on the scout image. Another scout view may be acquired to check the positioning.

The second purpose is to calculate the radiation technique for the tomosynthesis. We adopted the technique from conventional DCT systems. Instead of using AEC chambers, two ROIs from the lung region in the scout view image will be selected, the mean pixel

values of these two regions will be calculated. The calculated value will be compared to a reference value. The reference value is calibrated in advance to reflect a detector entrance dose (after passing through patient) of 3.2 μGy. The mAs needed for the reference value will be scaled from the scout view mAs. This mAs is multiplied by 10 and distributed equally over all projection views, determining the mAs per projection. Figure 10.8 demonstrates a calculation of the technique using a scout view image of a phantom. Once the scout view image is loaded, the technique is automatically calculated from two default ROIs. If the ROIs are not satisfactory, the technician can use the mouse cursor to select two new regions for measurement. Once the radiographic technique for tomosynthesis is determined, the technician can proceed to acquire tomosynthesis images.

10.5.4: Acquiring Tomosynthesis Images

A sequence of tomosynthesis images including 31 projections will be acquired in this step. The whole acquisition takes about 10 s. The patient needs to follow the instructions from the technician and hold their breath for 10 s. Failure to do so would void that patient study.

10.5.5: Image Handling and Reconstruction

Images will be saved in the designated folder following a successful image acquisition. Data will be stored on an encrypted hard drive and transported for image reconstruction and analysis.

Section 10.6: Patient Imaging of s-DCT

The s-DCT system successfully imaged the first patient in March of 2015. Figure 10.9 shows the one projection image of the patient. Figure 10.10 shows the one reconstructed slices of the patient.

Figure 10.9: One projection image from the first patient.

Section 10.7: Conclusion

The s-DCT system was constructed and installed in Marsico Hall for clinical evaluation. The system passed both the electrical and radiation safety tests. The system has successfully imaged the first patient. More patient imaging will follow.

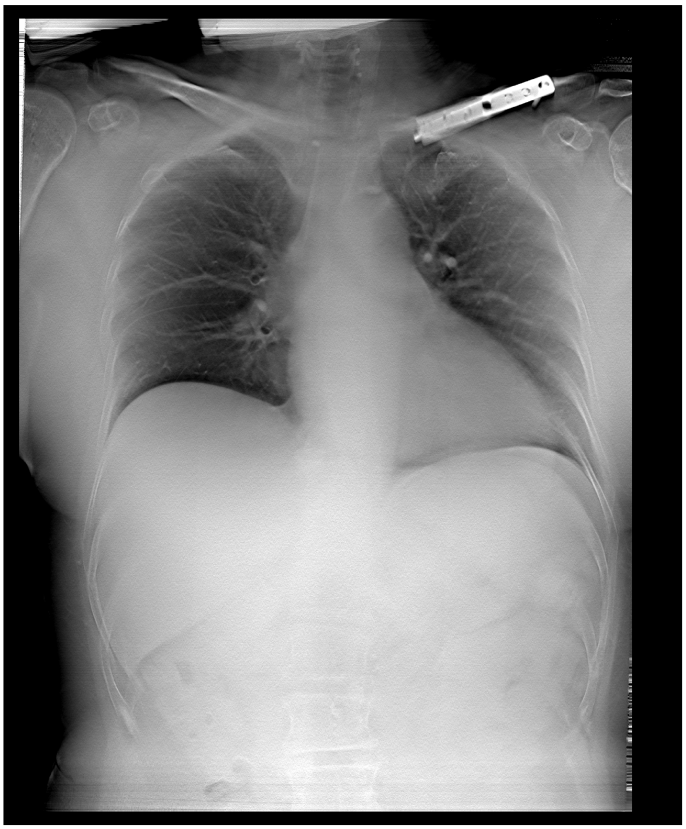

Figure 10.10: A reconstruction slice from the first patient.

CHAPTER 11: Summary and Future Directions

Section 11.1: Summary

A stationary digital chest tomosynthesis system prototype was developed using a CNT x-ray source array. The key components of the system include a distributed x-ray source array, a flat panel detector, and high voltage switching electronics. The source array was retrofitted on a Carestream digital radiography system.

Key questions discussed in this study include the feasibility of s-DCT, imaging configurations, and feasibility of prospective gated s-DCT. It was shown that the CNT source array was capable of delivering sufficient x-ray flux for the purpose of DCT imaging. The source array used in this prototype demonstrated good long term stability of the CNT emitters, suggesting its ability to handle clinical imaging tasks. For the linear source array, it was found that larger angular span is desired due to its improved in-depth resolution in tomosynthesis images. For the conventional DCT systems utilizing a continuously moving x-ray source, larger angular coverage in the DCT acquisition results in longer scanning time. In contrast, the scanning time of s-DCT does not depend on the angular coverage. This advantage allows s-DCT systems to cover a wider angular span for the given number of projections.

Tomosynthesis using other non-conventional shaped source geometry configurations have been studied. It is shown that 2D source geometries such as the square and circle demonstrated better in-depth resolution, and comparable in-plane resolution compared to conventional 1D imaging geometry with a similar tube footprint. The flexibility of the CNT source array and the fast switching capability allows a 2D source array configuration for stationary chest tomosynthesis.

Conventional DCT requires patients to hold their breath for approximately 10 s. While

this might be doable for a normal adult, it could be a hard task for people with lung conditions and pediatric patients too young to hold their breath. The ability to switch individual x-ray sources arbitrarily, allows tomosynthesis projection images to be acquired prospectively to at certain phase of respiratory cycle. Respiration signals can be monitored by sensors and synchronized with s-DCT. We have demonstrated the feasibility of physiologically gated s-DCT. Our preliminary results using a dynamic phantom model show that prospective gated tomosynthesis significantly reduces motion artifacts from respiration motion.

The s-DCT was installed in Marsico Hall for clinical evaluation. The system successfully passed electrical and radiation safety tests. The clinical trial has been approved by the Institutional Review Board (IRB) of UNC. Radiation technologists are being trained on the use of the system. First patient was successfully imaged. More patient trials will start soon.

Section 11.2: Future Directions

This whole study marks the first step toward many applications of CNT based stationary chest tomosynthesis. There still is a great deal of work for the future development and implementation of the technology.

Even though the feasibility of s-DCT and relative applications have been demonstrated,[49, 95, 98, 99] the system is not yet optimized. Future investigations and improvements of the system are needed.

The source array used in this study, is not optimized for the purpose of chest imaging. The source array has a relatively short length and anisotropic focal spots. However, these limitations are solvable. CNT x-ray source arrays with higher kVp, longer length, and isotropic focal spots have been demonstrated. The future s-DCT system will be equipped with an optimized source array.

The imaging time of s-DCT is determined by the dose and detector readout time. Currently, the main limiting factor is the detector acquisition (readout) speed. For the s-DCT being evaluated under clinical trial, the flat panel detector can run up to 3 fps, resulting in

a total 10 s scan time for 30 projection images. Using a faster detector can reduce the total imaging time, resulting in better imaging quality due to less patient motion blur. Flat panel detectors running up to 30 fps are commercially available. Future generations of s-DCT can be implemented with faster detectors to improve the system performance.

Accurately locating the positions of focal spots relative to the detector is crucial for tomosynthesis imaging reconstructions. Current geometry calibration methods utilize high attenuating fiduciary markers. This method can be simple and effective for general purpose in-room s-DCT systems, as the position of the source array and detector are relatively fixed. Other geometry calibration methods without using fiduciary markers need to be investigated in future as well.

The implementation of physiologically gated tomosynthesis also distinguishes s-DCT from conventional x-ray imaging systems. Gated tomosynthesis greatly reduces the motion artifact, and allows tomosynthesis acquisition without breath holding. An s-DCT with this capability would improve the patient care and imaging outcome. For example, for patients with severe lung conditions or traumas who cannot hold their breath easily, a tomosynthesis with gating capability could be a very helpful to doctors.

REFERENCES

[1] Dobbins, James T and McAdams, H Page. "Chest tomosynthesis: technical principles and clinical update." *European journal of radiology*, **72**(2), 244–51 (2009).

[2] Kalender, Willi A. *Computed tomography: fundamentals, system technology, image quality, applications* (John Wiley & Sons) (2011).

[3] Sabol, John M. "A Monte Carlo estimation of effective dose in chest tomosynthesis." *Medical Physics*, **36**(12), 5480–5487 (2009).

[4] Tingberg, Anders. "X-ray tomosynthesis: a review of its use for breast and chest imaging." *Radiation protection dosimetry*, **139**(1-3), 100–7 (2010).

[5] Machida, H, Yuhara, T, and Mori, T. "Optimizing Parameters for Flat-Panel Detector Digital Tomosynthesis." *RadioGraphics*, **30**, 549–562 (2010).

[6] Gomi, Tsutomu and Hirano, Hiroshi. "Clinical potential of digital linear tomosynthesis imaging of total joint arthroplasty." *Journal of digital imaging*, **21**(3), 312–22 (2008).

[7] Mermuys, Koen, De Geeter, Frank, Bacher, Klaus, Van De Moortele, Kris, Coenegrachts, Kenneth, Steyaert, Luc, and Casselman, Jan W. "Digital tomosynthesis in the detection of urolithiasis: Diagnostic performance and dosimetry compared with digital radiography with MDCT as the reference standard." *AJR. American journal of roentgenology*, **195**(1), 161–7 (2010).

[8] Dobbins, James T., McAdams, H. Page, Song, Jae-Woo, Li, Christina M., Godfrey, Devon J., DeLong, David M., Paik, Sang-Hyun, and Martinez-Jimenez, Santiago. "Digital tomosynthesis of the chest for lung nodule detection: Interim sensitivity results from an ongoing NIH-sponsored trial." *Medical Physics*, **35**(6), 2554 (2008).

[9] Bå th, Magnus, Svalkvist, Angelica, von Wrangel, Alexa, Rismyhr-Olsson, Heidi, and Cederblad, Ake. "Effective dose to patients from chest examinations with tomosynthesis." *Radiation protection dosimetry*, **139**(1-3), 153–8 (2010).

[10] Vikgren, Jenny, Zachrisson, Sara, Svalkvist, Angelica, Johnsson, Ase A, Boijsen, Marianne, Flinck, Agneta, Kheddache, Susanne, and Bå th, Magnus. "Comparison of chest tomosynthesis and chest radiography for detection of pulmonary nodules: human observer study of clinical cases." *Radiology*, **249**(3), 1034–1041 (2008).

[11] Yamada, Yoshitake, Jinzaki, Masahiro, Hashimoto, Masahiro, Shiomi, Eisuke, Abe, Takayuki, Kuribayashi, Sachio, and Ogawa, Kenji. "Tomosynthesis for the early detection of pulmonary emphysema: diagnostic performance compared with chest radiography, using multidetector computed tomography as reference." *European radiology* (2013).

[12] Vult von Steyern, Kristina, Björkman-Burtscher, Isabella, and Geijer, Mats. "Tomosynthesis in pulmonary cystic fibrosis with comparison to radiography and computed tomography: a pictorial review." *Insights into imaging*, **3**(1), 81–9 (2012).

[13] Yamada, Yoshitake, Jinzaki, Masahiro, Hasegawa, Ichiro, Shiomi, Eisuke, Sugiura, Hiroaki, Abe, Takayuki, Sato, Yuji, Kuribayashi, Sachio, and Ogawa, Kenji. "Fast Scanning Tomosynthesis for the Detection of Pulmonary Nodules." *Investigative radiology*, **46**(8), 471–477 (2011).

[14] Kim, Sung Mok, Chung, Myung Jin, Lee, Kyung Soo, Kang, Hee, Song, In-Young, Lee, Eun Joo, and Hwang, Hye Sun. "Digital tomosynthesis of the thorax: the influence of respiratory motion artifacts on lung nodule detection." *Acta Radiologica*, **54**(6), 634–639 (2013).

[15] Zhang, J., Yang, G., Cheng, Y., Gao, B., Qiu, Q., Lee, Y. Z., Lu, J. P., and Zhou, O. "Stationary scanning x-ray source based on carbon nanotube field emitters." *Applied Physics Letters*, **86**(18), 184104 (2005).

[16] Kevles, Bettyann. *Naked to the bone: medical imaging in the twentieth century* (Rutgers University Press) (1997).

[17] Seibert, J Anthony and Boone, John M. "X-ray imaging physics for nuclear medicine technologists. Part 2: X-ray interactions and image formation." *Journal of nuclear medicine technology*, **33**, 3–18 (2005).

[18] Shung, K Kirk, Smith, Michael, and Tsui, Benjamin M W. *Principles of medical imaging* (Academic Press) (2012).

[19] Maher, Kieran. *Basic Physics of Digital Radiography* (Wikibooks) (2013).

[20] Bushberg, Jerrold T and Boone, John M. *The essential physics of medical imaging* (Lippincott Williams & Wilkins) (2011).

[21] Kanaya, K and Okayama, S. "Penetration and energy-loss theory of electrons in solid targets." *J. Phys. D: Appl. Phys.*, **5**, 43 (1972).

[22] Food, U S, Administration, Drug, and Others. "Code of federal regulations." (2010).

[23] Compagnone, G, Baleni, M Casadio, Pagan, L, Calzolaio, F L, Barozzi, L, and Bergamini, C. "Comparison of radiation doses to patients undergoing standard radiographic examinations with conventional screen–film radiography, computed radiography and direct digital radiography." *British Journal of Radiology*, **79**, 899–904 (2006).

[24] Grant, D G. "Tomosynthesis: a three-dimensional radiographic imaging technique." *IEEE transactions on bio-medical engineering*, **19**(1), 20–28 (1972).

[25] Levakhina, Yulia. *Three-Dimensional Digital Tomosynthesis: Iterative Reconstruction,*

Artifact Reduction and Alternative Acquisition Geometry (Springer) (2014).

[26] Rivetti, Stefano, Lanconelli, Nico, Bertolini, Marco, and Acchiappati, Domenico. "A new clinical unit for digital radiography based on a thick amorphous Selenium plate: Physical and psychophysical characterization." *Medical Physics*, **38**(8), 4480 (2011).

[27] Terzi, Alberto, Bertolaccini, Luca, and Viti, Andrea. "Lung Cancer Detection with Digital Chest Tomosynthesis: Baseline Results from the Observational Study SOS." *Journal of Thoracic ...*, **8**(6), 685–692 (2013).

[28] Quaia, Emilio, Baratella, Elisa, Cernic, Stefano, Lorusso, Arianna, Casagrande, Federica, Cioffi, Vincenzo, and Cova, Maria Assunta. "Analysis of the impact of digital tomosynthesis on the radiological investigation of patients with suspected pulmonary lesions on chest radiography." *European radiology*, **22**(9), 1912–22 (2012).

[29] Svalkvist, Angelica, Ullman, Gustaf, Hå kansson, Markus, Dance, David R., Sandborg, Michael, Alm Carlsson, Gudrun, and Bå th, Magnus. "Investigation of the effect of varying scatter-to- primary ratios on nodule contrast in chest tomosynthesis." *Proc. SPIE*, **7961**, 79615Y–79615Y–10 (2011).

[30] Flynn, Michael J., McGee, Robert, and Blechinger, Joseph. "Spatial resolution of x-ray tomosynthesis in relation to computed tomography for coronal/sagittal images of the knee." *Proc. SPIE*, **6510**, 65100D–65100D–9 (2007).

[31] Kim, Eun Young, Chung, Myung Jin, Lee, Ho Yun, Koh, Won-Jung, Jung, Hye Na, and Lee, Kyung Soo. "Pulmonary Mycobacterial Disease : Diagnostic Performance of Compared with Chest Radiography." *Radiology*, **257**(1), 269 (2010).

[32] Keall, Paul J, Mageras, Gig S, Balter, James M, Emery, Richard S, Forster, Kenneth M, Jiang, Steve B, Kapatoes, Jeffrey M, Low, Daniel a, Murphy, Martin J, Murray, Brad R, Ramsey, Chester R, Van Herk, Marcel B, Vedam, S Sastry, Wong, John W, and Yorke, Ellen. "The management of respiratory motion in radiation oncology report of AAPM Task Group 76." *Medical physics*, **33**(10), 3874–900 (2006).

[33] Johnsson, Ase Allansdotter, Vikgren, Jenny, and Bath, Magnus. "Chest tomosynthesis: Technical and clinical perspectives." *Seminars in Respiratory and Critical Care Medicine*, **35**, 17–26 (2014).

[34] Iijima, Sumio. "Helical microtubules of graphitic carbon." *Nature*, **354**, 56–58 (1991).

[35] Baxendale, M. "The physics and applications of carbon nanotubes." *JOURNAL OF MATERIALS SCIENCE: MATERIALS IN ELECTRONICS*, **4**, 657–659 (2003).

[36] Awasthi, Kalpana, Srivastava, Anchal, and Srivastava, O N. "Synthesis of carbon nanotubes." *Journal of nanoscience and nanotechnology*, **5**(10), 1616–1636 (2005).

[37] Fowler, R.H. and Nordheim, L. "Electron Emission in Intense Electric Fields." *Pro-*

ceedings of the Royal Society of London A: Mathematical, Physical and Engineering Sciences., **119**, 173–181 (1928).

[38] Gomer, R. *Field emission and field ionization* (Harvard University Press, Cambridge, MA) (1961).

[39] Cheng, Yuan and Zhou, Otto. "Electron field emission from carbon nanotubes." *Comptes Rendus Physique*, **4**, 1021–1033 (2003).

[40] Saito, Yahachi. *Carbon Nanotube and Related Field Emitters: Fundamentals and Applications* (John Wiley & Sons) (2010).

[41] de Heer, Walt A, Châtelain, A, and Ugarte, D. "A Carbon Nanotube Field-Emission Electron Source." *Science*, **270**(5239), 1179–1180 (1995).

[42] Choi, W. B., Chung, D. S., Kang, J. H., Kim, H. Y., Jin, Y. W., Han, I. T., Lee, Y. H., Jung, J. E., Lee, N. S., Park, G. S., and Kim, J. M. "Fully sealed, high-brightness carbon-nanotube field-emission display." *Applied Physics Letters*, **75**(1999), 3129 (1999).

[43] Sugie, H., Tanemura, M., Filip, V., Iwata, K., Takahashi, K., and Okuyama, F. "Carbon nanotubes as electron source in an x-ray tube." *Applied Physics Letters*, **78**(17), 2578 (2001).

[44] Yue, G. Z., Qiu, Q., Gao, Bo, Cheng, Y., Zhang, J., Shimoda, H., Chang, S., Lu, J. P., and Zhou, O. "Generation of continuous and pulsed diagnostic imaging x-ray radiation using a carbon-nanotube-based field-emission cathode." *Applied Physics Letters*, **81**(2002), 355–357 (2002).

[45] Lee, Yueh Z, Burk, Laurel M, Wang, Ko-han, Cao, Guohua, Volmer, Jonathan, Lu, Jianping, and Zhou, Otto. "Prospective respiratory gated carbon nanotube micro computed tomography." *Academic radiology*, **18**(5), 588–93 (2011).

[46] Qian, Xin, Rajaram, Ramya, Calderon-Colon, Xiomara, Yang, Guang, Phan, Tuyen, Lalush, David S., Lu, Jianping, and Zhou, Otto. "Design and characterization of a spatially distributed multibeam field emission x-ray source for stationary digital breast tomosynthesis." *Medical Physics*, **36**(10), 4389 (2009).

[47] Qian, Xin, Tucker, A, Gidcumb, E, Shan, Jing, Yang, Guang, Calderón-Colón, Xiomara, Sultana, Shabana, Lu, Jianping, Zhou, Otto, Spronk, D, Sprenger, F, Zhang, Yiheng, Kennedy, Don, Farbizio, Tom, and Jing, Zhenxue. "High resolution stationary digital breast tomosynthesis using distributed carbon nanotube x-ray source array." *Medical physics*, **39**(April), 2090–2099 (2012).

[48] Hadsell, M., Zhang, J., Laganis, P., Sprenger, F., Shan, J., Zhang, L., Burk, L., Yuan, H., Chang, S., Lu, J., and Zhou, O. "A first generation compact microbeam radiation

therapy system based on carbon nanotube X-ray technology." *Applied Physics Letters*, **103**(2013), 2011–2016 (2013).

[49] Shan, Jing, Tucker, Andrew W, Lee, Yueh Z, Heath, Michael D, Wang, Xiaohui, Foos, David H, Lu, Jianping, and Zhou, Otto. "Stationary chest tomosynthesis using a carbon nanotube x-ray source array: a feasibility study." *Physics in medicine and biology*, **60**(1), 81–100 (2015).

[50] Sultana, Shabana, Calderón-Colón, Xiomara, Cao, Guohua, Zhou, Otto, and Lu, Jianping. "Design and characterization of a carbon-nanotube-based micro-focus x-ray tube for small animal imaging." *Proc. SPIE*, **7622**, 76225G–76225G–9 (2010).

[51] Shan, Jing, Zhou, Otto, and Lu, Jianping. "Anode thermal analysis of high power microfocus CNT x-ray tubes for in vivo small animal imaging." *Proc. SPIE*, **8313**, 83130O–83130O–9 (2012).

[52] Paulus, M J, Gleason, S S, Kennel, S J, Hunsicker, P R, and Johnson, D K. "High resolution X-ray computed tomography: an emerging tool for small animal cancer research." *Neoplasia (New York, N.Y.)*, **2**(1-2), 62–70 (2008).

[53] Ritman, Erik L. "Current Status of Developments and Applications of Micro-CT." *Annual Review of Biomedical Engineering*, **13**(1), 531–552 (2011).

[54] Lee, Yueh Z, Burk, Laurel, Wang, Ko-Han, Cao, Guohua, Lu, Jianping, and Zhou, Otto. "Carbon Nanotube based X-ray Sources: Applications in Pre-Clinical and Medical Imaging." *Nuclear instruments & methods in physics research. Section A, Accelerators, spectrometers, detectors and associated equipment*, **648**, S281–S283 (2011).

[55] Cao, G, Lee, Y Z, Peng, R, Liu, Z, Rajaram, R, Calderon-Colon, X, An, L, Wang, P, Phan, T, Sultana, S, Lalush, D S, Lu, J P, and Zhou, O. "A dynamic micro-CT scanner based on a carbon nanotube field emission x-ray source." *Physics in medicine and biology*, **54**(8), 2323–40 (2009).

[56] Cao, Guohua, Burk, Laurel M., Lee, Yueh Z., Calderon-Colon, Xiomara, Sultana, Shabana, Lu, Jianping, and Zhou, Otto. "Prospective-gated cardiac micro-CT imaging of free-breathing mice using carbon nanotube field emission x-ray." *Medical Physics*, **37**(10), 5306 (2010).

[57] Michell, M. J., Iqbal, A., Wasan, R. K., Evans, D. R., Peacock, C., Lawinski, C. P., Douiri, A., Wilson, R., and Whelehan, P. "A comparison of the accuracy of film-screen mammography, full-field digital mammography, and digital breast tomosynthesis." *Clinical Radiology*, **67**(10), 976–981 (2012).

[58] Hori, K., Fujimoto, T., and Kawanishi, K. "Development of ultra-fast X-ray computed tomography scanner system." *IEEE Transactions on Nuclear Science*, **45**(4), 4–9 (1998).

[59] Gonzales, Brian, Spronk, Derrek, Cheng, Yuan, Zhang, Zheng, Pan, Xiaochuan, Beckmann, Moritz, Zhou, Otto, and Lu, Jianping. "Rectangular computed tomography using a stationary array of CNT emitters: initial experimental results." *Proc. SPIE*, **8668**, 86685K–86685K–8 (2013).

[60] Gonzales, Brian, Spronk, Derrek, Cheng, Yuan, Tucker, Andrew W., Beckmann, Moritz, Zhou, Otto, and Lu, Jianping. "Rectangular fixed-gantry CT prototype: combining CNT x-ray sources and accelerated compressed sensing-based reconstruction." *IEEE Access*, **2**, 971–981 (2014).

[61] Slatkin, D N, Spanne, P, Dilmanian, F a, and Sandborg, M. "Microbeam radiation therapy." *Medical physics*, **19**(1992), 1395–1400 (2012).

[62] Machida, Haruhiko, Yuhara, Toshiyuki, Tamura, Mieko, Numano, Tomokazu, Abe, Shinji, Sabol, John M, Suzuki, Shigeru, and Ueno, Eiko. "Radiation dose of digital tomosynthesis for sinonasal examination: comparison with multi-detector CT." *European journal of radiology*, **81**(6), 1140–5 (2012).

[63] Zhou, Otto and Calderon-colon, Xiomara. "Chapter 9 Carbon nanotube based field emission x-ray technology." In "Carbon Nanotubes," .

[64] Kuo, Johnny, Ringer, Peter a., Fallows, Steven G., Bakic, Predrag R., Maidment, Andrew D. a., and Ng, Susan. "Dynamic Reconstruction and Rendering of 3D Tomosynthesis Images." *Proc. SPIE*, **7961**, 796116–796116–11 (2011).

[65] Fujita, H, Tsai, D Y, Itoh, T, Doi, K, Morishita, J, Ueda, K, and Ohtsuka, A. "A simple method for determining the modulation transfer function in digital radiography." *IEEE transactions on medical imaging*, **11**(1), 34–9 (1992).

[66] Kwan, Alexander L. C., Boone, John M., Yang, Kai, and Huang, Shih-Ying. "Evaluation of the spatial resolution characteristics of a cone-beam breast CT scanner." *Medical Physics*, **34**(1), 275 (2007).

[67] Zhang, Yiheng, Chan, Heang-Ping, Sahiner, Berkman, Wei, Jun, Goodsitt, Mitchell M., Hadjiiski, Lubomir M., Ge, Jun, and Zhou, Chuan. "A comparative study of limited-angle cone-beam reconstruction methods for breast tomosynthesis." *Medical Physics*, **33**(10), 3781 (2006).

[68] Zhao, Bo, Zhou, Jun, Hu, YH, and Mertelmeier, Thomas. "Experimental validation of a three-dimensional linear system model for breast tomosynthesis." *Medical physics*, **36**, 240–251 (2009).

[69] Wu, Tao, Moore, RH, Rafferty, EA, and Kopans, DB. "A comparison of reconstruction algorithms for breast tomosynthesis." *Medical physics*, **31**, 2636–2647 (2004).

[70] Tucker, Andrew W, Lu, Jianping, and Zhou, Otto. "Dependency of image quality on

system configuration parameters in a stationary digital breast tomosynthesis system." *Medical physics*, **40**(3), 031917 (2013).

[71] Deller, Timothy, Jabri, Kadri N., Sabol, John M., Ni, Xianfeng, Avinash, Gopal, Saunders, Rowland, and Uppaluri, Renuka. "Effect of acquisition parameters on image quality in digital tomosynthesis." *Proc. SPIE*, **6510**, 65101L–65101L–11 (2007).

[72] Svalkvist, Angelica, Må nsson, LG, and Bå th, M. "MONTE CARLO SIMULATIONS OF THE DOSIMETRY OF CHEST TOMOSYNTHESIS." *Radiation protection dosimetry*, **139**(1), 144–152 (2010).

[73] Inscoe, Christy R., Tucker, Andrew W., Zhou, Otto Z., and Lu, Jianping. "Demonstration of a scatter correction technique in digital breast tomosynthesis." *Proc. SPIE*, **8668**, 86680H (2013).

[74] Gidcumb, Emily, Gao, Bo, Shan, Jing, Inscoe, Christy, Lu, Jianping, and Zhou, Otto. "Carbon nanotube electron field emitters for x-ray imaging of human breast cancer." *Nanotechnology*, **25**, 245704 (2014).

[75] Grideri, D E, Wright, A, and AusburnS, PK. "Electron beam melting in microfocus x-ray tubes." *Journal of Physics D: Applied Physics*, **19**, 2281 (1986).

[76] Flynn, M J, Hames, S M, Reimann, D A, and Wilderman, S J. "Microfocus X-ray sources for 3D microtomography." *Nuclear Instruments and Methods in Physics Research A*, **353**, 312–315 (1994).

[77] Carslaw, H S and Jaeger, J C. *Conduction of heat in solids*. Oxford science publications (Clarendon Press) (1986).

[78] Lassner, E and Schubert, W. *Tungsten: properties, chemistry, technology of the element, alloys, and chemical compounds* (Springer) (1999).

[79] Cao, Guohua, Burk, Laurel M., Lee, Yueh Z., Calderon-Colon, Xiomara, Sultana, Shabana, Lu, Jianping, and Zhou, Otto. "Prospective-gated cardiac micro-CT imaging of free-breathing mice using carbon nanotube field emission x-ray." *Medical Physics*, **37**(10), 5306 (2010).

[80] Li, Xinhua, Zhang, Da, and Liu, Bob. "A generic geometric calibration method for tomographic imaging systems with flat-panel detectors—A detailed implementation guide." *Medical Physics*, **37**(7), 3844 (2010).

[81] Clackdoyle, R and Mennessier, C. "Centers and centroids of the cone-beam projection of a ball: Supplemental material." *Physics in Medicine and Biology*, **0**(27), 1–9 (2011).

[82] Maltz, Jonathan S, Sprenger, Frank, Fuerst, Jens, Paidi, Ajay, Fadler, Franz, and Bani-Hashemi, Ali R. "Fixed gantry tomosynthesis system for radiation therapy image guidance based on a multiple source x-ray tube with carbon nanotube cathodes." *Medical*

Physics, **36**(5), 1624–1636 (2009).

[83] Stevens, Grant M, Birdwell, Robyn L, Beaulieu, Christopher F, Ikeda, Debra M, and Pelc, Norbert J. "Circular tomosynthesis: potential in imaging of breast and upper cervical spine–preliminary phantom and in vitro study." *Radiology*, **228**(2), 569–75 (2003).

[84] Yavus, M, Edic, PM, Ishaque, AN, and Patch, SK. "METHOD AND APPARATUS FOR RECONSTRUCTING IMAGE DATA ACQUIRED BY A TOMOSYNTHESIS X-RAY IMAGING SYSTEM." *US Patent 6,292,530*, **1**(12) (2001).

[85] Shan, Jing, Chtcheprov, Pavel, Tucker, Andrew W., Lee, Yueh Z., Wang, Xiaohui, Foos, David, Heath, Michael D., Lu, Jianping, and Zhou, Otto. "Stationary chest tomosynthesis using a CNT x-ray source array." *Proc. SPIE*, **8668**, 86680E (2013).

[86] Shan, Jing, Tucker, Andrew W, Lee, Yueh Z, Heath, Michael D, Wang, Xiaohui, Lu, Jianping, Zhou, Otto, and Hill, Chapel. "Evaluation of imaging geometry for stationary chest tomosynthesis." *Proc. SPIE*, **9033**, 903317–1 (2014).

[87] Wu, Gongting, Inscoe, Christina, Calliste, Jabari, Lee, Yueh Z, Zhou, Otto, Lu, Jianping, Carolina, North, and Hill, Chapel. "Adapted fan-beam volume reconstruction for stationary digital breast tomosynthesis." *Proc. SPIE*, **9412**, 1–10 (2015).

[88] de Jong, P a, Lindblad, A, Rubin, L, Hop, W C J, de Jongste, J C, Brink, M, and Tiddens, H a W M. "Progression of lung disease on computed tomography and pulmonary function tests in children and adults with cystic fibrosis." *Thorax*, **61**(April 2004), 80–85 (2006).

[89] Mott, L. S., Park, J., Murray, C. P., Gangell, C. L., de Klerk, N. H., Robinson, P. J., Robertson, C. F., Ranganathan, S. C., Sly, P. D., and Stick, S. M. "Progression of early structural lung disease in young children with cystic fibrosis assessed using CT." *Thorax*, **67**, 509–516 (2012).

[90] O'Connor, Owen J, Vandeleur, Moya, McGarrigle, Anne Marie, Moore, Niamh, McWilliams, Sebastian R, McSweeney, Sean E, O'Neill, Michael, Ni Chroinin, Muireann, and Maher, Michael M. "Development of low-dose protocols for thin-section CT assessment of cystic fibrosis in pediatric patients." *Radiology*, **257**(3), 820–829 (2010).

[91] Miéville, Frédéric a., Berteloot, Laureline, Grandjean, Albane, Ayestaran, Paul, Gudinchet, François, Schmidt, Sabine, Brunelle, Francis, Bochud, François O., and Verdun, Francis R. "Model-based iterative reconstruction in pediatric chest CT: Assessment of image quality in a prospective study of children with cystic fibrosis." *Pediatric Radiology*, **43**, 558–567 (2013).

[92] Vult von Steyern, Kristina, Björkman-Burtscher, Isabella M., and Geijer, Mats. "Radiography, tomosynthesis, CT and MRI in the evaluation of pulmonary cystic fibrosis:

An untangling review of the multitude of scoring systems." *Insights into Imaging*, **4**, 787–798 (2013).

[93] von Steyern, Kristina Vult, Björkman-Burtscher, Isabella M., Weber, Lars, Höglund, Peter, and Geijer, Mats. "Effective dose from chest tomosynthesis in children." *Radiation Protection Dosimetry*, **158**, 290–298 (2014).

[94] Von Steyern, Kristina Vult, Björkman-Burtscher, Isabella M., Höglund, Peter, Bozovic, Gracijela, Wiklund, Marie, and Geijer, Mats. "Description and validation of a scoring system for tomosynthesis in pulmonary cystic fibrosis." *European Radiology*, **22**, 2718–2728 (2012).

[95] Shan, Jing, Burk, Laurel, Wu, Gongting, Lee, Yueh Z., Heath, Michael D., Wang, Xiaohui, Foos, David, Lu, Jianping, and Zhou, Otto. "Prospective gated chest tomosynthesis using CNT X-ray source array." *Proc. SPIE*, **9412**, 941242 (2015).

[96] Barnes, Gary T. "Contrast and Scatter in X-ray Imaging." *RadioGraphics*, **11**, 307–323 (1991).

[97] Samei, Ehsan, Dobbins, James T, Lo, Joseph Y, and Tornai, Martin P. "A framework for optimising the radiographic technique in digital X-ray imaging." *Radiation protection dosimetry*, **114**(1-3), 220–9 (2005).

[98] Potuzko, Marci, Shan, Jing, Pearce, Caleb, Lee, Yueh Z., Lu, Jianping, and Zhou, Otto. "Feasibility study of the diagnosis and monitoring of cystic fibrosis in pediatric patients using stationary digital chest tomosynthesis." *Proc. SPIE*, **9412**, 941226 (2015).

[99] Inscoe, Christina R, Wu, Gongting, Shan, Jing, Lee, Yueh Z, Zhou, Otto, and Lu, Jianping. "Low dose scatter correction for digital chest tomosynthesis." *Proc. SPIE*, **9412**, 1–8 (2015).